

University of Belgrade

Faculty of Physics

Radovan J. Dojčilović

**Fabrication of silver-tryptophan and
graphene oxide fluorescent nanostructures
and investigation of their interaction with
biological systems**

Doctoral Dissertation

Belgrade, 2017.

Univerzitet u Beogradu

Fizički fakultet

Radovan J. Dojčilović

**Fabrikacija srebro-triptofan i grafen oksid
fluorescentnih nanostruktura i ispitivanje
njihove interakcije sa biološkim sistemima**

Doktorska disertacija

Beograd, 2017.

Thesis advisor:

Dr Vladimir Đoković, Principal research fellow
Vinča Institute of Nuclear Sciences

Committee members:

Dr Vladimir Đoković, Principal Research Fellow

Vinča Institute of Nuclear Sciences

Dr Dušan Božanić, Research Associate

Vinča Institute of Nuclear Sciences

Dr Slavica Maletić, Assistant Professor

Faculty of Physics University of Belgrade

Dr Goran Poparić, Associate Professor

Faculty of Physics University of Belgrade

Thesis defense date:

ACKNOWLEDGMENT

I would like to express my special appreciation and thanks to my thesis advisor Dr Vladimir Đoković and thesis co-advisor Dr Dušan Božanić, for the continuous support of my Ph.D. study and related research, for their patience, motivation, friendship and immense knowledge. Thank you for encouraging my research and for allowing me to grow as a research scientist.

Beside my advisors, I would like to thank the rest of my thesis committee: Dr Slavica Maletić and Dr Goran Poparić, for their insightful comments and suggestions. I would like to recognize prof. dr Nataša Nedeljković for enlightening me the first glance of research during my years of study at the Faculty of Physics.

This dissertation could not have been completed without the great support that I received from so many people over the years. I wish to offer my sincere thanks to the following people.

To my colleague Jelena Pajović for being copilot in this journey, thank you and I wish you all the best in the future.

I am very grateful to dr Vladimir and dr Vera Pavlović for engaging me in my first contributed paper, to dr Matthieu Réfrégiers for advice and wisdom during and after beamtime at synchrotron SOLEIL, to dr Slavka Kaščaková for preparing cell cultures and willing to help in every aspect of my research, to dr Suzana Dimitrijević-Branković and Miona Miljković for teaching me everything about experimental biology, and to dr Aleksandar Milosavljević for collaborations and conversations we had.

I am also very grateful to all those at Laboratory for radiation chemistry and physics (Vinča Institute), especially to dr Vesna Vodnik, dr Una Bogdanović, dr Tatjana Savić, dr Marija Radoičić, dr Mila Vranješ, dr Ivana Zeković, dr Lea Lenhardt Acković and others who were always so helpful and provided me with their assistance throughout my dissertation. I acknowledge dr Zoran Šaponjić, dr Jovan Nedeljković, dr Miroslav Dramićanin, dr Nataša Bibić, and dr Nataša Jović for their support at various phases of the research.

A special thanks to my family: my parents Violeta and Jablan, my late grandfather Stojan and to my brother Vladimir, Katarina, Milena and Pavle for supporting me spiritually throughout writing this thesis and my life In general. And finally, thank you Jelena for being there for me and for making it possible to complete what I started.

Radovan Dojčilović

Abstract

Silver-tryptophan and graphene oxide fluorescent nanostructures were fabricated and tested as fluorescent probes for deep UV (DUV) bioimaging. The obtained nanostructures were studied by using morphological, structural and optical methods. The interaction of the nanostructures with microbial cells (*Escherichia coli* and *Candida albicans*) and cancer liver cells (Huh7.5.1 cell line) were investigated by fluorescent microscopy with synchrotron excitation in deep UV part of the EM spectrum. The basic physical properties of materials were modified by functionalization methods. Conjugation of silver nanoparticles with amino acid tryptophan resulted in formation of nanostructures with pronounced fluorescence. Transmission electron microscopy (TEM) images and the analyses of the UV-visible spectroscopy (UV-vis) spectra suggested that the addition of tryptophan led to the formation of hybrid nanostructures with prominent eccentricity and larger sizes with respect to that of the initial silver nanoparticles. Fourier transform infrared (FTIR) and x-ray photoelectron spectroscopy (XPS) were used for studying the interaction of tryptophan with the surface of silver nanoparticles. Photoluminescence spectroscopy (PL) showed that the tryptophan functionalized silver nanoparticles exhibit environmentally sensitive fluorescent properties, which was further confirmed by DUV fluorescence imaging study of microbial cells of *E. coli* and *C. albicans*. The DUV imaging showed that it was possible to distinguish the fluorescent signal pertaining to silver–tryptophan nanostructures localized in different cell compartments. Modified Hummers method was used for the preparation of graphene oxide and the reduction was carefully carried out in the presence of hydrazine hydrate. Three distinct graphene-based nanostructures in form of graphene oxide, partially reduced graphene oxide and reduced graphene oxide were fabricated and studied by scanning electron microscopy (SEM), high-resolution TEM coupled with energy dispersion spectroscopy (EDS) and atomic force microscopy (AFM). Changes in the oxidation level of the nanosheets during the reduction process were monitored by Raman spectroscopy, while the changes in the optical properties were monitored with UV-vis and PL. The highest fluorescence intensity was observed for the partially reduced graphene oxide. The fluorescent graphene based structures were used in bioimaging study of cancer liver cell line Huh7.5.1.

Key words: Silver, tryptophan, graphene oxide, functionalization, reduction, UV bioimaging, fluorescence, bacteria, fungus, cancer liver cells.

Scientific field: Physics

Research area: Condensed matter physics and statistical physics

UDC number: 538.9

Apstrakt

Nanostrukture srebro-triptofan i grafen oksid su pripremljene i testirane kao fluorescentne probe za fluorescentnu mikroskopiju živih ćelija. Fizičke osobine nanostrukture su ispitane korišćenjem morfoloških, strukturnih i optičkih metoda. Nakon toga je ispitivana njihova interakcija sa patogenim ćelijama (*Escherichia coli* i *Candida albicans*) i ćelijama raka jetre (Huh7.5.1 ćelijska linija) metodom fluorescentne mikroskopije sa sinhtronskom pobudom u ultraljubičastom (UV) delu elektromagnetnog spektra. Fizičke osobine polaznih materijala (srebro, grafen oksid) su modifikovane kroz proces funkcionalizacije. Konjugacijom srebrnih nanočestica sa amino kiselinom triptofanom dobijene su stabilne nanostrukture sa izraženom fluorescencijom. Metodama transmisiona elektronske mikroskopije (TEM) i apsorpcione spektroskopije u vidljivom i UV delu spektra (UV-vis) pokazano je da vezivanje triptofana dovodi do formiranja hibridnih nanostrukture izraženog ekscentriciteta i većih dimenzija u odnosu na same srebrne nanočestice. Furijeova transmisiona infracrvena spektroskopija (FTIR) i fotoelektronska spektroskopija X-zracima (XPS) su korišćene za proučavanje interakcije triptofana sa površinom srebrnih nanočestica. Metodom fotoluminiscentne spektroskopije je pokazano da nanočestice srebra funkcionalizovane triptofanom pokazuju emisijske osobine koje zavise od hemijskog okruženja, što je kasnije potvrđeno fluorescentnom mikroskopijom patogenih ćelija *E. coli* i *C. albicans*. Pokazano je da je moguće selektovati fluorescentni signal, koji dolazi od nanostrukture, u zavisnosti od njihovog položaja u ćeliji. Modifikovana Humersova metoda je korišćena za fabrikaciju grafen oksida, a redukcija je izvršena u prisustvu hidrazina. Dobijene su tri različite nanostrukture bazirane na grafenu (grafen oksid, parcijalno redukovani grafen oksid i redukovani grafen oksid) i ispitivane su skenirajućom elektronskom mikroskopijom (SEM), visoko rezolucijom transmisionom elektronskom mikroskopijom (HRTEM) i mikroskopijom atomskih sila (AFM). Promene u stepenu oksidacije nanostrukture koje su indukovane procesom redukcije su praćene uz pomoć Raman spektroskopije, dok su promene u optičkim osobinama praćene UV-vis i fotoluminiscentnom spektroskopijom. Parcijalno redukovani grafen oksid je pokazao najviši intenzitet fluorescentne emisije za pobudu u UV delu spektra. Fluorescentne nanostrukture na bazi grafen oksida su zatim korišćene za fluorescentnu mikroskopiju ćelija raka jetre Huh7.5.1.

Content

I Introduction	1
References.....	3
II Nanostructured materials for bioimaging	4
II.1. Noble metal nanoparticles	6
II.1.1. Structure and optical properties of noble metal nanoparticles	8
II.1.2. Fluorescent nanostructures based on biomolecule functionalization of noble metal nanoparticles.....	19
References.....	22
II.2. Graphene oxide and reduced graphene oxide	24
II.2.1. Structure and optical properties of graphene oxide and reduced graphene oxide.....	28
II.2.2. Partial reduction of graphene oxide.....	38
II.2.3. Fluorescent nanostructures based on graphene oxide and reduced graphene oxide	45
References.....	53
III Experimental techniques and methods	56
III.1. Procedures for the fabrication of fluorescent nanostructures.....	56
III.1.1. Tryptophan functionalized silver nanoparticles.....	56
III.1.2. Graphene oxide and the reduction of graphene oxide	58
III.2, Preparations of biological samples for experiments	59
III.2.1. Cell cultures.....	59
III.2.2. Antimicrobial, adaptation and uptake tests of microbial cells.....	59
III.2.3. Preparation of biological samples for deep UV imaging.....	61
III.3. Methods for structural characterization of fluorescent nanomaterials	62
III.3.1. Raman imaging copupled with atomic force microscope.....	62
III.3.2. Scanning electron microscopy.....	63
III.3.3. Transmission electron microscopy	63
III.4. Spectroscopy techniques for characterization of fluorescent nanomaterials.....	63
III.4.1. Absorption spectroscopy in the visible and UV part of the EM spectrum	63
III.4.2. Emission spectroscopy in the visible and UV part of the EM spectrum.....	64
III.4.3. Fourier transform infrared spectroscopy	64
III.4.4. X-ray photoelectron spectroscopy	64

III.5. Deep-UV fluorescence microscopy	65
III.5.1. Experimental conditions for deep-UV imaging.....	65
III.5.2. Processing of the fluorescence images.....	66
IV Physical properties of fluorescent nanostructures and their interaction with biological systems	68
IV.1. DUV fluorescence imaging of microbial cells incubated with tryptophan functionalized silver nanoparticles	70
IV.1.1. Structure and optical properties of tryptophan functionalized silver nanoparticles	72
IV.1.2. DUV fluorescence imaging of <i>Escherichia coli</i> incubated with tryptophan functionalized silver nanoparticles.....	79
IV.1.3. DUV fluorescence imaging of <i>Candida albicans</i> incubated with tryptophan functionalized silver nanoparticles.....	84
References.....	93
IV.2. DUV fluorescence imaging of cancer liver cells incubated with graphene-based nanostructures	94
IV.2.1. Structure and optical properties of graphene oxide, partially reduced graphene oxide and reduced graphene oxide	96
IV.2.2. DUV fluorescence imaging of Huh7.5.1 cancer liver cells with graphene oxide, partially reduced graphene oxide and reduced graphene oxide.....	102
References.....	109
V Conclusion.....	110
Additional information: List of author's publications	112

I Introduction

Bioimaging is an important field of biotechnology aimed at acquisition, processing, and visualization of structural or functional images of living systems. Bioimaging itself includes various different fields depending on the type of physical processes used for the acquisition of the images. In the fluorescence bioimaging, the images of biological matter are acquired by using fluorescent probes. The observation of molecular and physical events in living cells represents a key approach in understanding cell biology and has profound influence on the progress in biophysical sciences. Since cells are virtually transparent to visible light, direct visualization of their structural compartments is barely possible. For this reason, the fabrication of the effective and stable fluorescent probes that can enable imaging of the cells and tissues became one of the most important tasks [1, 2]. Continuous research efforts are directed towards development of these fluorescent nanomaterials with an aim to improve non-invasive studying of biological processes at the cellular and molecular level [3, 4].

In this dissertation, we investigated two types of fluorescent nanostructures: tryptophan functionalized silver nanoparticles (AgTrp) and graphene-based nanostructures in the form of graphene oxide (GO), partially reduced graphene oxide (prGO) and reduced graphene oxide (rGO). The fabricated fluorescent nanostructures were first characterized in order to determine their physical properties and then used in deep-UV (DUV) fluorescence imaging study of microbial cells (bacteria *Escherichia coli*, fungus *Candida albicans*) and Huh7.5.1 cancer liver cell line.

Silver nanoparticles were prepared by chemical reduction using NaHB_4 and after that functionalized by amino acid tryptophan. The changes in size and morphology of the silver nanoparticles after the functionalization were investigated by transmission electron microscopy (TEM). The conjugation of tryptophan to the surface of silver nanoparticles and the effects at the interfaces were studied by using x-ray photoelectron spectroscopy (XPS). Tryptophan has the ability to absorb and emit electromagnetic radiation in the UV domain [5]. Functionalization of silver nanoparticles with tryptophan leads to the formation of nanostructures that can resonantly absorb light and exhibit pronounced fluorescence properties. The fluorescence of AgTrp nanostructures depended on the polarity of the environment. As will be seen, this property can be used in DUV fluorescence microscopy to

detect the particular sites in *E. coli* and *C. albicans* cells where the accumulation of the particles takes place.

Graphene oxide nanosheets were prepared by modified Hummers method [6]. Graphene-based nanostructures (GO, prGO and rGO) are the second type of fluorescent nanostructures that are presented in this dissertation. We will show preparation procedures for the fabrication of GO that includes modification of the standard Hummers method [6]. In order to prepare prGO and rGO nanostructures, the reduction of GO was performed by using hydrazine as a reducing agent. The investigation of the changes in structural properties of fabricated graphene oxide induced by the reduction process was conducted by using SEM, high-resolution TEM coupled with EDS and AFM/Raman systems. Optical properties of disordered carbon materials like GO, which contain the mixture of sp^2 and sp^3 hybridized carbon atoms, are highly dependent on their ratio. The reduction of GO directly affects the concentration of sp^2 hybridized carbon atoms. Because the bandgap depends on the size, shape and fraction of sp^2 domains, the tunable photoluminescence could be achieved by controlling the reduction process [7]. UV-visible and photoluminescence spectroscopies were employed to study the changes in optical properties during the reduction. By carefully control of the reduction process, a stable structure with pronounced fluorescence intensity was fabricated in the form of partially reduced graphene oxide (prGO) and used for deep UV bioimaging study of cancer liver cells (Huh7.5.1 cell line). For comparison, we also investigated the fluorescence properties of the cancer liver cells prior and after the incubation with GO and rGO.

Doctoral dissertation is organized as follows: in Chapter II are presented structural and optical properties of nanomaterials based on noble metal nanoparticles and graphene with emphasizes on their applications in bioimaging. Chapter III concerns the methods used in fabrication of silver-tryptophan and graphene oxide fluorescent nanostructures and the experimental techniques used for their morphological structural and optical analyses. We also present DUV fluorescence imaging technique employed for probing the interaction between fabricated fluorescent nanostructures and biological systems. The discussions of the obtained results from these investigations are presented in chapter IV, which is divided in sections that are related to the particular types of nanostructures. Concluding remarks are given in chapter V. References are assigned to each chapter, separately.

References

- [1] O. S. Wolfbeis, *Chemical Society Reviews* 44 (2015) 4743.
- [2] C. Cheng, S. Li, A. Thomas, N. A. Kotov and R. Haag, *Chemical Reviews* 117 (2017) 1826.
- [3] S. Park et al., *Nature Reviews Materials* 2 (2017) 17014.
- [4] J. M. Yoo, J. H. Kang and B. H. Hong, *Chemical Society Reviews* 44(14) (2015) 4835.
- [5] J. R. Lakowicz, *Principles of Fluorescence Spectroscopy* (Springer, New York, 2006.).
- [6] W. S. Hummers and R. E. Offeman, *Journal of American Chemical Society* 80 (6) (1958) 1339.
- [7] G. Eda et al., *Advanced Materials* 22 (4) (2010) 505.

II Nanostructured materials for bioimaging

Fluorescent nanostructures are nanometer-sized objects, which exhibit fluorescence when excited with electromagnetic radiation. Fluorescence occurs when the electron from the singlet state of the excited molecular orbital is paired with the electron from the ground state of the opposite spin and returns to the ground state followed by emission of the photon. According to the spin selection rule, the transition from the excited to the ground state is allowed and it occurs very quickly ($\sim 10^{-8}$ s). The fluorescence photons, emitted by the nanostructures, can be detected with fluorescence spectroscopy and microscopy. In the last decades, the development of the methods for the fabrication of the fluorescent nanostructures with specific properties went along with significant improvement of the techniques used for their detection [1, 2]. Measurement techniques based on the fluorescence effect are highly sensitive, selective and non-destructive, therefore suitable for the application in a range of different scientific fields including nanotechnology, nanomedicine and biophysics. On the other hand, the fluorescent nanostructures are widely used as a detection medium in bioimaging, and, as such, intensively studied [2, 3]. They usually exhibit good sensitivity, favorable optical signal transduction and fast system response. Nanomaterials that are often used for fluorescent bioimaging include modified organic silicon nanoparticles, semiconductors organic polymers, quantum dots, carbon-based materials (carbon nanotubes, nanodiamonds, graphene etc.), and functionalized metallic nanoparticles [3, 4].

Noble metal nanoparticles are versatile agents with variety of biomedical applications [5–7]. Gold and silver nanoparticles exhibit unique and tunable optical properties on account of their surface plasmon resonance (SPR), which can be easily tuned to desirable wavelengths according to their shape (spherical and anisotropic), size and composition (core/shell or alloy noble metals), enabling their imaging and photothermal applications [8]. Silver nanoparticles are often used as scaffolds in novel nano-architectures, specifically designed for development of new drugs, biosensors, enhancers of Raman signal and pathogen inhibitors. Therefore, the noble metal nanoparticles are conjugated with various peptides, proteins, ligands and DNA in order to be used as therapeutic materials. As noble metal nanoparticles can be easily surface functionalized with biomolecules for targeting particular cell, they are considered as a potential candidate for drug delivery applications. Many believe that the issues such as multidrug resistance, and drug induced side effects can also be avoided using noble metal nanoparticles as drug carriers [7].

Graphene is a monolayer of sp^2 bonded carbon atoms organized in a honeycomb lattice widely used in fundamental and applied research in solid state physics. Due to unique 2d energy dispersion, graphene shows specific physical properties such as ballistic transport at room temperature, large charge mobility and optical transitions with wide bands. But, graphene is a semiconductor without energy bandgap, which is an obstacle for its successful implementation in convention electronics and the modification of its band structure became an important field of research. There are two methods for the modification of graphene's band structure: i) lowering the size of graphene up to few hundreds of carbon atoms into the form of nanoribbons, nanotubes or carbon quantum dots and ii) by functionalization. One of the products of the functionalization of graphene is graphene oxide. Graphene oxide (GO) is a multilayer (or monolayer) 2d structure of graphene which consists of sp^2 and sp^3 hybridized carbon atoms with oxygen functional groups that are present on the surface [10, 9]. Profound optical absorption and wide photoluminescence emission in visible [11] and infrared [12, 13] spectra makes GO favorable material for optoelectronic applications. Unlike graphene, GO has the finite bandgap [14, 15]. It is also important to emphasize that GO is water soluble which makes easier to study its interaction with biological systems. Graphene and its derivatives proved to be excellent biosensor platforms due to the ability to bind biomolecules while having good biocompatibility and high surface area. Graphene oxide is also suitable for fluorescence imaging due to resistance to photobleaching, tunable emission wavelength, high Raman scattering intensity and large absorption cross section in the NIR region [16].

In the present thesis, we investigated functionalized silver nanoparticles and partially reduced graphene oxide as nanostructured probes for deep UV (DUV) bioimaging. For this reason, we will pay attention to these particular materials. This chapter is organized as follows: Section II.1, concerns the noble metal nanoparticles; optical and structural properties of functionalized noble metal nanoparticles, and their applications in bioimaging. In the section II.2, we will present structural properties of graphene oxide and reveal the influence of the reduction process on its optical properties. The last section is dedicated to graphene-based materials as platforms for bioimaging.

II.1. Noble metal nanoparticles

Nanoparticles are solid state objects with characteristic dimensions in the range from 1 nm and 100 nm [17]. In the scientific literature, the term nanoparticles is sometimes related to the particles of larger dimensions, or solely used to describe spherical particles. The nanostructured objects called nanoparticles are rather those structures for which chemical and physical properties differ from that of isolated atoms or molecules of macroscopic crystals of the same substance. Therefore, for the particles with dimensions larger than 100 nm, substance's assets will be similar as for the macroscopic crystals. The properties of structures smaller than 1 nm are more similar to those of atoms or molecules because of the pronounced quantum effects. With the change of the characteristic dimensions of nanoparticles, they experience the change in physical properties. For the given physical quantity there is an interval of dimensions in which it changes continually. Besides on dimensions, the properties of the nanoparticles may depend on their shape and surrounding environments.

By the chemical definition, the noble metals are chemical elements that have pronounced resistance to oxidation, even at high temperatures [18]. This group of elements is not strictly defined, but the elements that are usually included in that group are ruthenium (^{44}Ru), rhodium (^{45}Rh), palladium (^{46}Pd), silver (^{47}Ag), osmium (^{76}Os), iridium (^{77}Ir), platinum (^{78}Pt) and gold (^{79}Au). These are the metals from VIIIb, VIII and Ib groups of second and third period of periodical system of elements. In physics, the definition of noble metals is more profound and it applies to the elements in which the *d*-orbitals are populated and the electronic energy levels are not cross matching with Fermi levels of that element [19]. According to this definition, only copper (^{29}Cu), silver and gold are the noble metals. Because of its chemical stability, noble metals are the most commonly used elements for the fabrication of nanostructures. Silver and gold nanoparticles are the optimal choice for the model systems, because besides their inert nature towards oxidation, they exhibit the surface plasmon resonance in the visible part of the electromagnetic spectrum.

Silver nanoparticles are representing the ideal modeling systems for investigation of physical properties of noble metal nanoparticles. For this reason, they are the most studied nanostructured materials. The reason for a wide application of this material lies also in the large number of procedures for the fabrication of the nanoparticles of different sizes and shapes. The key characteristic of silver nanoparticles is the absorption of light through surface plasmon resonance with the resonant value around 3.6 eV (in vacuum). The position of the

resonance peak may depend on the size and shape of the nanoparticles as well as the environments they are embedded in [20]. Silver nanoparticles exhibit nonlinear optical properties [21], ability to enhance Raman signals [22] and profound catalytic characteristics [23]. One of the most important properties of silver nanoparticles is the ability to inhibit the growth of pathogen microbial systems [24]. Silver nanoparticles can be used as antimicrobial agents against Gram-positive and Gram-negative bacteria, fungus or viruses for which they are showing microbiostatic and microbicidal effects. Antimicrobial activity of the silver nanoparticles takes place mostly through disruption of the cell walls of the pathogens. On the other hand, if used in larger concentrations, silver nanoparticles can have toxic effect on human cells [25].

Of all the noble metals, gold has the highest electrode potential of approximately 1.5 eV and for that reason the gold nanoparticles are chemically very stable. The fabrication of gold nanoparticles is relatively easy due to the resistivity to the oxidation and high melting temperature. Also, there is variety of preparation procedures available for modification of the surface. Chemical inertia of gold nanoparticles is useful for its integration in biological systems. Gold nanoparticles are the most commonly used as contrast biomarkers in living organisms [26], nanovectors for the drug delivery [27, 28] and as photosensitizers in photothermal therapies [29].

II.1.1. Structural and optical properties of functionalized noble metal nanoparticles

Metal nanoparticles have been widely investigated for the delivery of drugs [7, 26, 27]. Therefore the information such as molecular identity, structure, orientation, and nature of bonding of the surface-adsorbed species may provide essential clues on the efficiency of these processes. Also, the interaction between biomolecules and metal surfaces has recently given rise to a large number of investigations due to challenging technological applications in the field of biomaterials, biosensors, and biocatalysis. The large number of procedures employed for the functionalization of nanoparticles that include (bio)polymers, ligands, proteins, enzymes, amino acids, peptides, etc. In this study, tryptophan was used for the functionalization of silver nanoparticles. In that sense, the focus of this chapter will be on structural and optical properties of noble metal nanoparticles that are functionalized with essential amino acids. In chapter II.1.2, we will present the fluorescent nanostructures that are based on noble metal nanoparticles functionalized with biomolecules, with emphasis on their applications in bioimaging.

Because the nanoparticles are small, most of the atoms are situated on the surface. Surface atoms differ in physical properties when compared to the inner atoms of the nanoparticle. Specific characteristics of the surface atoms are a consequence of their coordination with lower number of neighboring atoms than it is the case for crystal lattice of that substance. The decrease in the sizes of nanoparticles results in an increase in the ratio between the number of atoms at the surface and atoms inside the particle, so the influence of the surface atoms on the properties of the nanostructures becomes more profound. The size of the nanoparticles in a particular direction could be smaller than De Broglie wavelength of the charge carriers (typical wavelength of electrons is around 10 nm) [30]. Since the charge mobility is restricted by the dimensions of the nanoparticles, the quantum size effects become important and they can consequently affect optical, electrical and magnetic properties. In the case of metal nanoparticles, quantum size effect is practically annulled due to thermal electron movement, except for very small nanoparticles (< 2 nm) and at very low temperatures [31]. On the other hand, the presence of such large number of free electrons in metals, allows their surface collective oscillations when they are excited with electromagnetic radiation. As a consequence, the absorption spectra of metal nanoparticles exhibit characteristic absorption bands e.g. surface plasmon resonance peaks. The number, positions and widths of these bands depend on their geometry and the chemistry of the environment. This is especially important

for the process of functionalization, since the change in optical properties is a good measure on the degree of conjugation.

Conventional methods for the fabrication of noble metal nanoparticles (NMNP) usually start from the aqueous solutions of metal salts in which reduction agent is added. The size of the formed nanoparticles depends mostly on the type of the reducing agent, but also on the concentration of metal ions, pH values, temperature and other conditions. Silver nanoparticles (AgNP) are most commonly synthesized with strong reduction agents such as sodium borohydride (NaBH_4) [32]. This method usually produces the nanoparticles with sizes between 5 nm and 20 nm. Wider size distribution of the silver nanoparticles can be obtained by the reduction process which involves using citrate ions [32]. The former reducing agents are also employed for the preparation of gold nanoparticles (AuNP) with widely used Turkevitch-Frens method [34, 35]. The size of the AuNP prepared by the mentioned procedure is around 20 nm. The other very efficient technique is the Brust-Schiffrin method [36, 37] that produces gold nanoparticles with sizes in 1.5 nm – 5.2 nm range, while the size of the nanoparticles can be tuned by the change in the initial concentration of the reagents. In this procedure, the AuCl_4^- ions are being transferred to organic phase (toluene) by using tetraoctylammonium bromide. After that, NaBH_4 is used for the reduction and alkanethiols are employed for stabilization of the colloid. Besides NaBH_4 and citrates, noble metal nanoparticles can be obtained by using other reducing agents such as hydrazine [38], hydrogen [39] or mono- and disaccharides [40].

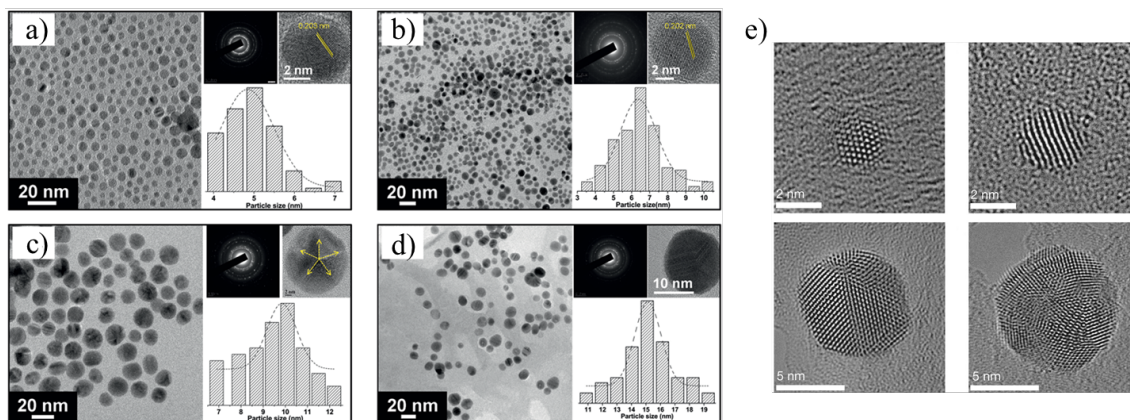


Figure II.1.1. The electron microscopy images (TEM, aberration corrected TEM and HRTEM) and the corresponding particle size distribution histogram of the Ag NP (a–e). Adapted from [41, 42]

Figure II.1.1a-d shows typical TEM images of the silver nanoparticles (AgNPs) obtained by reduction of silver salts using strong reducing agents [41]. Usually, this method produces the

nanoparticles spherical in shape with relatively narrow size distribution.. The selected-area electron diffraction (SAED) patterns demonstrated the concentric diffraction rings as bright spots corresponding to the presence of (111), (200), (220), (311), and (222) planes of the face-centered cubic (fcc) silver crystals. High resolution TEM (HRTEM) micrographs of the single particle show the presence of lattice fringes separated by so-called d -spacing. For particles with the average size 5 and 7 nm, most of the population consists of single crystalline AgNPs with a d -spacing of 2.02 Å, which corresponds to the (200) plane of silver. For the silver nanoparticles with higher average particle diameter (≥ 10 nm), HRTEM images show the presence of multiple-twinned crystalline planes. The transformation of single crystalline AgNPs to multiple twinned particles indicates that silver nuclei/particles formed at the first stage undergo Ostwald ripening in the second stage and are transformed into larger silver nanoparticles, thus completing the growth process [42].

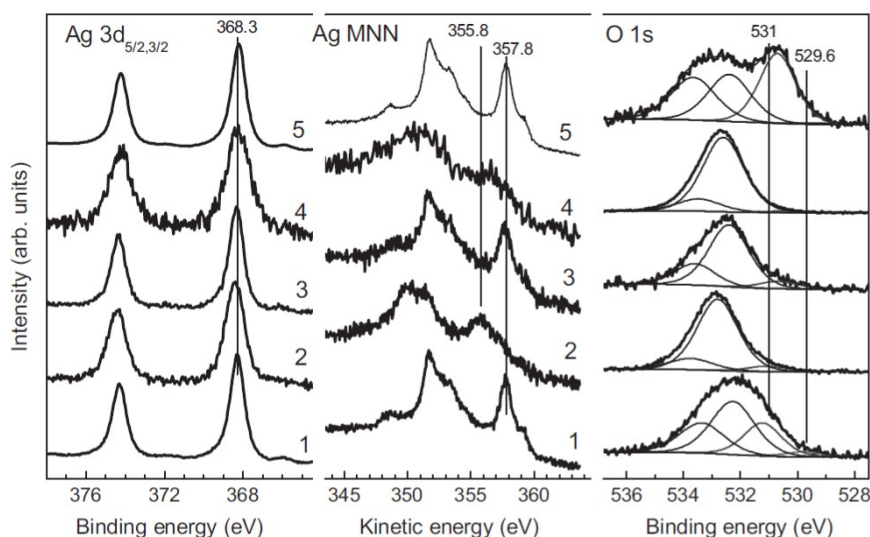


Figure II.1.2. X-ray photoelectron spectra normalized to height from silver NPs prepared with (1) $\text{AgNO}_3/\text{NaBH}_4 = 1$, (2) $\text{AgNO}_3/\text{NaBH}_4 = 10$, (3) $\text{AgNO}_3/\text{Na}_3\text{cit}/\text{NaBH}_4$, (4) $\text{AgNO}_3/\text{glucose}$, and (5) polycrystalline Ag plate, deposited on HOPG. Adapted from [43]

The influence of size and capping of silver nanoparticles on their surface chemistry has been investigated by using X-ray photoelectron spectroscopy (XPS). In a reported study [43] AgNPs of different sizes were obtained by using different concentrations of reducing agents and by capping the particles with glucose. In Figure II.1.2, the Ag $3d_{5/2,3/2}$ doublet spectra with the Ag $3d_{5/2}$ peak at binding energy (BE) of 368.3 eV demonstrate that all the particles are composed preferentially of metallic silver [44-47]. Full width at half maximum (FWHM) of the Ag $3d_{5/2}$ bands varies from 0.86 eV to 1.3 eV for different Ag NPs. The broadening

implies the presence of oxidized silver, which is negligible for silver plate and pronounced for Ag NPs. Auger Ag MNN peaks shifted to lower kinetic energies from the value of 357.8 eV typical for elemental silver suggest that the oxidized Ag species occur mainly on the surface of smaller NPs. An increase in a positive charge localized at Ag atoms commonly results in decreasing binding energies (BE) of Ag 3d lines and enhancing kinetic energies of the Auger band [48–50]. O 1s spectra contain strong bands from physically and chemically adsorbed water, C-OH groups in glucose and citrate, O- containing groups on the HOPG surface and adventitious impurities. Oxygen species interacting with Ag, in particular, OH chemisorbed on Ag (531.2 eV), electrophilic O β atoms dissolved in Ag⁰ lattice (~530.8 eV) or localized on the metal surface (~530.5 eV) are observable at lower BE. The ratios of surface OH group and electrophilic oxygen O β to Ag are in the range 0.19–0.5; the values are lower for capped nanoparticles and for smaller ones due to the presence of capping agents and adsorbed water. The exposure of the larger Ag NPs at atmosphere for longer periods of time induces a slow increase in the width of Ag 3d and Ag MNN bands, while the changes in the O 1s spectra of smaller silver clusters are less straightforward owing to complex transformations of surface Ag O species [47]. XPS and Auger spectra show that near-surface concentrations of Ag(I) species for the functionalized AgNPs are higher than for uncapped ones of the same diameter. The smaller AgNPs more easily enter into oxidation-reduction reactions.

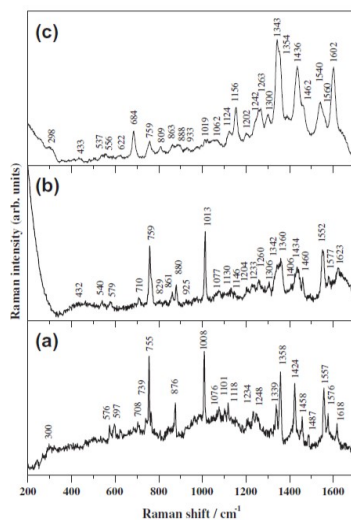


Figure II.1.3. Raman spectrum of tryptophan in a) solid and b) alkaline solution, and c) SERS of silver-tryptophan in the region 200-1700 cm^{-1} . Adapted from [51]

Surface-enhanced Raman scattering (SERS) is a surface sensitive technique in which the enhancement of Raman scattering is achieved by adsorbing molecules on the rough metallic

surfaces [52, 53]. Shifts in vibrational frequencies and relative intensities in the spectra of adsorbed molecular species compared to that in solution provide information on the average conformation of the adsorbed molecule and the relative proximity of different parts of the adsorbed molecule to the surface. In one example relevant to this dissertation, Nandita Maiti et al [51] investigated tryptophan-silver complex by the means of DFT and SERS. In Figure II.1.3 is the Raman spectrum of solid and alkaline solutions of tryptophan and SERS of tryptophan functionalized silver nanoparticles. The adsorption of tryptophan on the silver surface can occur either via physisorption or chemisorption. In case of latter, due to the overlap of the molecular and metal orbitals, the molecular structure is modified resulting in shifts in the Raman bands and changes in their intensities [54]. The SERS spectrum of silver-tryptophan [Figure II.1.3c] indicates significant changes comparing to the pure tryptophan solution spectrum, indicating chemisorption of the tryptophan over the silver surface. The formation of a charge-transfer complex between tryptophan and silver is further supported from the plot of frontier molecular orbitals, HOMO and LUMO of the tryptophan-silver complex, where there is significant interaction between the occupied indole ring and the unoccupied silver ion leading to the formation of stable tryptophan- Ag^+ complexes [51]. The adsorption of tryptophan on the silver surface also depends on the active sites of the molecule through which the binding takes place and can be estimated from the enhancement of the relevant Raman bands according to the electromagnetic surface selection rules. The higher the negative charge density on the atom, the higher is the possibility of the atom to act as an adsorptive site for silver substrate. The negative charge density is more appreciable on the oxygen atoms of the carboxylate group, which acts as the most probable active site for binding to Ag^+ . The SERS spectrum shows huge enhancement in the vibration at 1343 cm^{-1} (CO_2^- sym. stretch) along with remarkable red shift confirming binding directly through the carboxylate group. The enhancement in 1343 cm^{-1} is followed by increase in intensities of 1602 , 1540 , 1436 , 1354 , 1263 , 1156 , and 684 cm^{-1} vibration. The increase in intensity is thus, observed mainly in the in-plane ring stretching, breathing and bending vibrations along with carboxylate stretch and bend. Contributions from NH bend are suggesting the presence of the form of tryptophan-silver complex with an edge-on orientation with the indole ring lying perpendicular to the silver surface.

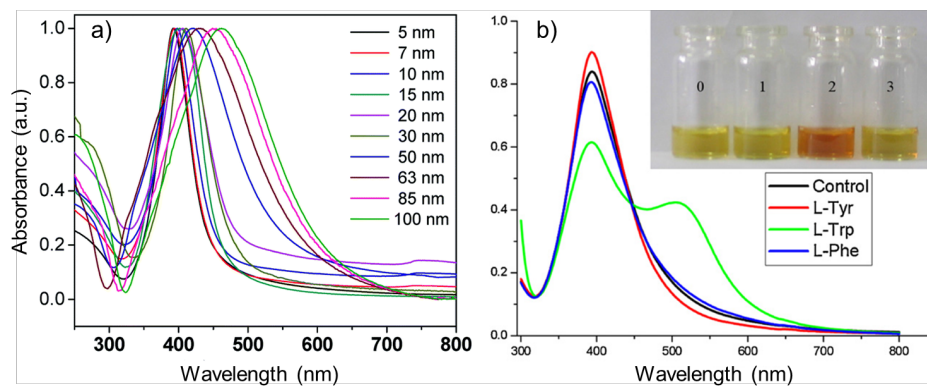


Figure II.1.4. a) UV-vis extinction spectra for different sized AgNPs b) UV-vis spectra of 4-DPD-AgNPs solution containing 3 kinds of neutral amino acids (red: tyrosine, green: tryptophan, blue: phenylalanine). The inset shows the photographic images of hydrocolloids (from 0 to 3, they are Control, tyrosine, tryptophan and phenylalanine, respectively). Adapted from [41, 55]

Figure II.1.4a shows the UV-vis absorption spectra of the silver nanoparticles of various sizes (5-100 nm). The spectra exhibit a sharp extinction peak in 393-462 nm wavelength range which is typical for the surface plasmon resonance (SPR) absorption of AgNPs. As can be seen, the absorption maxima of AgNPs shifted to longer wavelength with increase in AgNP size. The full width at half maximum (FWHM) of the SPR peaks is the measure of the size dispersity of the nanoparticles. By adding tryptophan to hydrocolloids of silver nanoparticles, the morphology changes in terms of aggregation. This is further reflected in changes in their optical properties, as we observe additional band at longer wavelength (Figure II.1.4b). For this reason, the color of the colloid changed from yellow to red. As shown in Figure II.1.4b, there is a slight shift in the position of the absorption peak towards higher wavelengths after the functionalization, which indicates that the tryptophan is attached onto silver nanoparticles. It has been proved that the adsorption of organic compounds on the metal nanoparticles will result in a redshift in the SPR band, due to the reducing of the plasma oscillation frequency as well as due to the change in the dielectric constant of the microenvironment around the nanoparticles.

Functionalization of silver nanoparticles with tryptophan does not change the chemical composition of tryptophan, since no oxidation was observed [51]. Therefore, the physical properties of tryptophan, such as the ability to absorb and emit light stay preserved and they were transferred to the hybrid nanostructures. However, it is important to address the influence of metal nanoparticles on the fluorescence properties of tryptophan and other amino acids.

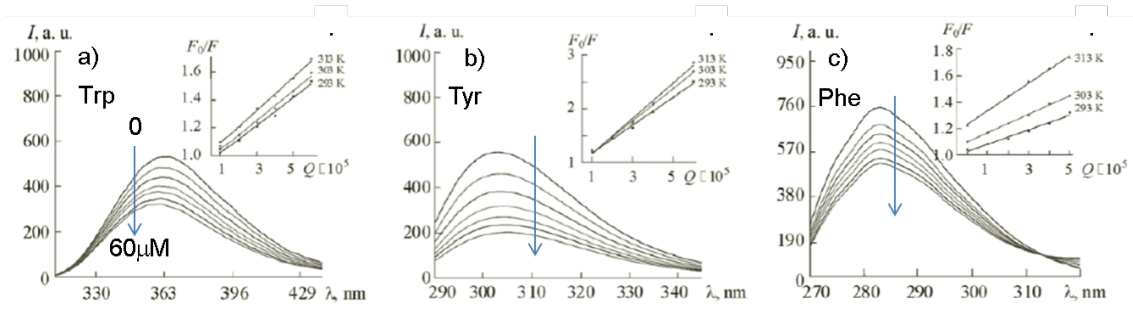


Figure II.1.5. Emission spectra of tryptophan (a), tyrosine (b), and phenylalanine (c) in the presence of different concentrations of silver nanoparticles (0, 10, 20, 30, 40, 50, and 60 μM). Insets show Stern–Volmer plot of amino acids–silver nanoparticles interaction. Adapted from [56]

Figure II.1.5 shows the emission spectra of tryptophan, tyrosine, and phenylalanine in the presence of various concentrations of silver nanoparticles. The fluorescence intensities of tryptophan, tyrosine, and phenylalanine decrease sharply with increasing in concentration. This indicates that the silver nanoparticles interacted with tryptophan, tyrosine, and phenylalanine, which resulted in quenching of the fluorescence intensity. The observed effect is a consequence of damped oscillations of molecular dipoles by the surrounding metal nanoparticles and absorption of emitted light by the particle's surface plasmon. Fluorescence quenching denotes any process that reduces the fluorescence intensity of a sample. A variety of molecular interactions results in quenching, including excited-state reactions, molecular rearrangements, energy transfer, ground-state complex formation, and collisional quenching [57]. Fluorescence quenching can be dynamic, due to collisional encounters between the fluorophore and quencher, or static, due to the formation of a ground-state complex between the fluorophore and the quencher.

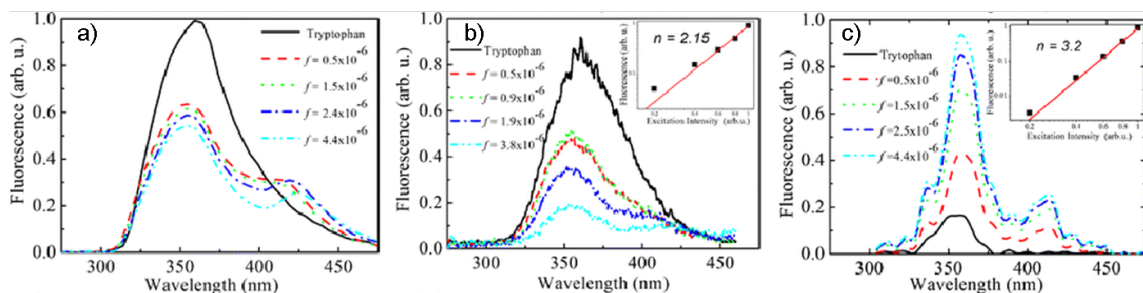


Figure II.1.6. Fluorescence spectra of hydrocolloids of tryptophan and AgNPs excited with a) 270 nm, b) 540 nm, and c) 800 nm. The insets on b and c show the fluorescence peak intensity as function of the excitation intensity. The f -values are representing concentrations of AgNPs. Adapted from [58]

The fluorescence spectra of tryptophan water solutions with and without silver nanoparticles obtained by excitation with one, two and three photon processes is shown in Figure II.1.6. The fluorescence spectra of the colloids pumped with one photon at 270 nm are presented in Figure II.1.6a. Again, a quenching of the amino acid emission occurs as AgNPs concentration increases. The fluorescence of the tryptophan can also be partially absorbed by the AgNPs plasmon band (at 400 nm) creating a valley on the emission spectrum. The tryptophan fluorescence is governed by the magnitudes of the radiative rate, the sum of the nonradiative decay rates, and the lifetime of a fluorophore. Metal–molecule interaction can lead changes on the quantum yield and lifetime of the fluorescent molecule, expressed by an increase in the radiative and nonradiative rates of the system [59]. Similar behavior was also observed when the colloid is excited by a two photon light absorption process (Figure II.1.6.b). The inset shows that the fluorescence's intensity of the tryptophan solution has a square dependence from the laser pump intensity (at 532 nm), consistent with simultaneous absorption of two photons. Although, one photon at 270 nm and two photons at 532 nm are resonant with the excited states of the molecule, these wavelengths are not in resonance with the plasmon energy level. The fluorescence spectra of the colloids pumped with three photons at 800 nm are shown in Figure II.1.6.c. The excitation of the solution with the 800 nm laser requires a simultaneous absorption of three photons. This is confirmed by a cubic dependence of the tryptophan's emission intensity from the intensity of the 800 nm pump beam (Figure II.1.6c inset). In that case, the fluorescence emission is enhanced with the addition of NPs into the solution. It is suggested that the presence of nanoparticles introduces new relaxation pathways and a new energy level in the solution which matches with the energy of two photons at 800 nm, providing an enhancement for absorption of a third photon by the amino acid [58].

The interactions of fluorophores with metallic surfaces can have a number of useful effects, including increased quantum yields, sensitivity, photostability as well as decreased lifetimes and decreased interference from unwanted background emission. Because quenching and enhancement mechanism of the fluorophores by the noble metal nanoparticles is used in biosensing and bioanalytical applications, we will elaborate them in more detail. Fluorescent substance (fluorophore) in the excited state has the resembling properties of an oscillating dipole. The excited fluorophore can influence oscillations of the electrons in the metal. Simultaneously, the electric field created by the metal can interact with the excited fluorophore and alter its emission. These effects can be understood by considering a Jablonski diagram that includes the concept of metal-enhanced fluorescence (Figure II.1.7a).

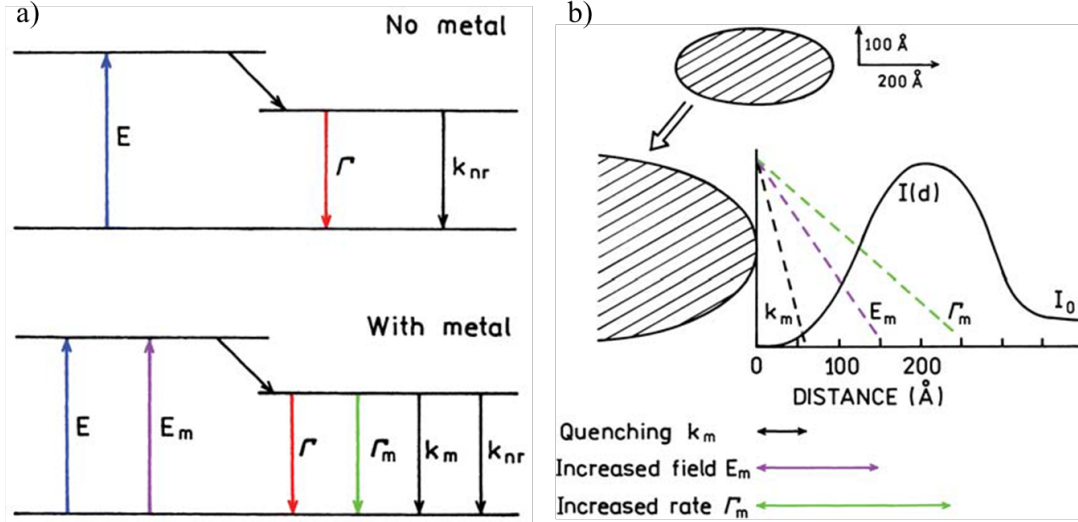


Figure II.1.7. a) Jablonski diagram without and with the effects of metal surfaces. b) Metallic particles can cause quenching, enhanced focusing of the incident light field and can increase the radiative decay rate. Adapted from [2]

In the absence of metals the quantum yield (Q_0) and lifetimes (τ_0) are given by

$$Q_0 = \Gamma / (\Gamma + k_{nr}), \quad \text{Eq.II.1.}$$

$$\tau_0 = (\Gamma + k_{nr})^{-1}, \quad \text{Eq.II.2.}$$

where Γ is the radiative decay and k_{nr} is non-radiative decay. Since the radiative decay rate is nearly constant for any fluorophore the quantum yield can only be increased by decreasing the value of k_{nr} . If the effect on metal results in an increased rate of excitation ($E + E_m$) this will result in increased brightness without changing the quantum yield or lifetime. This is a useful effect that can allow using decreased intensities of the incident light and reduce the background. Metal-enhanced excitation can also result in selective excitation of fluorophores near the metal. Another possible effect is an increase in the radiative decay rate. In this case the quantum decay yield and lifetime of the fluorophore near the metal surface are given by

$$Q_m = (\Gamma + \Gamma_m) / (\Gamma + \Gamma_m + k_{nr}) \quad \text{Eq.II.3.}$$

$$\tau_m = (\Gamma + \Gamma_m + k_{nr})^{-1} \quad \text{Eq.II.4.}$$

As the value of Γ_m increases the quantum yield increases while the lifetime decreases. When the total decay rate ($\Gamma_T = \Gamma + \Gamma_m$) increases the quantum yield increases. The increase occurs because more of the fluorophores emit before they can decay through the non-radiative pathway. The effect is larger for fluorophores with low quantum yields because increasing Γ_m does not affect Q if it is already unity. The proposed model assumes that there are three dominant interactions of fluorophores with metals (Figure II.1.7b). Fluorophores may be

quenched at short distances from the metal surfaces (k_m), but there may be other ways to recover this energy as a useful emission. An increased rate of excitation (E_m) (so-called the lightning-rod effect), and an increased rate of radiative decay (Γ_m) may be observed at higher distances..

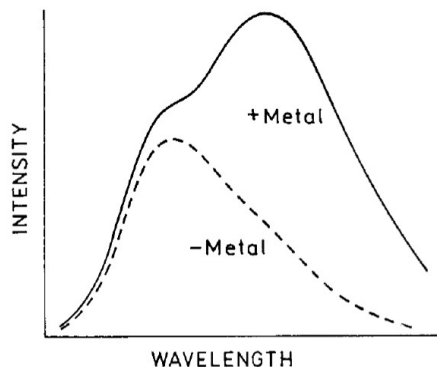


Figure II.1.8. Effect of an increased radiative rate on a protein with two tryptophan residues, one of which has a low quantum yield. Adapted from [59]

The effect of increased rate of radiative decay competes more effectively with quenching and takes place at shorter distances. Therefore, emission from the quenched fluorophores will be observable in vicinity of the metal particles. For a protein that has two tryptophan residues, the surface exposed is strongly quenched by a local quenching interaction. In the absence of metal, emission will only be observed from the higher quantum yield residue emitting at shorter wavelengths (Figure II.1.8). When the protein is close to a metal particle, both residues will emit faster. However, the quantum yield of the quenched residue will be increased to a higher extent. Hence, the spectral shape will change due to an increased in intensity at shorter wavelengths from the increased quantum yield of the quenched residue.

Biological molecules contain a number of intrinsic fluorophores. A substantial fraction of intrinsic fluorophores are quenched. For example, flavins are fluorescent in solution, but most flavoproteins display little if any flavin emission [60–62]. Tyrosine is often quenched in proteins, and frequently tryptophan residues are quenched by nearby amino acid residues such as disulfide bonds, histidine, or phenylalanine side chains [63–65]. Another well-known example is DNA, nucleotides, and the individual bases. While some intrinsic emission has been reported [66, 67], the intrinsic fluorescence from the five common nucleic acid bases is very weak. The surface effects may produce more intense emission from all these intrinsic fluorophores. Flavoproteins adjacent to metal surfaces may become fluorescent as the increased radiative rates become comparable in magnitude to the quenching rates. Similarly,

quenched residues in proteins or DNA may display useful emission if the radiative rates can be made comparable to the nonradiative decay rates. Since significant enhancements of fluorescence have been observed, there is a reason to expect similar results can be obtained for DNA.

II.1.2. Fluorescent nanostructures based on biomolecule functionalization of noble metal nanoparticles

Attaching biomolecules on the surface of NPs is of great importance in developing biocompatible platforms for various biomedical applications. Proteins that have certain charge can be directly deposited on the surfaces of oppositely charged nanoparticles through electrostatic interactions [68]. For the purpose of cancer therapy, when nanoparticle is functionalized with specific biomolecule, it is recognized by the receptors that are located on the plasma membrane, and internalized via receptor-mediated endocytosis. These receptors are unique to specified cells or related to certain diseases, and therefore, they have frequently been used as a tool to increase the drug load within the unhealthy cell. This concept is used in designing nanodevices and nanomaterials for sensing and other associated applications. Various molecules such as folic acid, DNA, proteins, oligonucleotides and others ligand specific molecules are used in surface functionalization of nanoparticles (Figure II.1.9).

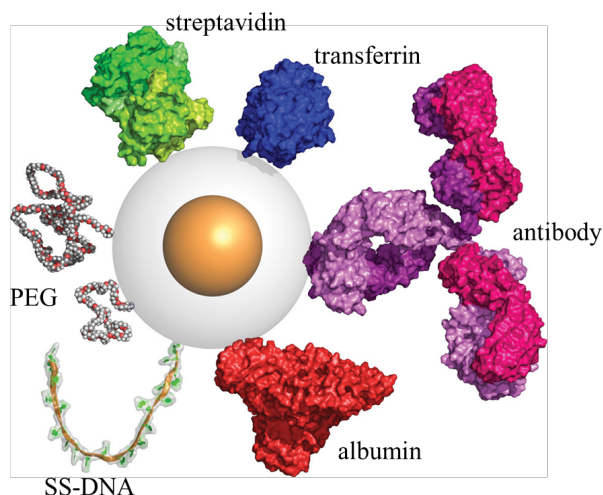


Figure II.1.9. Schematic illustration of a nanoparticle with 5 nm core diameter, 10 nm shell diameter, with PEG molecules of 2000 and 5000 g mol⁻¹ (on the left, light grey), streptavidin (green), transferrin (blue), antibody (IgG, purple), albumin (red), single-stranded DNA (20mer, cartoon and space filling). Adapted from [69]

Detection of DNA using fluorescence is almost always performed using extrinsic probes, because the intrinsic fluorescence of the DNA bases is very weak. Silver particles were found to increase the intrinsic fluorescence of unlabeled DNA [70]. DNA hybridization is frequently measured using fluorophores that display increased intensity when bound to double-helical DNA. Metal-enhanced fluorescence allows the measurement of the hybridization using fluorophores for which the quantum yield, in the absence of metal, does

not change upon DNA hybridization [70]. The increase in fluorescence intensity is not because of the effect of hybridization, it is due to the localization of the probe near the silver structures. This result shows that metal-enhanced fluorescence can be used to detect any binding reaction that tends to bring fluorophore closer to silver structure.

For the fluorophores with a small Stokes shift used as the protein label, the intensity does not increase proportionally to the number of bound fluorophores, and sometimes the intensity decreases. Proper distance between heavily labeled biomolecules to silver surfaces can result in increased fluorescence intensities and apparently less self quenching due to homo resonance energy transfer [2]. Correspondingly, resonance energy transfer can be used to measure DNA hybridization if the donor and acceptor are within about 15 base pairs, but will not occur if the donor and acceptor are spaced by a much larger number of base pairs. The proximity to metal particles can increase the extent of energy transfer [71]. The effect of silver surface on resonance energy transfer was studied using a double-stranded DNA oligomer labeled with AMCA as the donor and Cy3 as the acceptor. The DNA oligomers labeled with both donor and acceptor were placed either near a single silver island film or between two silver islands films. The resonance energy transfer efficiency was not affected by a single island film, but was increased when the donor-acceptor pair was between two films. Lu et al. [72] designed a fluorescence resonance energy transfer (FRET) system containing gold nanorods (AuNRs) and fluorescein amidite (FAM) for the detection of hepatitis B virus DNA sequences. The fluorescence coming from FAM is quenched successfully by AuNRs present in the sample. Hence, any interaction of target molecules with NRs gets back the original FAM fluorescence.

Theranostics based on anisotropic noble metal nanoparticles are emerging as a promising therapeutic model because of their ability in diagnosis, drug delivery, and monitoring therapeutic responses. They have been intensively investigated as theranostics in cancer therapy, especially for photo-chemotherapy, because of two important features: (i) chemotherapeutics and various functional ligands (for targeting cancer cells) can be easily attached to the nanoparticles through surface reactive groups of the capping agents (e.g. amino group, and carboxyl group), and (ii) presence of SPR bands in the NIR region, which induces photothermal conversion by converting the absorbed light to heat when it matches with the wavelength of irradiation light. Availability of a wide variety of noble metal nanoparticles (e.g. NRs, NSs, nanodisks, nanoshells, nanocages, and hollow nanospheres) as well as cancer specific ligands (e.g. antibodies, biomolecules, and proteins) makes them promising candidates for theranostics in cancer therapy. Photo thermal therapy (PTT) is the

minimally invasive therapeutic approach in which the photon energy is directly used to generate heat (with the use of plasmonic nanoparticles) to destroy cancer cells. In photodynamic therapy (PDT) that battles cancer cells, the singlet oxygen ($^1\text{O}_2$) is formed by the influence of light on photosensitizer and it leads to cancer cell death [73]. PDT mediators can be highly localized in tumors. For example, PEGylated gold nanoparticles conjugates have been used to deliver PDT agents effectively to the target site [74]. The delivery of PDT agents with PEGylated gold NP conjugates is observed as quenching of the fluorescence of PDT agent until the delivery at the target site. The use of noble metal nanoparticles improves the effectiveness of PTT many folds as it enhances heat generation under the absorption of NIR light. By utilizing the EPR effect in cancerous cells, nanoparticles can be targeted passively to cancer cells. The use of plasmonic anisotropic nanoparticles lets light of longer wavelengths to be used, which helps reduce the damage to normal cells [75, 76].

Single gold nanorod was used as a contrast agent for optical microscopy and two-photon fluorescence (TPF) imaging [77]. Conventional fluorescence microscopy uses a single photon to excite one fluorescent molecule; two photon microscopy uses two photons of half the energy (i.e. double the wavelength) to excite one fluorescent molecule. When gold nanorods are used as probes in two photon microscopy, the scattering cross sections obtained are much stronger than those of conventional fluorescent molecules. This results in contrast enhancement and better resolution of the fluorescence images. It is reported that the signal from a single gold NR is 58 times brighter than the two-photon fluorescence signal arising from single rhodamine molecule [77].

The properties such as strong surface plasmon resonance (SPR), biocompatibility, and other surface properties, made noble metal nanoparticles good candidate for various biological applications. For example, surface modified noble metal nanoparticles have been used as contrast markers in sensitive detections, and as replacements of conventional organic and molecular fluorescent probes [2]. The absorption of metallic nanospheres in biological window ([650-900] nm) enabled them to be used for reduced non-invasive in vivo imaging. Also, anisotropic noble metal nanoparticles in the electromagnetic window ([800-1300] nm) can be employed for drug delivery, diagnostics and photothermal therapy [78].

References

- [1] M. Chen and M. Yin, *Progress in Polymer Science* 39(2) (2014) 365.
- [2] J. R. Lakowicz, *Principles of Fluorescence Spectroscopy* (Springer, New York, 2006.).
- [3] O. S. Wolfbeis, *Chemical Society Reviews* 44 (2015) 4743.
- [4] Z. Tang et al., *Progress in Polymer Science*, 60 (2016) 86.
- [5] J. Conde, G. Doria and P. Baptista, *Journal of Drug Delivery*, 751075 (2012).
- [6] R. R. Arvizo et al., *Chemical Society Reviews* 41(7) (2012) 2943.
- [7] G. Doria et al., *Sensors* 12(2) (2012) 1657.
- [8] P. K. Jain, X. Huang, I. H. El-Sayed and M. A. El-Sayed, *Plasmonics* 2(3) (2007) 107.
- [9] K. P. Loh et al., *Nature Chemistry* 2 (2010) 1015.
- [10] C. Galande et al., *Scientific Reports* 1 (2011) 85.
- [11] G. Eda et al., *Advanced Materials* 22 (2010) 505.
- [12] X. Sun et al., *Nano Research* 1 (2008) 203.
- [13] Z. Luo et al., *Applied Physics Letters* 94 (2009) 111909.
- [14] E. Morales-Narvaez and A. Merkoci, *Advanced Materials* 24 (2012) 3298.
- [15] P. V. Kumar, M. Bernardi and J. C. Grossman, *ACS Nano* 7(2) (2013) 1638.
- [16] P. Kalluru et al., *Biomaterials*, 95 (2016) 1.
- [17] D. Pomogailo and V. N. Kestelman, *Metallopolymer Nanocomposites* (Springer-Verlag, Berlin - Heidelberg 2005.).
- [18] E. Wiberg, A. F. Holleman and N. Wiberg, *Lehrbuch der Anorganischen Chemie* (Walter de Gruyter GmbH, Berlin, 2009.).
- [19] N. W. Ashcroft and N. D. Mermin, *Solid State Physics* (Harcourt College Publishers, Fort Worth, 1976.).
- [20] V. V. Vodnik, D. K. Božanić, N. Bibić, Z. V. Šaponjić and J. M. Nedeljković, *Journal of Nanoscience and Nanotechnology* 8 (2008) 3511.
- [21] L. Yang et al., *Applied Physics Letters* 78 (2001) 102.
- [22] J. Hu, B. Zhao, W. Xu, B. Li and Y. Fan, *Spectrochimica Acta A* 58 (2002) 2827.
- [23] C. F. Mao, M. A. Vannice, *Journal of Catalysis* 154 (1995) 230.
- [24] V. K. Sharma, R. A. Yngard and Y. Lin, *Advances in Colloid and Interface Science* 145 (2009) 83.
- [25] P. V. AshaRani, G. L. Kah Mun, M. P. Hande and S. Valiyaveetil, *ACS Nano* 3 (2009) 279.
- [26] R. Kannan et al., *Journal of the American Chemical Society* 128 (2006) 11342.
- [27] D. R. Bhumkar, H. M. Joshi, M. Sastry and V. B. Pokharkar, *Pharmaceutical Research* 24 (2007) 1415.
- [28] X. Zhou et al., *Biomaterials* 29 (2008) 111.
- [29] C. Loo, A. Lowery, N. Halas, J. West and R. Drezek, *Nano Letters* 5 (2005) 709.
- [30] W. J. Parak, L. Manna, F. C. Simmel, D. Gerion, and P. Alivisatos, *Nanoparticles - From Theory to Application*, Ed. G. Schmid, (Wiley-VCH, Weinheim, 2004.)
- [31] D. K. Božanić, Fizičke osobine nanokompozitna skroba sa metalnim i poluprovodničkim nanočesticama, Magistarska teza, Univerzitet u Beogradu, Beograd, Februr 2008.
- [32] J. A. Creighton, C. G. Blatchford, and M. G. Albrecht, *Journal of the Chemical Society, Faraday Transactions 2* (2001) 790.
- [33] P.C. Lee, D. Meisel, *Journal of Physical Chemistry* 86 (1982) 3391.
- [34] J. Turkevitch, P.C. Stevenson, J. Hillier, *Discussions of the Faraday Society* 11 (1951) 55.
- [35] G. Frens, *Nature: Physical Science* 241 (1973) 20.
- [36] M. Brust, M. Walker, D. Bethell, D. J. Schiffrin, and R. J. Whyman, *Journal of Chemical Society Chemical Communication* 801 (1994).
- [37] M. Brust, J. Fink, D. Bethell, D. J. Schiffrin, C. J. Kiely, *Journal of Chemical Society Chemical Communication* 1655 (1995).
- [38] K. Esumi, N. Ishizuki, K. Torigoe, H. Nakamura, and K. Meguro, *Journal of Applied Polymer Science* 44 (1992) 1003.
- [39] U. Nickel, A. Z. Castell, K. Poppl, and S. Shneider, *Langmuir* 16 (2000) 9087.
- [40] Panacek, L. Kvitek, B. Prucek, M. Kolar, R. Vecerova, N. Pizurova, V. K. Sharma, T. Nevezna, and R. Zboril, *Journal of Physical Chemistry B* 110 (2006) 16248.
- [41] S. Agnihotri, So. Mukherji and Su. Mukherji, *RSC Advances* 4 (2014) 3974.
- [42] J. A. Scholl, A. L. Koh and J. A. Dionne, *Nature* 483 (2012) 421.
- [43] Y. L. Mikhlin et al., *Applied Surface Science* 297 (2014) 75.
- [44] V. I. Bukhtiyarov, A. F. Carley, L. A. Dollard and M. W. Roberts, *Surface Science* 381 (1997) L605.
- [45] V. I. Bukhtiyarov and V.V. Kaichev, *Journal of Molecular Catalysis A* 158 (2000) 167.

- [46] L. S. Kibis, A. I. Stadnichenko, E. M. Pajetnov, S. V. Koscheev, V. I. Zaykovskii, A. I. Boronin, *Applied Surface Science* 257 (2010) 404.
- [47] T. C. R. Rocha, A. Oestereich, D. V. Demidov, M. Hävecker, S. Zafeiratos, G. Weinberg, V. I. Bukhtiyarov, A. Knop-Gericke, and R. Schlögl, *Physical Chemistry Chemical Physics* 14 (2012) 4554.
- [48] E. R. Savinova, D. Zemlyanov, B. Pettinger, A. Scheybal, R. Schlögl, and K. Doblhofer, *Electrochimica Acta* 46 (2000) 175.
- [49] E. R. Savinova, A. Scheybal, M. Danckwerts, U. Wild, B. Pettinger, K. Doblhofer, R. Schlögl and G. Ertl, *Discussions of the Faraday Society* 121 (2002) 181.
- [50] D. Lützenkirchen-Hecht and H. H. Strehblow, *Surface and Interface Analysis* 38 (2006) 686.
- [51] N. Maiti, S. Thomas, J. A. Jacob, R. Chadha, T. Mukherjee and S. Kapoor, *Journal of Solid and Interface Science* 380 (2012) 141.
- [52] R. K. Chang, T.E. Furtak (Eds.), *Surface Enhanced Raman Scattering*, Plenum, New York, 1982.
- [53] M. Moskovits, *Reviews of Modern Physics* 57 (1985) 783.
- [54] Campion and P. Kambhampati, *Chemical Society Reviews* 27 (1998) 241.
- [55] H. Li, F. Li, C. Han, Z. Cui, G. Xie and A. Zhang, *Sensors and Actuators B: Chemical* 145 (2010) 194.
- [56] S. Roy and T. K. Das, *Journal of Applied Spectroscopy* 82(4) (2015) 598.
- [57] C. X. Wang, F. F. Yan, Y. X. Zhang, and L. Ye, *Journal of Photochemistry and Photobiology A* 192 (2007) 23.
- [58] D. Rativa, A. S. L. Gomes, S. Wachsmann-Hogiu, D. L. Farkas and R. E. de Araujo, *Journal of Fluorescence* 18 (2008) 1151.
- [59] J. Lakowicz, *Analytical Biochemistry* 298(1) (2001) 24.
- [60] P. A. W. van den Berg, A. van Hoek, C. D. Walentas, R. N. Perham, and A. J. W. G. Visser, *Biophysical Journal* 74 (1998) 2046.
- [61] J. Visser, S. Ghisla, V. Massey, F. Muller and C. Veeger, *European Journal of Biochemistry* 101(1) (1976) 13.
- [62] J. R. Albani, A. Sillen, Y. Engelborghs and M. Gervais, *Photochemistry and Photobiology* 69(1) (1999) 22.
- [63] J. K. Swadesh, P. W. Mui and H. A. Scheraga, *Biochemistry* 26 (1987) 5761.
- [64] R. Loewenthal, J. Sancho and A. R. Fersht, *Biochemistry* 30 (1991) 6775.
- [65] N. Rouviere, M. Vincent, C. T. Craescu and J. Gallay, *Biochemistry* 36 (1997) 7339.
- [66] S. Georghiou, T. M. Nordlund and A. M. Saim, *Photochemistry and Photobiology* 41(2) (1995) 209.
- [67] R. Plessow, A. Brockhinke, W. Eimer and K. Kohse-Hoinghaus, *Journal of Physical Chemistry* 104 (2009) 3695.
- [68] R. B. Shmueli, D. G. Anderson and J. J. Green, *Expert Opinion on Drug Delivery* 7(4) (2011) 535.
- [69] R. A. Sperling and W. J. Parak, *Philosophical Transactions of the Royal Society A* 368 (2010) 1333.
- [70] J. R. Lakowicz, J. Malicka and I. Gryczynski, *Biotechniques* 34(1) (2003) 62.
- [71] J. Kummerlen, A. Leitner, H. Brunner, F. R. Aussenegg and A. Wokaun, *Molecular Physics* 80 (1993) 1031.
- [72] X. Lu, X. Dong, K. Zhang, X. Han, X. Fang and Y. Zhang, *Analyst* 138(2) (2013) 642.
- [73] W. Fongm H. Yeung, P. Lo and D. K. P. Ng, *Handbook of Photonics for Biomedical Engineering* (2017) 657.
- [74] C. Yao et al., *Journal of Nanomaterials* 2016 (2016) 1.
- [75] D. Jaque et al., *Nanoscale* 6(16) (2014).
- [76] N. Li, P. Zhao and D. Astruc, *Angewandte Chemie* 53(7) (2014) 1756.
- [77] H. Wang et al., *PNAS* 102(44) (2005) 15752.
- [78] G. Paramasivam, N. Kayambu, A. M. Rabel, A. K. Sundramoorthy and A. Sundaramurthy, *Acta Biomaterialia* 49 (2017) 45.

II.2. Graphene oxide and reduced graphene oxide

Graphene oxide (GO) is a two-dimensional (2D) material derived from the parent graphene by introducing, through covalent bonding, several oxygen functionalities. GO is fabricated from starting graphite material by oxidation with strong oxidants in concentrated acid media. The oxidation level of GO depends on the nature of the oxidants and most importantly, on the concentration of the oxidant (graphite to oxidant ratio). Depending on the type of the oxidant and the acidic medium, three major methods for GO preparation can be found in the literature: Brodie's method [1], Staudenmaier's method [2] and the Hummers method [3]. The Hummers method uses potassium permanganate (KMnO_4) as an oxidant in concentrated sulfuric acid medium. Hummers and Offeman claimed that their reaction completes in two hours, thus their method was more effective compared to Brodie's and Staudenmaier's methods. The drawback of the Hummers method is its low efficiency when the large-particle-size powdered graphite is used as a starting material. In that case, an incompletely oxidized graphite-GO hybrid is obtained. The samples prepared by the Hummers approach are normally more oxidized due to the fact that potassium permanganate is a stronger oxidizing agent than potassium chlorate. For this reason, the Hummers method is currently the most used approach for the fabrication of GO, with some modifications related to the particular applications.

During the conversion of the bulk graphite to GO, there are three main steps in the Hummers procedure (Figure II.2.1). The reaction can be stopped at any step, and the corresponding intermediate products can be isolated, characterized and stored under appropriate conditions. The first step is the transformation of graphite to the sulfuric acid-graphite intercalation compound (deep blue color), which begins immediately upon exposing graphite to the acidic oxidizing medium, and it comes to completion within a few minutes. The layer of the intercalant alternates with every graphene layer. The second step is conversion of the intercalation compound to the oxidized form of graphite that was defined as pristine graphite oxide (GtO). The diffusion mechanism of the oxidizing agent between the graphene layers that it needs to replace existing intercalant molecules or insert between them. As soon as the oxidizing agent diffuses between the graphene layers, it reacts with nearby carbon atoms. Thus, the second step of GtO formation is diffusion-controlled, where the oxidizing agent replaces the acid intercalant. The third step of GO formation, i.e. the change of GtO to GO, and it is directed by the exposure to the water during quenching and washing

procedures. As a consequence, there is a loss of the c-axis interlayer registry followed by the exfoliation of GtO into single-atomic-layer sheets. With sufficient oxidation of graphene oxide, mono layer sheets are spontaneously formed with simple stirring in water.

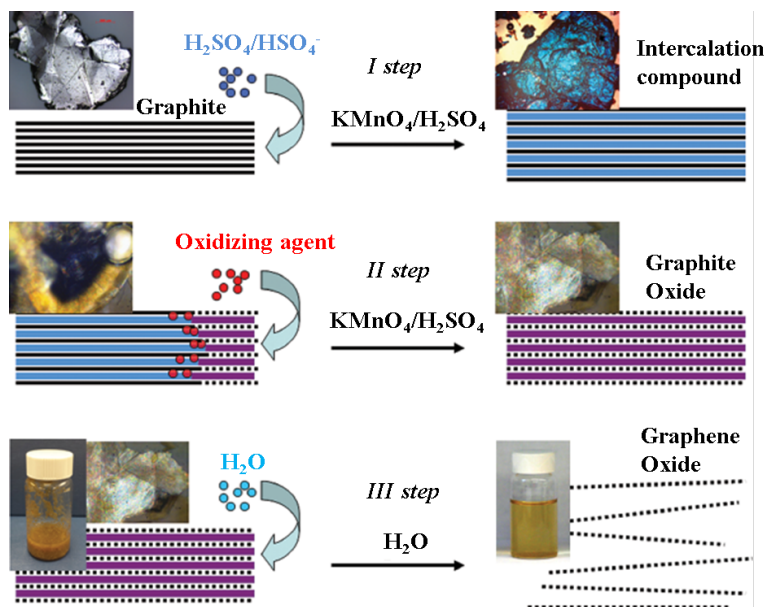


Figure II.2.1. Schematics of the transformation of the bulk graphite into GO with corresponding images of samples at each phase. The three steps signify formation of the two intermediate products (Intermediate compound and GtO) and the final GO product. Graphene layers are represented by the solid black lines; dotted black lines are corresponding to single layers of GO; wide blue lines represent $\text{H}_2\text{SO}_4/\text{HSO}_4^-$ intercalate; wide purple lines represent a layer of the mixture of $\text{H}_2\text{SO}_4/\text{HSO}_4^-$ intercalate with reduced form of oxidizing agent. Adapted from [4]

The current state of graphene production is divided between two approaches – the bottom-up and top-down. In the bottom-up approach graphene sheets are built from scratch, starting with simple carbon molecules such as methane and ethanol. The chemical reduction of graphene oxide (top-down) relies on the fundamental idea of extracting layers of graphene from graphite. The top-down method via chemical oxidation and reduction is the most suitable technique to date, in terms of high yield and low cost. Additionally, graphene obtained via such chemical treatment is important for a large portion of the graphene community that utilizes graphene in applications such as composites, coatings, transparent conductive layers, bioapplications and energy storage [5–7]. There is currently a wide range of reducing agents for graphene oxide in the literature [8]. The reduction compound is usually chosen depending on the later use of the material. The graphene community seeks the fabrication procedures that will result in the highest reduction capability, healing the defective graphene oxide, improving the dispersion stability of the resulting graphene, as well as looks for the environmentally friendly and affordable reducing agents. Recent review on the

chemical reduction of graphene oxide [9] categorizes the reducing methods into two groups: those with the reduction mechanism that is well-supported (understood) and those with proposed mechanism. The so-called ‘well-supported’ mechanisms are related to the reducing agents that have been traditionally applied in synthetic chemistry and have demonstrated well-defined modes of reaction towards specific oxygen functional groups. The most commonly used reducing agents with the well-supported mechanisms are borohydrates, aluminum hydride, hydrazine, hydrohalic acid and sulphur-containing reducing agents. In contrast, there are reducing agents for which definite modes of reaction towards specific oxygen moieties are yet to be established and they belong to the methods with ‘proposed’ mechanisms. For example, they include reducing agents like hydrazine (nitrogen-containing), saccharides (oxygen containing), glycine (amino acid) and other that do not have any definite modes of reaction towards specific oxygen moieties.

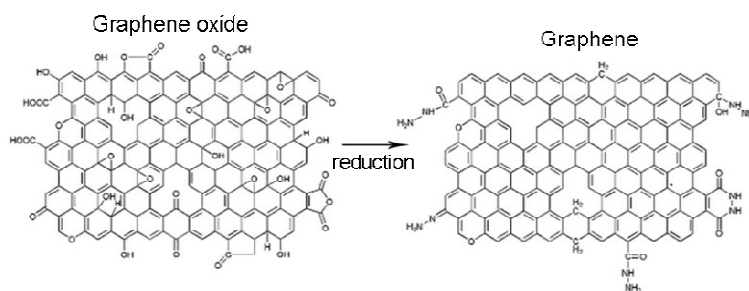


Figure II.2.2. Proposed model for the chemical structure of graphene oxide before and after the reduction. Adapted from [10]

The transformation of the graphene oxide to graphene (or reduced graphene oxide) is indicated by a color change of the reaction mixture from brown-yellow for GO to black for rGO. The increase of hydrophobicity/aggregation of the material occurs as a result of the removal of oxygen containing groups. The decrease in oxygen contents (often represented by an increase of C/O ratio) and the increase in the current conductivity of the graphene material often signify the efficiency of a particular reduction method. Two different types of structures remain on the rGO planes after the reduction: holes and some oxygen functionalities. The holes are formed on GO planes already in the course of its production [11, 12] due to the removal of carbon atoms in the form of carbon dioxide. Additional defects are introduced during the third step of GO formation, i.e. washing of as-prepared GtO with water [13, 14] according to the mechanism presented in (Figure II.2.1). The reduction of graphene oxides yields variety of changes in structural and optical properties which will be addressed in the following subsection (II.2.1).

Most of the GO and rGO layers (or flakes) are too small to be well resolved with an optical microscope. However, electron microscopy techniques generate images that reveal all the structural features of GO and rGO flakes. The morphology of the layers and the structure of graphene oxide are most often probed with scanning electron microscopy (SEM), atomic force microscopy (AFM), and transmission electron microscopy (TEM). SEM provides complete information about the flake size distribution, number of carbon layers, and flake morphology. Typical SEM micrograph of graphene oxide sheet is shown in figure II.2.3a. It has flake like morphology and fairly large diameter. The graphene oxide sheets are almost transparent to the electrons, while overlapping e.g. increasing in thickness can make them appear opaque. The number of the layers can be obtained from the SEM images by using the flake's opacity. The exact thickness of the flake is normally obtained by AFM (Figure II.2.3b,c). When the GO is deposited on the substrate surface, the thickness of the monolayer GO flakes is normally within the 0.8-1.3 nm interval. The size of the oxidized and graphenic domains on GO sheet is in the range from 2 to 4 nm. This is smaller than the tip diameter and that is why AFM cannot resolve two types of domain on the GO platform. The high resolution transmission electron microscopy (HRTEM) technique is usually employed for the additional structural analysis of the graphene-based materials. The spectroscopy techniques (XPS, Raman, UV visible spectroscopy and Photoluminescence spectroscopy) can also provide information about the complex physical properties of the graphene oxide's surface. In the following section, the focus will be on the fluorescent properties of graphene oxide and reduced graphene oxide as well as on the methods of fabrication of the nanostructured graphene-based materials for bioimaging.

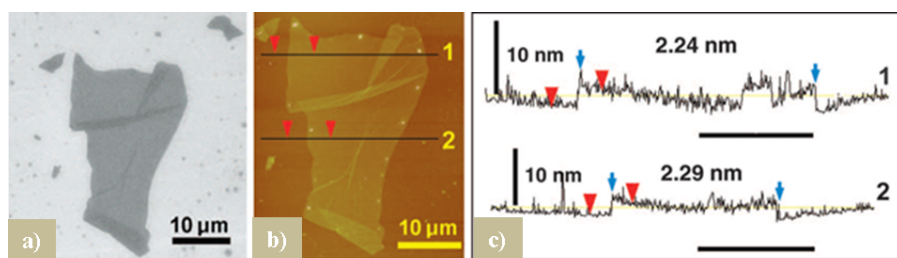


Figure II.2.3. Micrograph of GO flake taken with two microscopy techniques (SEM and AFM). a) SEM image, b) AFM image and c) height profiles of the bilayer GO flake. Adapted from [15]

The physical properties of graphene oxide (GO) and reduced graphene oxide (rGO), are highly dependent on the preparation procedures and they can differ to a great extent. In the present dissertation, the Hummers approach was used for the fabrication of GO, so the emphasis will be on the reported results on structural and optical properties of GO prepared by this particular method, unless noted otherwise.

II.2.1. Structural and optical properties of graphene oxide and reduced graphene oxide

Graphene oxide is a 2d network of sp^2 and sp^3 hybridized carbon atoms organized in a honeycomb lattice with oxygen containing functional groups stochastically distributed over the surface (Figure II.2.4). The oxygen atoms are covalently bonded to carbon atoms, converting them from sp^2 -hybridized state of parent graphene in to the sp^3 -hybridized state. The number of carbon atoms bonded to oxygen exceeds the number of intact sp^2 -hybridized carbon atoms, which makes graphene oxide distinctively different from graphene. Reduced graphene oxide (rGO), as an intermediate material between graphene oxide and graphene, although similar to graphene, it also exhibits some particular properties. The reduction itself is a complex process, but the successful reduction can be easily observed. The GO solution immediately changes its color from yellow-brown to black, due to restoration of the conjugated sp^2 network and the formation of the graphitic structure. However, the original graphene network is never fully restored by the reduction. This is because GO already possesses a high number of defects: the existing defects cannot be healed during the reduction. Carbonyls are the most present oxygen functionalities that remain on GO after chemical reduction. The epoxides and tertiary alcohols are reduced to a certain extent; however, carbonyl groups are difficult to reduce because the formation of carbonyls requires rupture of the C–C bonds. These defects cannot be healed. The ketones in GO can react with small molecules extrinsic to GO; however, they cannot react with carbon atoms from the opposite side of the defects due to the steric hindrance of such a reaction. This is why oxygen functionalities at point defects cannot be removed, and the graphene lattice cannot be fully recovered.

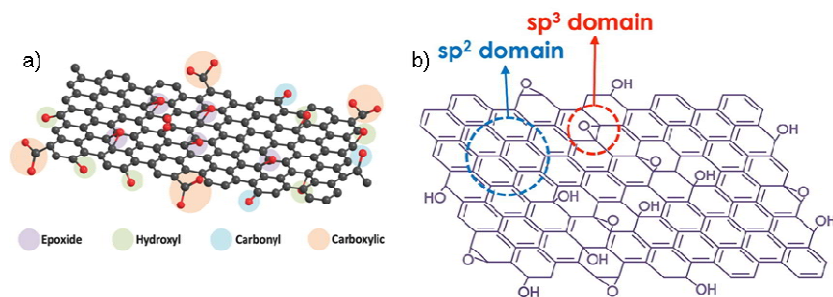


Figure II.2.4. Illustrations of a) oxygen functional groups on the surface of graphene oxide: epoxide, hydroxyl, carbonyl and carboxyl (adapted from [16]) and b) domains of sp^2 and sp^3 hybridized carbon (adapted from [17]).

Figure II.2.5 depicts the high resolution TEM micrographs of graphene, graphene oxide and hydrazine reduced graphene oxide. The oxidation of the parent graphite results in

high number of inhomogeneity that is spreading across the surface. Three different types of domains can be observed in the GO image (Figure II.2.5b): the graphitic domain which formed isolated islands (depicted in yellow-green color), the continuous network of oxidized domains (red-purple color), and the observation of the holes (blue colored). The $<5 \text{ nm}^2$ holes that are present in GO are formed through CO/CO_2 release during the aggressive oxidation and sheet exfoliation [11, 12]. Graphitic regions, covering between 1 and 6 nm^2 , indicate incomplete oxidation of the basal plane with the preserved honeycomb structure and 1.4 Å atomic spacing of graphene. The disordered (high-contrast) oxidized regions of the basal plane form continuous network throughout the GO sheet. Monolayer of rGO (Figure II.2.5c) has qualitatively similar non-homogenous regions in terms of holes, graphitic regions and disordered areas with high contrast. The increase in the area of holes compared to GO is expected as CO and CO_2 form during annealing [12]. The significant increase in graphitic area observed, indicates a substantial restoration of the original sp^2 bonding character lost during the oxidation, by the reduction of oxygen functionalities. Disordered high contrast regions still exist, likely from nitrogen and oxygen functionalities which persist even after the reduction and annealing [18].

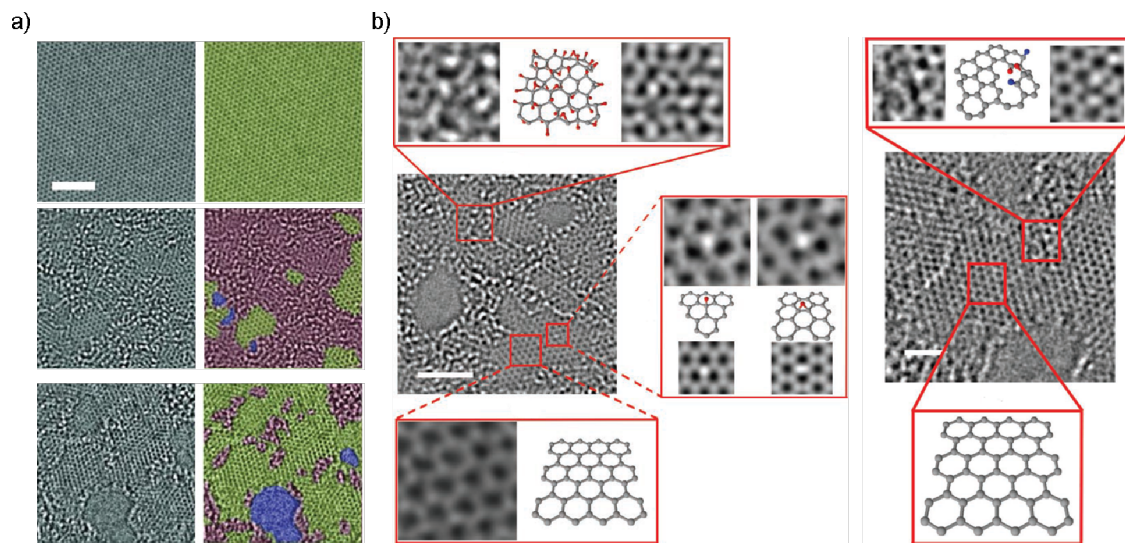


Figure II.2.5. a) TEM images of Graphene, GO and rGO. The scale bar is 2nm. In the right column are the same images as in the left one, but with color highlighted domains: yellow-green are graphitic domains, blue are the holes and red-purple are oxidized domains. b) Aberration-corrected TEM image of a single sheet of suspended GO and rGO. Expansions are highlighting the surface structure. Adapted from [18]

X-ray photoelectron spectroscopy (XPS) data showed that there are four main oxygen-containing functionalities of carbon present in a variety of GO samples. The main assigned groups are hydroxyl ($-\text{OH}$) and epoxy, with a contribution from carbonyl ($\text{C} = \text{O}$)

and carboxyl (COOH) groups. The C 1s spectrum for GO samples (Figure II.2.6) consists of three similar components. The peak at 284.5 eV is assigned to the carbon atoms of graphitic domains. Even if the carbon atom is not perfectly graphitic, it will generate a signal in this area as long as it is not chemically bound to oxygen atoms. The spectrum is dominated by the component centered at 286.5 eV. This peak is attributed to the carbon atoms of epoxides and tertiary alcohols. The integral spectrum contains a shoulder at 289.2 eV that is usually ascribed to carboxylic acid groups. The signal from ketones falls into the (286.5–287.5 eV) interval together with epoxides and alcohols, although some studies placed it into the 288.5–289.2 eV interval together with the signal from carboxyl groups. The actual signal from the ketone carbon atoms is probably positioned somewhere in between. The databases for the known carboxyl and ester group carbon O–C = O provide values from 288.6 eV through 289.2 eV [19, 20]. Thus ketones bridge alcohols and epoxides are on the right hand side of the spectrum, with carboxyls on the left. The line related to the later component is most likely the sum of the two overlapping peaks of carboxyls and ketones. Although the C1s XPS spectrum of the reduced GO (Figure II.2.6b) exhibits these same oxygen functionalities, their peak intensities are much lower than those in GO. In addition, there is an additional component at 285.9 eV corresponding to carbon bound to nitrogen. These observations indicate both considerable de-oxygenations by the reduction process as well as nitrogen incorporation.

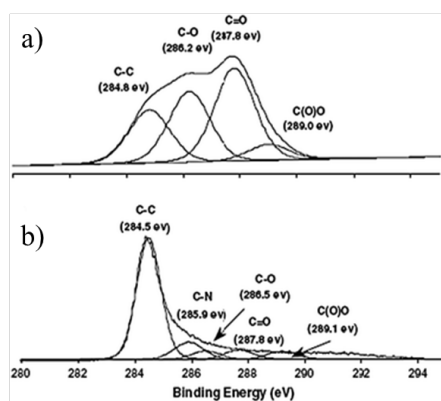


Figure II.2.6. The C1s XPS spectra of: (a) GO, (b) reduced GO. Adapted from [23]

There are several possible methods for deconvolution of the integral C 1s spectra. Some of these methods try to separate the contribution of the C–OH carbons from the contribution of the C–O–C atoms, and the contribution of the C = O groups from that of the O–C = O groups [21, 22]. Since the number of possible ways for the deconvolution of the

integral spectra is virtually unlimited, the conclusions should be carefully made by considering the computed data from DFT calculations. It is, however, clear that the C 1s XPS spectrum describes well the overall oxidation level of GO and rGO.

The technique that can also provide important information about the state of lattice disorder, the size of sp^2 carbon regions, structure-specific vibrational phonon modes and electronic doping in the graphene-based materials is the Raman spectroscopy. The Raman spectra of graphite-based materials such as GO have several distinct features. However, the most typical bands are D ($\sim 1385\text{ cm}^{-1}$), G ($\sim 1580\text{ cm}^{-1}$) and G' or 2D ($\sim 2700\text{ cm}^{-1}$) [24, 25]. The D band originates from a second-order effect involving a phonon and it is often attributed to disorder in the carbon material. The G band comes from the first-order Raman scattering of doubly degenerate E_{2g} mode related to in-plane optical vibration in sp^2 carbon. The G' band (sometimes referred to as 2D) is the result of the two-phonon processes that include phonons with opposite momenta and it depends strongly (inversely) on the number of graphene layers. The G band is associated with sp^2 graphitic structure and the D band is related to the defects in a structure. Their intensity ratio (I_D/I_G) is a good quantity of the relative defect content in the sp^2 carbon lattice. These bands in GO (Figure II.2.7) are different to a certain extent from those in graphite and graphene: the D band is broad and intense in GO, and the G band is fairly suppressed, broadened substantially [26] and sometimes slightly shifted to higher frequencies [27, 28]. This shift should probably be attributed to doping effects [29, 30]. Another explanation (based on theoretical calculations [27]) is that the alternating pattern of single and double bonded carbons in GO would result in the blue shift in the Raman G band that corresponds to these double bonds. The D band of graphene/graphite is often indistinguishable from the background and the I_D/I_G ratio in the spectra of GO is much larger.

The reduction of GO, has steadily shown the red-shifts of the G band [31, 32], which complements with previously doping-attributed blue shifts acquired with oxidation. However, changes in the I_D/I_G ratio vary depending on the reduction procedures. Some studies report no changes in the I_D/I_G ratio with reduction [33, 34]. In that case, the removal of the oxygen-containing groups did occur but the defects that replaced those groups were not healed. Other reports indicate a decrease of the I_D/I_G ratio, suggesting reduction-mediated removal of the defects [35-37]. There are also cases where an increase in D and G intensity ratio was observed [38-40], meaning that the reduction created more disorder and consequently increased the D-band intensity due to arbitrary nucleation of small sp^2 domains.

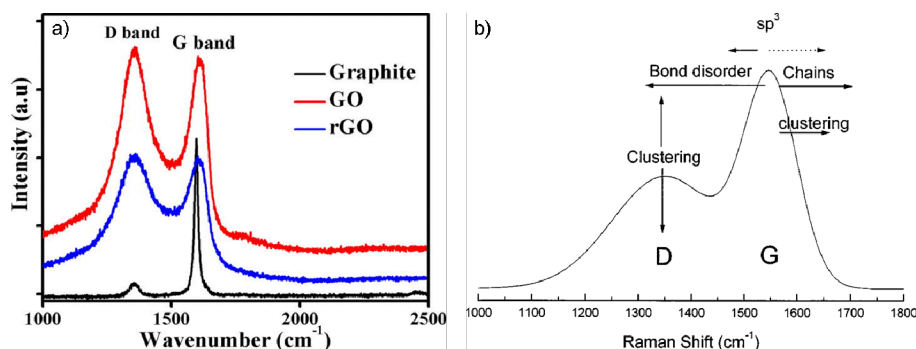


Figure II.2.7. a) Raman spectra of graphite, graphene oxide and reduced graphene oxide, and b) schematic diagram of influences on the Raman spectra. A dotted arrow marks the indirect influence of the sp^3 content on increasing G position. Adapted from [41, 24]

The UV-vis spectra of GO showed that strong absorption in the ultraviolet (UV) while its long tail extended into the visible part of the EM spectrum. The p-orbitals of carbon can be combined either in-phase (Figure II.2.8a) or out of phase (Figure II.2.8b), producing bonding and antibonding combinations. This gives rise to π and π^* orbitals, where the π orbital is lower in energy than the π^* , allowing a photon induced transitions between π and π^* , which is common for the aromatic C = C bonds. This electronic transition dominates the absorption of GO and usually occurs at ~ 230 nm [42–46]. A typical absorption spectrum of the GO prepared by the modified Hummers method [3] also exhibits a shoulder at ~ 300 nm (Figure II.2.89) that is attributed to the $n \rightarrow \pi^*$ transition in the C = O bonds containing functional groups [42–46]. This transition involves transfer of an electron from a lone-pair non-bonding n orbital to the antibonding π^* orbital via photon absorption. Non-bonding orbital is positioned between π and π^* (Figure II.2.8c) and it can be seen that the $n \rightarrow \pi^*$ transition is of lower energy and somewhat red-shifted from the $\pi \rightarrow \pi^*$ absorption feature. The ratio in peak intensities between the two features can be explained by a lower molar absorptivity for the $n \rightarrow \pi^*$ as opposed to $\pi \rightarrow \pi^*$ transition [47].

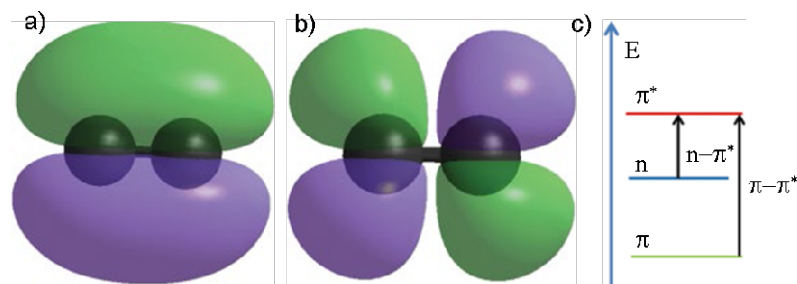


Figure II.2.8. a) The π orbitals of a C = C bond, b) the π^* orbitals of a C = C bond and c) energy diagram of π , π^* and n orbitals and its transitions. Adapted from [48]

Absorption spectra could be used to monitor changes in GO composition induced by reduction (Figure II.2.9). For example, upon chemical reduction, the shoulder at ~ 300 nm corresponding to the $n \rightarrow \pi^*$ transition in C = O disappears. This is followed by spectrum broadening and increased absorption in the visible part of the spectrum. The observed spectral changes are the consequence of two competing processes that occur during the reduction: the oxygen removal (which leads to the suppression of the 300 nm absorption feature) and restoration of the sp^2 carbon network (which results in the absorption broadening throughout the visible part of the spectrum as well as in an increase in the intensity of the $\pi \rightarrow \pi^*$ absorption peak). This is also observed in the reduction treatments of GO with either KOH [49] or hydrazine [50, 51].

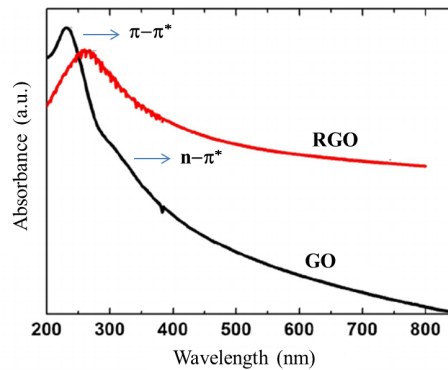


Figure II.2.9. The absorption spectra for graphene oxide (GO) and reduced graphene oxide (RGO). The peak at 220 nm corresponds to $\pi\text{-}\pi^*$ transition and the shoulder at 310 nm to the $n\text{-}\pi^*$ transition. Adapted from [48]

GO exhibits photoluminescence across its optical bandgap, because of the functionalization-induced opening of the energy gap. There are two distinct types of emission that are observed from aqueous suspensions of GO. Photoluminescence in the blue region of EM spectrum (350 – 450 nm) was detected from few-layer GO [50] and it is assigned to electron–hole recombination in sp^2 graphitic domains imprinted by the oxidation-induced sp^3 structure in GO.

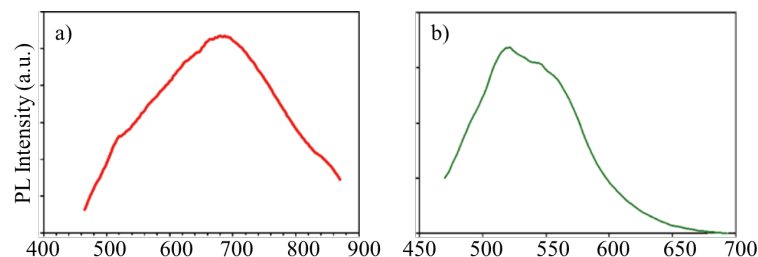


Figure II.2.10. Photoluminescence spectrum of GO produced from graphite a) via modified Hummers method and b) controlled oxidation from rGO. The excitation is 440 nm. Adapted from [48]

Second type of the observed emission is green to infrared (500 – 800 nm) emission from chemically oxidized GO [49, 52, 53]. This type of emission (Figure II.2.10) arises from localized electrons in the sp^2 carbon regions encircled by repulsive sp^3 carbon hard wall barriers, or from bond alteration induced inter-valley scattering effects [53]. Eda et al. [50] proposed that GO emission is the result of the relaxation processes in multi-layer graphene flakes. Some authors suggest the $\pi \rightarrow \pi^*$ bandgap photoluminescence mechanism: GO is split into smaller and larger clusters of graphitic sp^2 carbon separated by oxidized sp^3 regions. These clusters experience strong localization by surrounding sp^3 -hybridized atoms acting as potential barrier walls. In order to understand the origin of emission mechanism, a number of factors need to be considered. The scheme of such processes is depicted in Figure II.2.11a.

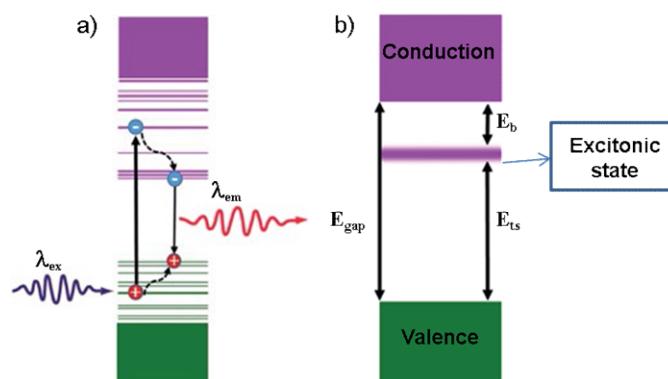


Figure II.2.11. a) Arrangement of the bandgap photoluminescence process and b) Simplistic scheme of electronic transitions considering excitonic effects, where E_{gap} is one-electron bandgap energy, E_b is the binding energy of the exciton and E_{ts} is the first allowed optical transition energy. Adapted from [48]

When the incoming photon is absorbed, an electron is transferred over the bandgap to the higher orbital, leaving a positively charged hole behind. The creation of an electron–hole pair (exciton) is then followed by non-radiative decay of the electron to the lowest unoccupied molecular orbital (LUMO) and of the hole to the highest occupied molecular orbital (HOMO). This process continues through radiative recombination of the exciton. As a result, a photon is emitted with the energy lower than that of the excitation light. The efficiency of this process is described by the fluorescence quantum yield expressed as a ratio of absorbed to emitted photons. Quantum yield reported for GO is quite low (0.02–0.5%) [46, 49], due to the electron-hole recombination through a number of non-radiative pathways, including charge defects/traps or phonon-assisted relaxations. Fluorescence lifetimes reported for GO are of the order of magnitude from picoseconds to nanoseconds [42, 43, 50, 54]. Chen et al. [46] reported that the blue and the red emission features can exhibit different fluorescence lifetimes, in the picosecond range for red emission and -in the nanosecond range for the blue

emission. Electrons act as massless particles in graphene; the confinement induces energy quantization and consequently the existence of the bandgap [55] of the order of:

$$E_{\text{gap}} \approx (v_F h / 2d) \approx (2 \text{ eV nm} / d) \quad (\text{Eq. II.2.1})$$

Here v_F is the Fermi velocity of the electron and d is the diameter of the confined sp^2 region. The photoluminescence process occurs in the small sp^2 carbon clusters that have a larger bandgap on the order of 3.2 eV and enclose roughly about a dozen aromatic rings according to the density functional theory (DFT) calculations [50]. These clusters were localized by surrounding sp^3 oxidized carbon and, possibly, by a few larger sp^2 clusters with smaller bandgaps. The bandgap values calculated in theoretical predictions of photoluminescence in functionalized carbon materials by tight-binding molecular dynamics simulation varied from 0.3 to 2.7 eV depending on the degree of functionalization. The DFT calculations [56] estimated $\pi \rightarrow \pi^*$ gaps to be of the order of 0.3 – 4 eV, although the electronic contributions from surrounding sp^3 sites were not included.

Experimental observations by high-resolution transmission electron microscopy (HRTEM), showed that the size of the graphitic sp^2 islands in GO sheets is around 1–2 nm [18]. This would correspond to a smaller bandgap and thus a red-shifted emission in the green, red (Figure II.2.11) or even near-infrared (NIR) parts of the spectra. By taking into account the binding energy of the exciton, the emission energy was found to be less than the bandgap by an amount equal to the exciton binding energy (Figure II.2.11):

$$E_{\text{ts}} = E^{\text{GW}} - E_{\text{b}} \quad (\text{Eq. II.2.2})$$

Here E^{GW} is the single-electron bandgap calculated by the GW approach, E_{b} is the exciton binding energy and E_{ts} is the optical transition energy [57]. Further calculations of the emission energy (E_{ts}) showed an inverse dependence on the nanodisk diameter, resulting in a nearly linear $1/D$ trend. The reported correlation of GO photoluminescence emission energy with the size of the sp^2 graphitic circular islands emphasize the significance of the excitonic effects in GO.

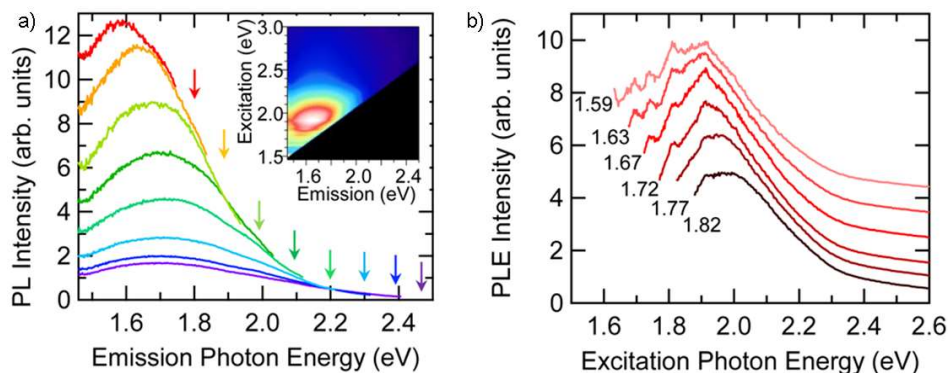


Figure II.2.12. a) PL spectra of GO in aqueous solution obtained with various excitation energies from 1.8 to 2.5 eV. The arrows indicate the excitation energy. Inset shows a PLE intensity map of GO. b) PLE spectra of GO with various monitored emission energies from 1.6 to 1.8 eV. The numbers indicate the monitored emission energy. Adapted from [57]

Figure II.2.12a shows PL spectra of GO in aqueous solution with excitation at various photon energies where the arrows indicate the excitation energies. The PL spectrum of GO shows a broad emission peak in NIR region (~ 1.7 eV), and the gradual blue shift and broadening of emission features are observed with increasing the excitation energy. Figure 1b shows PLE spectra of GO with various monitored emission energies from ~ 1.6 to ~ 1.8 eV, where the numbers indicate the monitored photon energies. The PLE spectra show a broad resonance peak below ~ 1.95 eV depending on the monitored energy, which is also observed in the PLE map as shown in the inset of Figure II.2.12a. The observed PL spectra indicate the broadening originates from the emission from inhomogeneous structure of GO because of the energy redistributions within an ensemble of emitting states [58]. This is reflected in the shift in the emission spectra upon the change in excitation wavelength (Figure II.2.12), which is also observed in a number of studies [42, 54, 57]. When excitation is shifted to the red, the larger sp^2 regions would exhibit red-shifted emission. Since the photoluminescence originates from the sp^2 domains of different sizes, the distribution of the emission energies will be wide. The relaxation process also involves multiple energy transfer steps and therefore results in longer lifetimes for less energetic emission [57].

The position of the photoluminescence peak is described by a combination of two contributing factors: the relative abundance of sp^2 graphitic regions of a particular size and the efficiency of energy transfer to the regions of the larger size. The first is governed by the degree of oxidation in GO and, possibly, the type of functionalization process. The second factor influencing the energy transfer is given in part by the proximity of graphitic regions in the sp^3 matrix, which, again, relies on the state of GO functionalization and the distribution of

sp^2 clusters. The short photoluminescence lifetimes suggest that emission proceeds before charge relaxation to the band edge, therefore bypassing band-edge transitions [49]. Due to the wide spectrum of vibrational states in GO, there is a variety of possible transitions yielding a broad emission spectrum. This work also indicates a dependence of emission wavelength on excitation. Still, the Stokes shift between those two appeared to be constant for a particular electronic transition and, therefore, a particular functional group. Such strong correlation of photoluminescence in GO with oxygen-containing functional groups together with the evidence provided solid background for the functional-group-related emission model in GO.

In summary, photoluminescence from GO was detected in the blue and red part of the spectrum, while certain studies also report green ultraviolet and near-infrared emission. The origin of the photoluminescence has been proposed by several models, including the emissions from confined domains of sp^2 graphitic carbon, the emissions from localized electronic environments surrounding oxygen-containing functional groups, or even emissions from oxidation-produced graphitic debris.

II.2.2. Partial reduction of graphene oxide

In this chapter we will focus on the influence of the reduction process on the optical properties of graphene oxide. The partial reduction yields a structure with different physico-chemical properties with respect to initial GO (graphene oxide) and reduced GO. The mechanism of the partial reduction of the graphene oxides will be discussed through the results obtained from the optical absorption, Raman scattering and photoluminescence spectroscopies.

The optical properties of GO depend on the type of the reduction process. Thermal reduction leads to less abrupt changes in GO photoluminescence than chemical reduction [59]. Thermal reduction produces larger red shift in photoluminescence [32], possibly due to a weaker excitonic confinement (larger sp^2 clusters). Gradual reduction under the Xenon lamp irradiation [60] resulted with the complex photo luminescent behavior of GO: an initial emission feature in the red part of the spectrum decreased significantly, while there was a simultaneous increase of the sharp emission peak at ~ 450 nm. This suggests a dual nature of GO photoluminescence. The major red emission feature of GO is present due to the optical transitions in disorder-induced localized states (Figure II.2.13a) that lie deep within the $\pi \rightarrow \pi^*$ gap. The feature observed in the blue range was attributed to the emission from confined sp^2 regions appearing in the initial stage of GO reduction (Figure II.2.13b) as advocated previously [section II.2.1].

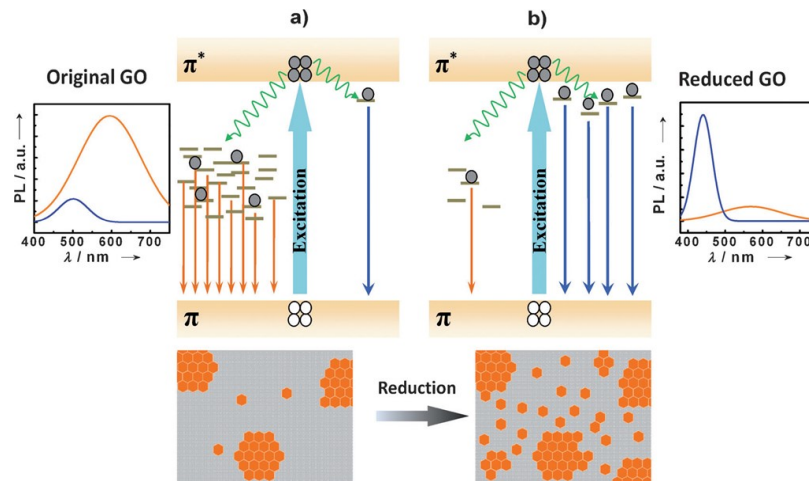


Figure II.2.13. Representations of the dual nature of photoluminescence in reduced GO. a) The main emission in GO from disorder-induced localized states. b) The prime emission in thermally reduced GO from confined cluster states. Adapted from [60]

A mild chemical reduction causes a red shift in GO photoluminescence spectra [63]. The reported study proposes that under these conditions the growth of sp^2 regions in GO is constrained to a certain extent. It seems that the growth of the domain continues until it reaches the size of ~ 2 nm, after which the nucleation of new sp^2 domains takes place. With the prolonged reduction, as proposed previously [50], photoluminescence is quenched because of exciton recombination at the defect sites allowed by reduction-facilitated percolation of sp^2 regions. This model of GO reduction is also supported by observed changes in Raman spectra of the partially reduced GO. A non-monotonic trend in I_D/I_G ratio was observed with gradual chemical reduction of GO (Figure II.2.14): at first I_D/I_G ratio decreases and then start to increase [61]. An increase in I_D/I_G ratio is attributed to the growth of sp^2 regions at short reduction times. A subsequent increase I_D/I_G ratio is a result of the formation of smaller sp^2 regions inside sp^3 clusters, which increased the disorder in the lattice. Different reduction procedures might give GO with different optical properties. However, they provide information about possible lattice morphologies that arise during the reduction process.

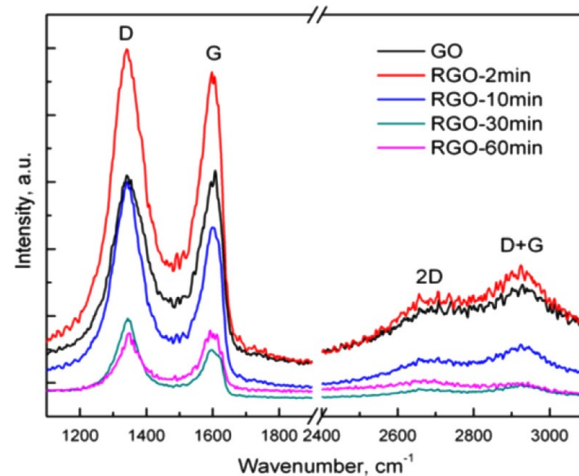


Figure II.2.14. Raman spectra of as-grown (black), hydrazine reduced GO (red) and thermally reduced. Adapted from [61]

Although there are contradicting observations in the literature, it is widely accepted that the intensity of the GO photoluminescence decrease upon prolonged reduction. In addition to decrease in the emission intensity, a number of works also report a blue shift [44, 62] that contradicts the theoretical prediction of GO band-gap shrinkage at the end of reduction process [56]. Such unexpected behavior could be explained by reduction-induced formation of small sp^2 islands with larger optical bandgaps. It had been suggested that reduction at first does not induce the increase of sp^2 cluster size in GO, but rather stimulates

nucleation of smaller-sized sp^2 domains [60]. According to that, newly created sp^2 domains with larger bandgaps would indeed shift the emission towards the blue range. This hypothesis is also supported by observation of slightly non-monotonic behavior of emission intensity upon chemical (Figure II.2.15a) or thermal reduction of GO [32, 50]. These experiments show that the photoluminescence first increases and then decrease steady with at longer reduction times. This may point to the formation of new sp^2 regions responsible for the increase in photoluminescence at the initial stages of the process. The new arrangement of sp^2 domains in the end resulted in quantum yield being much higher than that of the GO. Further reduction could cause photoluminescence quenching due to percolation between sp^2 regions allowing for increased exciton migration eventually leading those to non-radiative recombination sites [50].

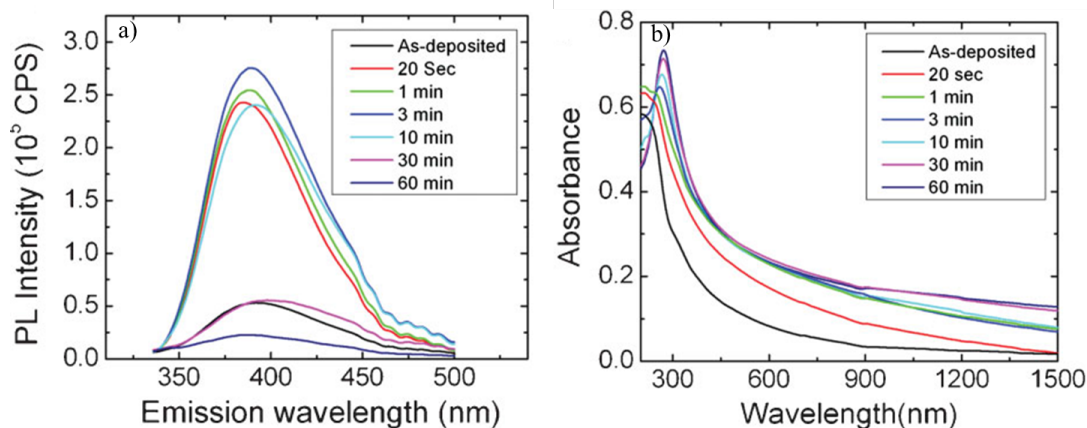


Figure II.2.15. a) Photoluminescence emission (for $\lambda_{exc} = 325$ nm) and b) UV-vis spectra of progressively reduced GO. The exposure time to hydrazine is given in the inset. Adapted from [50]

As a result of the reduction treatment of GO with hydrazine [50], the absorption feature 310 nm disappears and the absorption is broadening into the visible range. This is associated with the removal of oxygen-containing groups (Figure II.2.15b). The broad absorption that extends up to 1500 nm indicates the absence of a well-defined band-edge in the UV-vis energy range. A shoulder around 310 nm ($n-\pi^*$ transitions of C=O) disappeared almost immediately after exposure to hydrazine treatment, most likely due to the decrease in the concentration of carboxyl groups. The absorbance is found to increase with hydrazine exposure time, consistent with the evolution of oxygen and with a simultaneous increase in the sp^2 fraction. A reverse process involving controlled oxidation of reduced graphene oxide (rGO) with ozone into GO produced completely opposite changes: a blue shift of absorption spectra and

significant reduction of absorption background in the visible range with oxidation time (Figure II.2.16a). That is the indication of a decrease in the sp^2 graphitic structure, which absorbs strongly in the visible part of the spectrum.

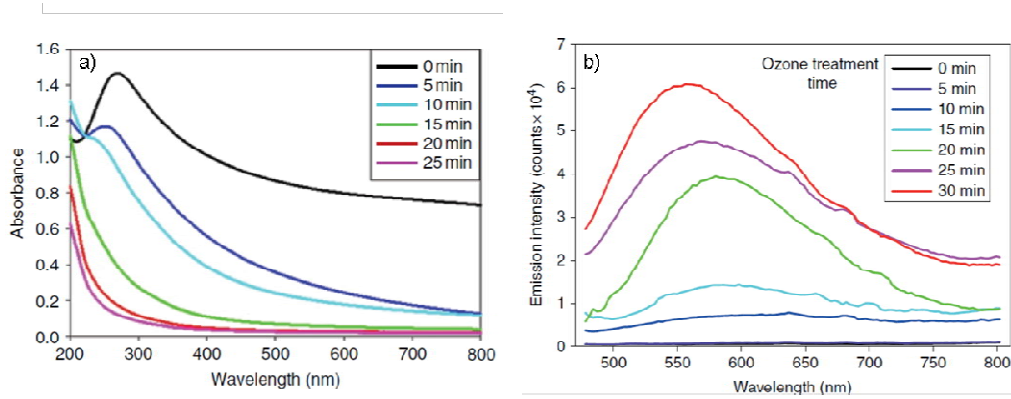


Figure II.2.16. a) Absorbance spectra of rGO oxidized via controlled ozone treatment for 0 - 25 minutes and b) photoluminescence spectra of ozone treated rGO for 440 nm excitation wavelength (0 – 30 minutes). Adapted from [48]

It is also interesting to note, that plasma treatments of graphene and acid assisted oxidation of graphite have all resulted in bandgap opening [55, 62, 63]. The band-gap energies varied from 1.7 to 2.4 eV, while the stronger oxidation caused larger bandgap. Another procedure allowing controllable oxidation includes timed ozone treatment of non-emissive reduced graphene oxide (rGO) obtained from GO by hydrazine reduction. Upon oxidation, initially non-emissive rGO has exhibited bright photoluminescence in the visible, with its intensity dependent on the time of ozone treatment (Figure II.2.16b). In that process, a comparatively small shift in the emission energies was observed, possibly because rGO has already inherited lattice defects that were not removed upon reduction. Also, one study suggests that confined sp^2 domains could still have been present in rGO from the previous oxidation [64]. These defects would have predetermined the initial size and distribution of oxidation-induced sp^2 islands and thus the emission range. The other possibility involves a different photoluminescence mechanism, with emission arising from functional groups, which dictates somewhat weaker dependence of emission energy on the degree of oxidation. Such a mechanism, proposed in multiple works studying photoluminescence of GO [52, 55, 59], involves emission from localized states at the functional groups. The important role of functional groups was also supported by calculation of molecular orbitals in GO [42]. The results demonstrate that photoluminescence is governed by a HOMO–LUMO transitions that occur predominantly at carbon atoms situated in vicinity of oxygen-containing functional groups. According to this, all three kinds of oxygen functionalities, C–O, C = O and O = C–

OH, were related to the emission. A similar conclusion was derived from studying the possible contributions of the electronic transitions in functional groups to GO photoluminescence [49]. GO was treated with KOH in order to remove hydroxyl groups and convert epoxy groups to hydroxyl, or with HNO₃ in order to further oxidize GO and produce additional carboxyl groups. The characteristic features in the photoluminescence spectra of in this ways treated GO were attributed to particular electronic transitions: $\pi^* \rightarrow \pi$ transition of the C = C bond, $\pi^* \rightarrow n$ transition of the C = O groups and $\sigma^* \rightarrow n$ transition of C–OH groups. Based on that analysis, photoluminescence transitions in GO were assigned primarily to the transitions of oxygen-containing functional groups.

An attempt was made to explain the emission of GO through spectral hole burning [55]. It was expected that, upon intense excitation at a particular wavelength a subset of sp² carbon-cluster-based emitters of a certain size should be bleached, leaving a spectral hole in the piece of plasma-oxidized graphene. However, experimentally, this is not observed. Instead, the emission was quenched across all wavelengths in that region. Because of that, photoluminescence was traced to localized electronic states at oxidation sites and the emission spectral width was attributed to homogeneous broadening of the energy states at oxygen-containing emissive species. Such localized electronic states were modeled by Galande et al. [52] showing a region of negative electrostatic potential around oxygen-containing addends in GO. The former authors observed, for the first time, a strong pH dependence of GO photoluminescence. Upon pH change from acidic to basic, a broad GO emission in the red region was quenched and a sharp blue-shifted photoluminescence peak emerged.

Various treatments, particularly controlled reduction and oxidation of GO, resulted with two major theories of GO photoluminescence concerning confined sp² cluster-related and oxygen-containing functional groups emissions. However, new scientific studies revealed that both sp² clusters and oxygen-containing functional groups contribute to the observed effects. Chien et al. [60] reported the presence of two emission peaks in GO: a blue feature attributed to quantum confined graphitic domains and the red emission arising from functional-group-induced disorder states. It is also observed that the emission peaks have different luminescence origins concerning the fact that they exhibit fluorescence lifetimes that differ by nearly three orders of magnitude [46]. Time-resolved photoluminescence measurements of GO and GO reduced via Xe-lamp irradiation has also shown notably different lifetimes [58]. The initial emission of GO in the red range exhibited significantly longer fluorescence lifetimes the in comparison to the blue rGO emission. However, when

measured right after the excitation pulse, the emissions of both rGO and GO were identical and detected in the blue region. The initial similarity of the life times suggests that there is a red shift of the emission with time, due to non-radiative spectral relaxation in GO. This process was further studied by the disordered gap model (Figure II.2.17), where at certain spatial regions in GO the gap energies are in the blue and in some regions they are in the red range. Upon excitation, the exciton in GO could migrate from larger (blue) gap regions to smaller (red) gap regions, which would induce radiative recombination. In rGO, due to short carrier lifetimes, spectral relaxation and shifting would not have enough time to occur. As a result, long-lived excitons in GO that undergo spectral migration to the red range do not survive in rGO, which yields the short-lived emission in the blue.

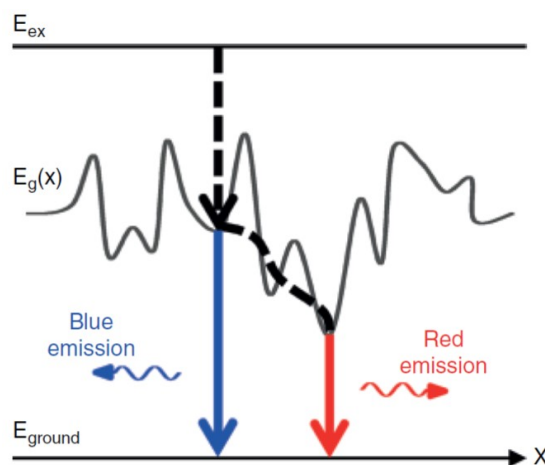


Figure II.2.17. Proposed relaxation of excited carriers within the context of a disordered band model of GO. Adapted from [34]

Studies of the oxidation and reduction of GO not only elucidate possible mechanisms of fluorescence emission in GO but also provide important routes for modification of its optical properties. A considerable increase in fluorescence quantum yield of GO up to 13% was observed upon functionalization of the epoxy and carboxyl groups in GO by alkylamines [65]. This is probably the result of the passivation of epoxy and carboxyl groups that act as quenching centers. At the same time the sp^2 domain structure responsible for the emission in GO was unaffected by the treatment. Highly enhanced photoluminescence was reported for Mn^{2+} -bonded rGO [66], where the increase in emission was assigned to fluorescence resonance energy transfer from Mn ions to emissive sp^2 clusters in graphene. Due to the energy level structure in Mn, resonance energy transfer could significantly enhance the emission of rGO, strongly increasing the photoluminescence intensity at ~ 550 nm. Such

photoluminescence enhancements suggest that chemical functionalization could serve as an efficient route to improve the fluorescence quantum yield of GO.

II.2.3. Fluorescent nanostructures based on graphene oxide and reduced graphene oxide

Graphene oxide (GO) has exceptional optical properties that are necessary for the applications in fluorescence bioimaging: resistance to photobleaching, tunable emission wavelength, high Raman scattering intensity, large absorption cross section in the NIR region and low toxicity [67, 68]. Conjugates built on the graphene-based scaffolds have excellent target specificity and high capacity for drug loading with the rapid pharmacokinetics. Due to the ability to quench the photoluminescence of biological molecules and viruses, GO was applied as an optical biosensor [69]. The recent reviews [70, 71] emphasize the significance of the graphene based materials (mainly GO and rGO) as the new advanced drug delivery systems. There is a large market of applications of the optical properties of GO and rGO in optoelectronics, sensing and biological imaging. Reduced graphene oxide is proved to be a better sensing platform and loading dock for adsorption of DNA than graphene oxide [69]. Recent studies on GO photoluminescence proposed a number of its potential uses in photonic devices, including electroluminescent cells and photodetectors [27]. The sensitivity of GO emission to the environment has been used in multiple sensing applications. The mentioned pH dependence of GO fluorescence emission also positions it as a nanoscale sensor for extracellular biological pH [52, 72]. Potential environmental applications of GO include metal ion sensing by N-doped GO, due to the selective sensitivity of its photoluminescence to normal and transition metal ions [73]. In addition to sensing, GO and GO quantum dots have been successfully used as vehicles for drug/gene delivery and biological imaging [74-78]. GO is water-soluble and provides a large platform for the attachment of multiple drug molecules on both sides of the graphene sheets [76]. It has been reported as a high-capacity carrier for anticancer drugs, genes and targeting agents [76, 79]. In addition to that, the intrinsic photoluminescence of GO [77, 79] or GO quantum dots [75] could be used for the imaging of drug/gene delivery pathways without the need for additional fluorophores. Due to the transparency of biological tissue in the near-infrared, and the fact that it emits in that spectral region [79], GO is highly attractive for both in vitro and in vivo fluorescence imaging. As a result, GO poses a significant advantage to existing delivery/imaging modalities due to its multi-functionality and large transport capacity. New functionalities arise when the reduction of graphene oxide takes place. Studies that exploit changes of the surface chemistry of graphene oxide after the reduction report favorable physico-chemical assets for various functionalities which can be employed in emerging biological applications [80, 81].

Fabrication of the fluorescent nanostructures based on GO and rGO for bio applications is presented below.

GO is a 2d structure in which every atom is exposed to the surface. Because the surface area of GO is very large, one can densely load GO with cargo, e.g. drugs, cell-surface-directing fragments, nucleic acids and proteins. GO is water soluble, but it can aggregate in the presence of salts and cell medium. Therefore, this material is often chemically modified to improve its biocompatibility, which includes either non-covalent (electrostatic or π - π interactions) or covalent modification [82]. For example, mixing GO with poly(ethyleneimine) (PEI) of different sizes (1.2–10 kDa) leads to formation of hybrid GO–PEI compound, which, in contrast to GO, is retained in the physiological solution and the serum-containing medium. Moreover, such hybrids have lower toxicity than free PEI [83]. In this case, the electrostatic interaction at neutral pH between positively charged PEI and negatively charged GO is the driving force for the GO–PEI formation. Furthermore, π - π interactions can be used to modify GO and rGO. For example, planar aromatic molecules, such as porphyrins, pyrenes, perylenes and coronenes, have been used as anchors for attaching different functionalities to GO and rGO [84]. Since GO contains a variety of reactive functional groups, one often applies covalent chemistry to modify the GO surface. The most popular reactions include the formation of amide bonds, which typically occurs between a GO-bound –COOH group and a modifier-bound –NH₂ group [85]. For example, the attachment of polymers like PEG, poly-l-lysine and polyacrylamide (PAA) to GO has been conducted by using such reactions. A non-covalent interaction of GO with π conjugated molecules is possible because of the high share of the sp² carbon atoms (Figure II.2.16). Water molecules always interact by hydrogen bonding (polar interaction) and therefore GO is dispersible in water. In one example, the polymer of methylcellulose was used to make hydrogen-bonded composites. The polymer isolates individual sheets and it was found that fluorescence properties could be adjusted over a wide range of pH [86]. In accordance with the noncovalent functionalization concept, fluorescent dye-labeled single-strand DNA (ssDNA) can interact with GO, which leads to the quenching of the fluorescence. It could be observed that the fluorescence is restored upon addition of a complementary target, because of the stronger target–ssDNA interaction compared to ssDNA–GO interaction (Figure II.2.18) [87].

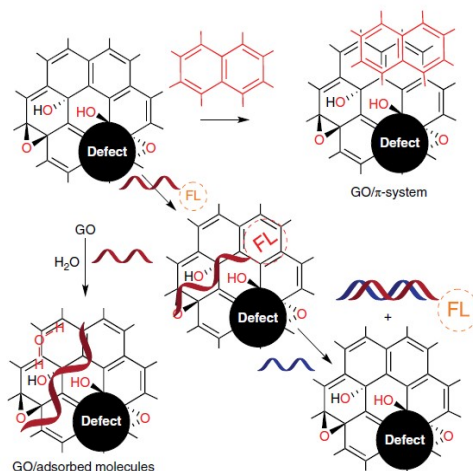


Figure II.2.18. Non-covalent methods to functionalized GO with π interactions or polar interactions. Adapted from [87]

A stable dispersion of rGO in water was prepared by using poly(diallyldimethylammonium chloride) (PDDA) [88]. First, GO was stabilized by non-covalent interaction with a cationically charged polymer PDDA and then stable dispersions of rGO/PDDA were prepared by chemical reduction of the composite with sodium borohydride. The polymer modified GO and rGO, gave also the stable dispersions of single layers. Without the stabilizing polymer, the rGO tends to aggregate and form precipitates. It is proposed that GO and PDDA interact by polar interactions of the oxo-functional groups of GO with the cationic groups of PDDA. The interaction of rGO and PDDA is due to van der Waals interactions and in part via polar groups that are located at the edges of defects. As for the non-covalent π - π interaction of pyrene derivatives with GO, it is limited due to solubility incompatibilities. However, rGO offers a vast π system and functional groups at defect sites still provide polar groups (Figure II.2.19) [89].

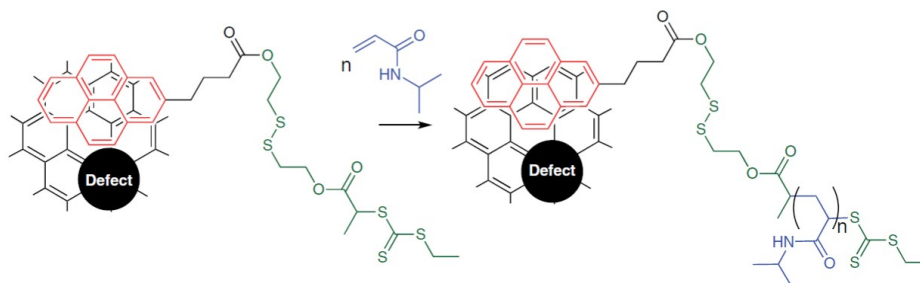


Figure II.2.19. The illustration of the ability of non-covalent polar interaction of pyrene (marked as green) with the π system of rGO that enables attachment of the reversible addition-fragmentation chain-transfer agent (marked as blue) for composite formation. Adapted from [89]

In photothermal therapy (PTT) of cancer, bacteria and other cells that cause the disease, the cells are internalized with a compound that absorbs near-infrared (NIR) light. Then subsequent exposure to NIR light heats up the specified compound, inducing hyperthermia and thereby causing cell death. The light of the beam can be focused on a tumor location and its intensity (dose) can be easily controlled. Single-layered GO is suitable for PTT, since, in addition to its excellent water solubility, membrane permeability and stability, this material absorbs in the NIR range [90–92]. By optimizing the size of GO, the NIR absorptivity can be improved. Small GO (nano GO < 300 nm) absorb NIR light efficiently. The extinctions at 808 and 1200 nm have been found to be from five- to eight-fold higher in nano GOs (NGOs) [93]. The accumulation of GO in tumors can be achieved by decoration of GO with ligands that bind to cancer-specific receptors. Wu and co-workers have explored the applicability of conventional GO obtained by the Hummers method in combination with PTT for the treatment of bacterial infection in wounds [94]. This is a rare example demonstrating the biological activity of conventional, chemically unmodified GO in vivo. The healing of the wounds treated with both GO and subsequent laser irradiation was faster in comparison to the control wounds. This indicates that GO in combination with PTT can potentially be used as an efficient and cheap alternative to antibiotics. PTT in combination with GO or other NIR-absorbing nanomaterials has the potential to improve the side effects that occur during conventional chemotherapy. Moreover, when applied together, PTT and chemotherapy have been shown to exhibit synergistic effects [95]. For example, Guo and coworkers have prepared a hybrid material NGO–PEG–DOX containing NGO covalently modified with polyethylene glycol (PEG) residues and doxorubicin (DOX) [96]. The PEG fragment stabilizes NGO in the serum-containing media, enabling the application of this material in vivo. DOX is an anthracycline antitumor drug, which exhibits its activity due to binding of genomic DNA via intercalation. This fragment binds the NGO–PEG via non-covalent π – π interactions. The authors have reported a strong synergistic antitumor effect of DOX and PTT: the tumors were completely destroyed 30 days after the beginning of treatment. Interestingly, DOX alone exhibited substantially stronger side effects than the nano-sized construct NGO–PEG–DOX. These data demonstrate that PTT combined with chemotherapy can be a feasible approach for the improvement of current methods of cancer treatment.

The organic drugs comprising of extended π systems are common and such compounds can act as intercalators of genomic DNA for antibiotics, inhibit specific kinases and act as antimetabolites in chemotherapy. Many such drugs are not well soluble in water, which can be improved by loading them onto well soluble GO-based materials. Moreover, the

uptake mechanism of GO–drug hybrids is often different from those of the free drugs. Resistance that is developed as a result of repeated treatments with the same drug is an important problem in the chemotherapy of cancer. The activity of hybrids is often higher and they can be utilized to overcome the resistance of cells to particular drugs. Despite being a potent anticancer drug, DOX has an extended aromatic structure and can interact with sp^2 -hybridized regions of GO due to π – π stacking interactions. This interaction is so strong that it is sufficient for the immobilization of DOX onto GO and no additional covalent attachment is usually required. Moreover, DOX is a fluorescent molecule that allows easy monitoring of its loading into cells by using either fluorescence microscopy or flow cytometry. In a recent study nano-GO with sheet size below 100 nm and thickness between 0.8 and 1.5 nm was used as a drug carrier [97]. By simple incubation of the components and removal of the excess drug by centrifugation, high cargo loading could be achieved, 0.468 g DOX per 1 g NGO. Interestingly, the interaction strength between the NGO and DOX was strongly affected by the pH of the solution. In particular, at neutral (pH 7.2) and basic (pH 9.0) conditions, less than 6.5% of the drug was released after standing for over 40 h in the correspondingly buffered phosphate saline (PBS) solutions. In contrast, at slightly acidic conditions (pH 5.0) ~15% of DOX was released within the same time. This effect has been attributed to the presence of hydrogen bonding between the functional groups on the NGO (–OH, –COOH) and those of DOX (–OH, –NH₂) in addition to the π – π stacking. The former bonds were expected to be destabilized under the acidic conditions. Since the microenvironment in tumors is often acidic, this property of NGO–DOX can be used for the selective release of DOX at the cancer-specific conditions, which should improve the therapeutic index of the nano-drug.

GO-based materials can potentially evolve as true alternatives to the usually used transfection reagents for creating new approaches for improving cell membrane infiltration of nucleic acids. Nucleic acids play a central role in the storage of genetic information, protein synthesis and regulation. Liu and coworkers have modified GO covalently with cationic PEI polymers of different sizes: 1.2 and 10 kDa [98]. They have found that both GO–PEI-1.2 kDa and GO–PEI-10 kDa induce the efficient transfection of a plasmid carrying enhanced green fluorescent protein (EGFP), which could be followed by monitoring the EGFP expression via fluorescence microscopy. Zhang et al. [99] have designed a hybrid consisting of GO that was covalently modified with PEI-25 kDa and contained siRNA (small interfering RNA) targeting an mRNA (messenger RNA) of the Bcl-2 gene. These data confirm the applicability of GO as a carrier for the transport of siRNAs into cells, which resulted in the significant inhibition of

tumor growth without any toxicity. Variety of different components can be loaded on the surface of GO to obtain multi-functional drugs. One such example [100] is the fabrication of PEGylated GO, which was carried out at the terminus of each PEG residue one folic acid (FA) fragment. Next, 1-pyrenemethylamine was adsorbed via strong non-covalent π - π interactions with flat regions of GO that provided an overall positive charge for the resulting construct. Finally, siRNA targeting a human telomerase reverse transcriptase (hTERT) gene was attached via electrostatic interactions. The authors have demonstrated that the obtained hybrid is not toxic to HeLa cells, but acts as a strong inhibitor of hTERT expression, as evidenced by monitoring the corresponding transcript and the protein.

The experiment for determination of the delivery efficiency would be the transport of a labeled ON, e.g. molecular beacons (MBs) or another hybridization-sensitive probe, which binds to its intracellular target and causes changes of the fluorescence of the probe. The latter reaction is stoichiometric and the fluorescence intensity is expected to correlate with the concentration of the target in the cell. One study reported on the transport of a DNA-based MB containing Dabcyl as a quencher and Cy5 as a reporter fluorophore [101]. This probe was designed to bind a surviving mRNA. The authors have observed that the nano-GO protected the MB from nucleases and substantially reduced the background signal of the MB in the absence of its target. Moreover, the nano-GO brought this MB into cells where it bound the surviving mRNA, as indicated by the increase of the fluorescence intensity in cells. A construct containing nano-GO and control MB has been found to generate a 2.4-fold lower fluorescence signal in cells.

Aptamers are short oligonucleotide (ON) or peptide molecules that have ability to bind targeted small molecules. These reagents can be applied as drugs and for imaging of biomolecules directly in cells. The authors have explored the opportunity for the delivery of an ATP-aptamer (ON) to cells using GO [102]. To be able to monitor the reagent delivery as well as its binding to intracellular ATP, the authors have labeled the aptamer with a fluorescent dye (Fl) to obtain ON-Fl. The GO-bound ON-Fl remained weakly fluorescent due to strong quenching of the Fl with the GO. However, upon binding of ATP, the aptamer was folded with the formation of the structure, which does not have the high affinity to GO. Therefore, the aptamer was released from the GO in the presence of ATP, which was reflected in the dequenching of the fluorescence of the ON-Fl. Thus, the fluorescence of ON-Fl/GO correlates with the concentration of ATP in solution. This type of behavior was observed both in cell-free assays and in cells, thereby confirming that GO is a suitable carrier of aptamers.

Graphene oxide has been used in variety of optical assays for the detection of biomolecules and xenobiotics and nucleic acids by using fluorescence-based approaches [103]. Oligonucleotides (ONs), such as short RNA and DNA molecules, interact strongly with GO. A detailed study was conducted on the binding of fluorescein-labeled oligonucleotides (Fl-ONs) of different length with GO [104]. The GO used in that work was obtained by a modified Hummers method and the binding was studied by means of fluorescence spectroscopy with monitoring the fluorescence quenching upon the addition of the GO to the Fl-ONs. The binding efficiency decreased with increasing ON length and the kinetics of this interaction has been found to be substantially faster for shorter strands than for the longer one. Since both the nucleobases of ONs and the flat regions of the GO are planar aromatics, they are able to get engaged in π - π interactions with each other analogously to those found between singlewalled nanotubes (SWNTs) and nucleic acids [105]. The GO-ON interaction is highly sensitive to the hybridization state of the nucleic acids. For example, single-stranded nucleic acids bind GO efficiently, whereas folded ones, including double-stranded nucleic acids, or aptamers [102] bound to their target molecules, do not bind GO. This property of GO has been used in a number of bioanalytical applications for detection of nucleic acids and, in combination with aptamers, for the detection of small molecules.

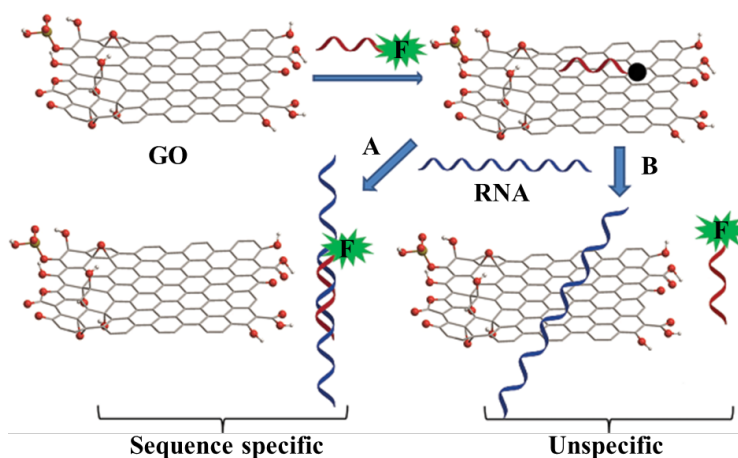


Figure II.2.20. Quenching and ON-binding properties of GO. Binding of the probe via pathway A leads to the sequence-specific fluorescence increase, while pathway B is manifested in the non-specific fluorescence increase. Adapted from [101, 104]

In early assays, a single-stranded ON containing a fluorophore was loaded onto nano-GO and GO, leading to fluorophore quenching (Figure II.2.20). Adding a complementary nucleic acid to the resulting mixture caused the formation of dsDNA, its release from the GO surface and, consequently, fluorophore dequenching. By utilizing this method, the reported study showed detection of DNA with an HIV1 sequence [106]. A recent study has provided

experimental evidence that the unspecific probe displacement from the GO followed by the hybridization of the probe with the target in solution is a major pathway of activation of the probe-GO sensors. Another important factor to account for in GO-based DNA detection assays is the level of oxidation of GO (C/O ratio). The C/O ratio strongly affects the fluorescence quenching ability of GO as well as its affinity toward single stranded ONs [73].

Functional materials based on GO and rGO have been attracting more and more attention as an emerging platform in the fields of biophysics, material science, and biomedical engineering due to their tunable physical properties, high surface area, remarkable photoluminescence, as well as easy chemical functionalization. Beyond their applications in nanomedicine for drug/gene delivery, phototherapy, and bioimaging, they have shown excellent interaction and adhesive properties for protein, mammalian cells, and microbes, which makes them hybrid architectures potential platforms for multifunctional biological applications.

References

- [1] B. Brodie, *Annales de Chimie et de Physique* 45 (1855) 351.
- [2] L. Staudenmaier, *Chemische Berichte* 31 (2) (1898) 1481.
- [3] W. S. Hummers and R. E. Offeman, *Journal of American Chemical Society* 80 (6) (1958) 1339.
- [4] M. Dimiev and J. M. Tour, *ACS Nano* 8 (3) (2014) 3060.
- [5] K. S. Novoselov et al., *Nature* 490 (2012) 192.
- [6] M. Pumera, *Energy and Environmental Science* 4 (2011) 668.
- [7] X. Huang et al., *Small* 7 (2011) 1876.
- [8] S. Pei and H. Cheng, *Carbon* 50(9) (2012) 3210.
- [9] C. K. Chua and M. Pumera, *Chemical Society Reviews* 43 (2014) 291.
- [10] R. Wang, Y. Wang, C. Xu, J. Sun and L. Gao, *RSC Advances* 3 (2013) 1194.
- [11] Dimiev et al., *Journal of American Chemical Society* 134 (5) (2012) 2815.
- [12] G. Charpy, *Comptes rendus de l'Académie des sciences* 148 (5) (1909) 920.
- [13] M. Dimiev, L. B. Alemany, and J. M. Tour, *ACS Nano* 7 (1) (2013) 576.
- [14] M. Dimiev and T. A. Polson, *Carbon* 93 (2015) 544.
- [15] M. Dimiev, D. V. Kosynkin and A. Sinitskii, *Science* 331 (6021) (2011) 1168.
- [16] K. Chua and M. Pumera, *Chemical Communications* 52 (2015) 72.
- [17] T. Tsuchiya, K. Terabe and M. Aono, *Advanced Materials* 26(7) (2013) 1087.
- [18] K. Erickson, R. Erni, Z. Lee, N. Alem, W. Gannett and A. Zettl, *Advanced Materials* 22 (2010) 4467.
- [19] Briggs, in *Handbook of X-ray Photoelectron Spectroscopy*, vol. 3, eds C. D. Wagner, W. M. Riggs, L. E. Davis, J. F. Moulder and G.E. Muilenberg. Perkin-Elmer Corp., Eden Prairie, MN, 1979.
- [20] G. B. Hofflund, *Spectroscopic techniques: X-ray photoelectron spectroscopy (XPS), Auger electron spectroscopy (AES) and ion scattering spectroscopy (ISS)*. In *Handbook of Surface and Interface Analysis*. Marcel Dekker, New York, 1998.
- [21] P. L. Chiu et al., *Journal of American Chemical Society* 134 (13) (2012) 5850.
- [22] Ganguly, S. Sharma, P. Papakonstantinou, J. Hamilton, *Journal of Physical Chemistry C* 115 (34) (2011) 17009.
- [23] S. Stankovich, R. D. Piner, X. Chen, N. Wu, S. T. Nguyen and R. S. Ruoff, *Journal of Materials Chemistry* 16 (2006) 155.
- [24] C. Ferrari and J. Robertson, *Physical Review B* 61(20) (2000) 14095.
- [25] F. Tuinstra and J. L. Koenig, *the Journal of Chemical Physics* 53(3) (1970) 1126.
- [26] K. N. Kudin et al., *Nano Letters* 8 (1) (2008) 36.
- [27] G. Eda and M. Chhowalla, *Advanced Materials* 22 (22) (2010) 2392.
- [28] Das et al., *Nature Nanotechnology* 3 (4) (2008) 210.
- [29] P. K. Ang et al., *ACS Nano* 3 (11) (2009) 3587.
- [30] R. Voggu, B. Das, C. S. Rout and C. N. R. Rao, *Journal of Physics: Condensed Matter* 20 (2008) 472204.
- [31] K. Krishnamoorthy, M. Veerapandian, R. Mohan and S.-J. Kim, *Applied Physics A* 106 (3) (2012) 501.
- [32] T. V. Cuong et al., *Materials Letters* 64 (6) (2010) 765.
- [33] Mattevi et al., *Advanced Functional Materials* 19 (16) (2009) 2577.
- [34] Gómez-Navarro et al., *Nano Letters* 7 (11) (2007) 3499.
- [35] N. Mohanty, A. Nagaraja, J. Armesto and V. Berry, *Small* 6 (2) (2010) 226.
- [36] V. Lee et al., *Chemistry of Materials* 21 (16) (2009) 3905.
- [37] S. Wang et al., *Nano Letters* 10 (1) (2010) 92.
- [38] S. Stankovich et al., *Carbon* 45 (7) (2007) 1558.
- [39] V. C. Tung, M. J. Allen, Y. Yang and R. B. Kaner, *Nature Nanotechnology* 4 (1) (2009) 25.
- [40] J. I. Paredes et al., *Langmuir* 25 (10) (2009) 5957.
- [41] S. Perumbilavil, P. Sankar, P. R. Thankamani and R. Philip, *Applied Physics Letters* 107(5) (2015) 051104.
- [42] J. Shang et al., *Scientific Reports* 2 (2012) 792.
- [43] X.-F. Zhang, X. Shao and S. Liu, *Journal of Physical Chemistry A* 116 (27) (2012) 7308.
- [44] J.-L. Chen, X.-P. Yan, *Journal of Material Chemistry* 20 (2010) 4328.
- [45] S. Kochmann, T. Hirsch and O. S. Wolfbeis, *Journal of Fluorescence* 22 (3) (2012) 849.
- [46] J.-L. Chen, X.-P. Yan, K. Meng and S.-F. Wang, *Analytical Chemistry* 83 (22) (2011) 8787.
- [47] J. D. Ingle, S. R. Crouch, *Spectrochemical Analysis*. Prentice-Hall, Englewood Cliffs, NJ, 1988.
- [48] D. Dimiev and S. Eigler, *Graphene Oxide: Fundamentals and Applications*, John Wiley & Sons, West Sussex, United Kingdom, 2016.

- [49] M. Li et al., *Journal of Material Chemistry* 22 (44) (2012) 23374.
- [50] G. Eda et al., *Advanced Materials* 22 (4) (2010) 505.
- [51] Li et al., *Nature Nanotechnology* 3 (2) (2008) 101.
- [52] Galande et al., *Scientific Reports* 1 (2011) 85.
- [53] Z. Luo et al., *Applied Physics Letters* 2009, 94, 111909.
- [54] Kozawa, Y. Miyauchi, S. Mouri and K. Matsuda, *the Journal of Physical Chemistry Letters* 4 (12) (2013) 2035.
- [55] T. Gokus et al., *ACS Nano* 3 (12) (2009) 3963.
- [56] P. Johari and V. B. Shenoy, *ACS Nano* 5 (9) (2011) 7640.
- [57] Kozawa et al., *the Journal of Physical Chemistry Letters* 5 (10) (2014) 1754.
- [58] L. Exarhos, M. E. Turk and J. M. Kikkawa *Nano Letters* 13 (2013) 344.
- [59] T. V. Cuong et al., *Materials Letters* 64 (3) (2010) 399.
- [60] C.-T. Chien et al., *Angewandte Chemie International Edition* 51 (27) (2012) 6662.
- [61] Yin, S. Wu, Y. Wang, L. Wu, P. Yuan and X. Wang, *Journal of Solid State Chemistry* 237 (2016) 57.
- [62] Nourbakhsh et al., *Nanotechnology* 21 (43) (2010) 435203.
- [63] K. Jeong et al., *Journal of Physics D: Applied Physics* 42 (2009) 065418.
- [64] Y. Dong et al., *Carbon* 50 (12) (2012) 4738.
- [65] Q. Mei et al., *Chemical Communications* 46 (39) (2010) 7319.
- [66] Z. X. Gan et al., *Nano Letters* 11 (9) (2011) 3951.
- [67] Y. M. Yoo, J. H. Kang and B. H. Hong, *Chemical Society Reviews* 44 (2015) 4835.
- [68] X. Zhu, Y. Liu, P. Li, Z. Nie and J. Li, *Analyst* 141 (2016) 4541.
- [69] C. Lu, P. J Huang, B. Liu, Y. Ying and J. Liu, *Langmuir* 32 (2016) 10776.
- [70] M. Orecchioni, C. Menard-Moyon, L. G. Delogu and A. Bianco, *Graphene and the immune system: Challenges and potentiality. Advanced Drug Delivery Reviews* 105 (2016) 163.
- [71] B. Zhang, P. Wei, Z. Zhou and T. Wei, *Advanced Drug Delivery Reviews* 105 (2016) 145.
- [72] J.-L. Chen and X.-P. Yan, *Chemical Communications* 47 (11) (2011) 3135.
- [73] Z. Qian et al., *Journal of Materials Chemistry* 21 (44) (2011) 17635.
- [74] X. Sun et al., *Nano Research* 1 (3) (2008) 203.
- [75] X. Yan et al., *the Journal of Physical Chemistry Letters* 2 (10) (2011) 1119.
- [76] Z. Liu, J. T. Robinson, X. Sun, and H. Dai, *Journal of American Chemical Society* 130 (33) (2008) 10876.
- [77] Kim et al., *Bioconjugate Chemistry* 22 (12) (2011) 2558.
- [78] Y. Wang et al., *Trends in Biotechnology* 29 (5) (2011) 205.
- [79] Y. Lu et al., *Journal of Materials Chemistry* 22 (7) (2012) 2929.
- [80] C. Cheng, S. Li, A. Thomas, N. A. Kotov and R. Haag, *Chemical Reviews* 117 (2017) 1826.
- [81] V. Georgakilas et al., *Chemical Reviews* 116 (9) (2016) 5464.
- [82] S. Shi, F. Chen, E. B. Ehlerting, and W. Cai, *Bioconjugate Chemistry* 25 (2014) 1609.
- [83] L. Feng, S. Zhang, and Z. Liu, *Nanoscale* 3 (2011) 1252.
- [84] S. Eigler and A. Hirsch, *Angewandte Chemie International Edition* 53 (2014) 7720.
- [85] Q. Lai et al., *AIP Advances* 2 (2012) 032146.
- [86] Kundu, R. K. Layek and A. K. Nandi, *Journal of Materials Chemistry* 22 (16) (2012) 8139.
- [87] H. Lu et al., *Angewandte Chemie International Edition* 48 (26) (2009) 4785.
- [88] S. Wang et al., *ACS Nano* 5 (8) (2011) 6202.
- [89] Liu et al., *Journal of Polymer Science Part A: Polymer Chemistry* 48 (2) (2010) 425.
- [90] Q. Lai et al., *AIP Advances* 2 (2012) 032146.
- [91] S. Saxena et al., *Applied Physics Letters* 99 (2011) 013104.
- [92] M. Li et al., *Advanced Materials* 24 (2012) 1722.
- [93] X. Sun et al., *Nano Research* 1 (3) (2008) 203.
- [94] M. S. Khan, H. N. Abdelhamid, H.-F. Wu, *Colloids Surfaces B: Biointerfaces* 127 (2015) 281.
- [95] T. S. Hauck et al., *Advanced Materials* 20 (2008) 3832.
- [96] W. Zhang et al., *Biomaterials* 32 (2011) 8555.
- [97] Wu et al., *Nanotechnology* 23 (2012) 355101.
- [98] Feng, S. Zhang and Z. Liu, *Nanoscale* 3 (2011) 1252.
- [99] Zhang et al., *Small* 7 (4) (2011) 460.
- [100] X. Yang et al., *Journal of Materials Chemistry* 22 (2012) 6649.
- [101] C.-H. Lu et al., *Chemical Communications* 46 (2010) 3116–3118.
- [102] Y. Wang et al., *Journal of American Chemical Society* 132 (2010) 9274.
- [103] Tang, Y. Wang, and J. Li, *Chemical Society Reviews* 44 (2015) 6954.
- [104] Wu et al., *Langmuir* 27 (2011) 2731.
- [105] M. Zheng et al., *Nature Materials* 2 (2003) 338.

[106] B. J. Hong, Z. An, O. C. Compton and S. B. Nguyen, *Small* 8 (16) (2012) 2469.

III Experimental techniques and methods

In this dissertation, various experimental techniques were employed for the assessment of the physical properties of fabricated fluorescent nanostructures. In the first part of the section (III.1) we will report on fabrication procedures for silver nanoparticles (AgNP) and tryptophan functionalized silver nanoparticles (AgTrp). In the second part, we will present preparation procedures for graphene oxide (GO) and reduced graphene oxides. After that, we will describe methods for preparation of biological samples for the experiments (section III.2). Methods used for the structural characterization of fluorescent nanostructures are given in section III.3 and spectroscopy techniques in section III.4. Deep-UV (DUV) fluorescence microscopy technique along with image processing is presented in the last section (III.5).

III.1. Procedures for the fabrication of fluorescent nanomaterials

III.1.1. Tryptophan functionalized silver nanoparticles

Silver hydrocolloids (Ag NP) were prepared by the chemical reduction of silver nitrate AgNO_3 (0.1 mM) by NaBH_4 . In a 100 mL of argon saturated aqueous solution of 2×10^{-4} M AgNO_3 , 10 mg of NaBH_4 was added under vigorous stirring, resulting in formation of a transparent yellow colloidal silver solution (Figure III.1.1i). Tryptophan-functionalized silver nanoparticles (AgTrp) were prepared by adding an appropriate amount of 1 ml Trp aqueous solution (1 mM) into 10 ml of silver colloid with pH value previously adjusted to 10.4 by addition of 0.1 M NaOH solution. The mixture was stirred for 30 minutes and subsequently investigated. The list of the samples prepared, their labels and the amount of chemicals used are given in the Table III.1. A fresh batch of samples was prepared using the same conditions prior to all analyses.

Table III.1. The list of samples and the amount of chemicals used in the preparation

Sample	V (0.1 mM Ag NP) [ml]	V (1 mM Trp)[ml]	n_m (Ag): n_m (Trp) ^b
Trp1.0	0 ^a	1.0	0
Ag NP	10	0.0	∞
AgTrp0.3	10	0.3	10:3
AgTrp0.5	10	0.5	2:1
AgTrp1.0	10	1.0	1:1
AgTrp2.0	10	2.0	1:2

^a- in 10 ml H_2O ; ^b-Ag:Trp molar ratio.

Silver ions in saline solution tend to form non-biocompatible complex with chlorine and form AgCl which leads to a decrease in silver concentration in the system. Since saline solution is used as a cell dispersion medium it is important to test chemical stability of silver hydrocolloids in this environment. The chemical stability of Ag NP and AgTrp hydrocolloids in the presence of saline (0.9% NaCl) was investigated by UV-vis spectroscopy. For these analyses, 4 ml of the as prepared Ag NP, AgTrp1.0 or AgTrp2.0 colloids were mixed with 1 ml of saline. The mixtures were held at 37 °C and the intensity of surface plasmon resonance at 400 nm was subsequently measured by UV-vis.

To test the efficiency of the functionalization of the silver nanoparticles by tryptophan and its photoluminescence properties, we performed the phase transfer of the colloid from water into an organic solvent. If the tryptophan was attached to the surface of the nanoparticles, the phase transfer may occur due to the presence of hydrophobic indole side groups. The tests were performed by mixing 1 ml of toluene with 5 ml of Ag NPs or AgTrp2.0 colloid in the glass test tubes, followed by vigorous shaking of the tubes for 5 minutes. The photographs of the vials containing Ag NPs and AgTrp2.0 colloids with and without toluene are presented in Figure III.1.1a-d. The phase transfer into an organic phase was observed solely in the case of the functionalized silver nanoparticles, indicating efficient capping of their surfaces by the amino acid.

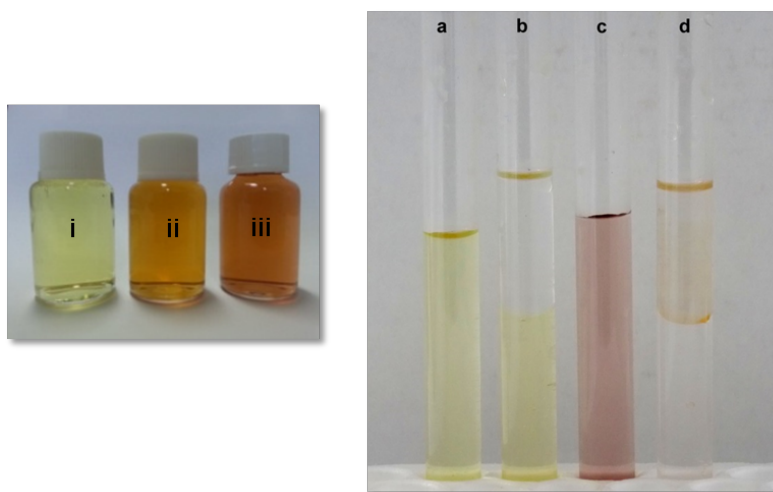


Figure III.1.1. Photographs of (i) hydrocolloids of silver nanoparticles (AgNP) and (ii,iii) tryptophan functionalized silver nanoparticles AgTrp1.0 and AgTrp2.0. Phase transfer in toluene of a,b) bare AgNP and c,d) AgTrp2.0

III.1.2. Graphene oxide and the reduction of graphene oxide

Graphene Oxide (GO) was synthesized using modified Hummers method. We used 150 g of expanded graphite (EG) as a starting material. We employed sulfuric acid (H_2SO_4) as the intercalating compound. Volume quantity of 6 ml of (95-98%) H_2SO_4 was added to the pillared pieces of EG and mixed at $0\text{ }^\circ\text{C}$ for two hours. The mixture was then left overnight and kept at room temperature. By adding 450 mg of potassium permanganate (KMnO_4), we engaged the oxidation to the graphite 3D structure and replacement of the acid intercalant. We added 28 ml of DI water and then we prepared oil bath (kept the temperature at $90\text{-}95\text{ }^\circ\text{C}$) and used it to heat the oxidized graphite for two hours. Then, the oxidized graphite mixture was cooled down to the room temperature. After that, we added 84 ml of 3% solution of H_2O_2 in order to stop possible reduction from occurring. Repeated cycles of centrifugation (at 5500 rpm) and washing with 5% HCl solution were conducted until brown solution was obtained indicating that successful intercalation/oxidation occurred and the formation of graphite oxide (GtO). The sonification of GtO by using Branson W-450 D Digital Sonifier with 20% amplitude (80W) for 10 minutes made a graphite oxide solution to change color from light brown to light yellow. Transparent light yellow supernatants were obtained after another cycle of centrifugation and washing which indicated formation of small sized multi/monolayered graphene oxide (GO) (Figure III.1.2).



Figure III.1.2. Photograph of glass bottles containing water dispersions of graphene oxide (GO), partially reduced graphene oxide (prGO) and reduced graphene oxide (rGO).

The reduction of as prepared GO was directed in the presence of 30% concentrated solution of hydrazine (N_2H_4) hydrate. First, the glass with 0.1 mg/ml of GO solution was introduced into an oil bath which was heated to $95\text{ }^\circ\text{C}$. After that 100 μl of hydrazine solution (30%) was poured into heated GO solution, end it represented the start of the reduction

process. After that, for different reduction times, the same volume of graphene oxide during the reduction was extracted and diluted with DI water in order to stop the reduction process. In this way we fabricated partially reduced forms of GO with light yellow color changing to gray (Figure III.1.2). The stability of prGO samples with different times of reduction was monitored in order to confirm stopping of reduction process and the results showed sustainable optical properties without solution precipitation over month's period of time, except for totally reduced GO.

III.2. Preparations of biological samples for experiments

III.2.1. Cell cultures

Microorganisms that are used in this dissertation are Gram-negative bacteria *Escherichia coli* (ATCC strain number 25922), unicellular eukaryote fungus *Candida albicans* (ATCC strain number 10259) and hepatocyte derived cellular carcinoma cell line Huh7.5.1. *Escherichia coli* and *Candida albicans* cells are incubated with tryptophan functionalized silver nanoparticles. Cancer liver cells Huh7.5.1 are treated with graphene oxide and reduced graphene oxides.

III.2.2. Antimicrobial, adaption and uptake tests of microbial cells

The quantitative testing of AgNP, AgTrp1.0 and AgTrp2.0 antimicrobial activity against *E. coli* was assessed in a potassium hydrogen phosphate buffer solution (pH 7.00). For inoculum preparation, the microorganisms were cultivated in TSYB at 37 °C and left overnight (late exponential stage of growth). The solutions with specific concentrations of silver were obtained by mixing the colloids with sterile physiological saline solutions. Thereafter, 400 µl of the solutions were placed in Eppendorf tubes containing 100 µl of microbial inoculum. The resulting mixture was vortexed for 10 s and incubated at 37 °C in a water bath shaker. After 2 h, the dispersions were placed in Petri dishes, overlaid with TSYA (0.6% of agar-agar in Trypton soy broth) and after 24 h of incubation at 37 °C, the counts of

viable microorganisms were determined. The percentage of reduction of the microbial cells (R,%) was calculated using the following equation:

$$R, [\%] = \frac{CFU_{cont} - CFU_{coll}}{CFU_{cont}} \times 100\% \quad \text{Eq. III.1.}$$

where CFU_{cont} and CFU_{coll} are the numbers of colony forming units per milliliter for the control and the silver colloid solutions, respectively. All experiments were performed in triplicates and the results are shown as mean values. Data were analyzed using analysis of variance (one-way ANOVA) and the Tukey test was applied as a test for comparison of mean values with a significance level of 0.1. The uptake of the nanoparticles by *E. coli* cells was determined by measuring the intensity of the surface plasmon resonance peak of silver nanoparticles before and after interaction with bacteria.

The growth of pathogen fungus *C. albicans* (ATCC 10259) strain was carried out in a Trypton Soy broth or agar (TSYB or TSYA—Institute of Immunology and Virology, Torlak, Belgrade), supplemented with 0.6% (v/v) yeast extract. For inoculum preparation, the microorganisms were cultivated in TSYB at 37°C and left overnight (early exponential stage of growth). The culture media was prepared using distilled water and sterilized by conventional methods. The initial concentration of the cell dispersion was 10^6 CFU ml⁻¹. The initial cell dispersion (concentration $\sim 10^6$ CFU ml⁻¹) was used in the tests, except in the adaptation test, where the concentration was adjusted to 10^4 CFU ml⁻¹ by dilution with saline. The solutions with specific concentrations of tryptophan, AgNPs, and AgTrp2.0 were prepared by mixing the colloids with sterile physiological saline solutions. After that, 400 µl of the solutions were placed in tubes containing 100 µl of purified microbial dispersion. The resulting mixture was vortexed for 10 s and incubated at 37°C for two hours. In order to test the antimicrobial activity, the dispersions were placed in Petri dishes, overlaid with TSYA (0.6% of agar–agar in Trypton soy broth). After 24 h of incubation at 37°C, the counts of viable microorganisms were determined. Because the AgNP can inhibit yeast growth of *C. albicans*, we conducted 24 h adaptation tests of *C. albicans* incubated with AgTrp2.0 in the presence of TSB as a growth medium. The uptake test was performed after mixing of *C. albicans* dispersion with AgTrp2.0 colloid (the preparation procedure was the same as the one used for the antimicrobial tests). The mixture was centrifuged at 3000 rpm for 10 min. The optical densities at 400 nm were measured prior and after centrifugation of the mixture.

For comparison, the OD400 values were also determined for the starting *C. albicans* dispersion (prior and after centrifugation) under the same conditions.

III.2.3. Preparation of biological samples for deep-UV imaging

The first type of biological sample for DUV imaging was prepared by adding different volume ratios of AgTrp1.0 or AgTrp2.0 colloids and saline into 100 μl of purified *Escherichia coli* (ATCC 25922) saline dispersion. Upon mixing, the samples were incubated at 37 $^{\circ}\text{C}$ for 2 h. After that, 10 μl of each sample were placed on quartz coverslips, dried under ambient conditions and immediately examined by DUV fluorescence imaging. The control samples were prepared using the same procedures and conditions, but without adding the colloid. The procedure for the quantitative determination of the number of colonies was repeated for the samples used in the DUV fluorescence imaging test. After two hours of incubation, the samples were centrifuged at 7000 rpm in order to precipitate the live cells. The precipitated cells were dispersed in TSYB and the number of colonies was found to be 10^2 CFU ml^{-1} (the initial number of colonies was 10^6 CFU ml^{-1}). After 20 hours in TSYB, the number of colonies increased to 36×10^6 CFU ml^{-1} proving that the certain number of cells survived the incubation. An image of the test tubes with TSYB immediately after mixing with the precipitated cells and after 20 h at 37 $^{\circ}\text{C}$ is shown in Figure III.2.1.



Figure III.2.1. The optical image of the test tubes that contain TSYB. Left) The mixture of TSYB and *E. coli* cells incubated with AgTrp2 for 2 h. Right) The same mixture after 20 h at 37 $^{\circ}\text{C}$. An increase in optical density (from 0.013 to 0.759 at 600 nm) indicates the cell growth (that the sufficient number of cells survived the treatment).

The second type of biological sample for DUV imaging was obtained by adding different volume ratios of tryptophan solution (Trp2.0) as well as Ag NPs and AgTrp2.0 colloids into 100 μl of purified *C. albicans* saline dispersions. The mixtures were incubated at

37 °C for 2 h and then 10 µl of each sample was placed on quartz cover-slips. The samples were left to dry at ambient conditions. After that, they were washed with distilled water to remove unattached and dead cells and immediately examined by DUV fluorescence imaging. The control sample of untreated *C. albicans* cells was prepared by using the same procedures and conditions, but without adding the tryptophan solution and/or the colloids.

The third type of biological sample used in DUV imaging were cancer liver cells (cell line Huh7.5.1) incubated with graphene functionalities: graphene oxide (GO), partially reduced graphene oxide (prGO) and reduced graphene oxide (rGO). Two concentrations (10^{-5} M and 10^{-6} M) were used for 7h of incubation time with initial number of cell colonies 10^5 CFU ml⁻¹ in calf fetal serum. 300 µl and 1 ml from the stock solutions of GO, prGO and rGO were mixed with 3 ml of cell's culture medium. After the incubation, cells were washed with PBS and fixed with 4% of PFA. 10 µl of each sample was deposited on the quartz coverslips, dried and placed in the appropriate holder for bioimaging. The control sample was prepared in the same way but without adding graphene's functionalities.

III.3. Methods for structural characterization of fluorescent nanomaterials

III.3.1. Raman imaging coupled with atomic force microscope (Raman/AFM)

In this dissertation we have used AFM coupled with Raman microscope in order to investigate morphology of the graphene oxides layers and to obtain high specific Raman data from discrete points. Collocated Raman/AFM system is using motorized AFM integration arm with objective at 90 degrees relative to the sample. In this way, efficient direct laser coupling to sample on AFM platform is gained. A Renishaw inVia Raman microscope equipped with 532 nm laser excitation in combination with a 2400 l/mm grating (producing a nominal spectral resolution of 1 cm⁻¹) was used to characterize the structural species of GO, prGO and rGO. Samples were analyzed spatially by using either fast Raman imaging technique StreamLineHR or confocal depth profiling. This allows the distribution of the different chemical or structural species to be determined.

III.3.2. Scanning electron microscopy (SEM)

The microstructure morphology of graphene oxide was investigated by using a JEOL JSM-6390 scanning electron microscope (SEM). Because of the low electrical conductivity of graphene oxide, the surface was covered with thin layer of gold. High-quality micrographs of GO were obtained with x4300 magnification and operating voltage value of 13 kV.

III.3.3. Transmission electron microscopy

The morphology of the Ag and AgTrp nanostructures was investigated by transmission electron microscopy (JEOL JEM-1400 instrument) at 120 kV operating voltage. Aqueous dispersions of the colloids were deposited on carbon coated copper grids using an automatic pipette. The samples were left to dry under ambient conditions before they were transferred to the TEM chamber. The distribution of particle sizes was determined by measuring the diameters of the equivalent circular area of at least 100 observed particles.

Due to significantly higher magnification (x225000) provided by high resolution transmission electron microscopy (HRTEM) single layers of GO, prGO and rGO samples were detected for 200 kV operating voltage value. Energy dispersion spectroscopy (EDS) coupled with HRTEM allowed inspection of the elemental composition of the monolayers.

III.4. Spectroscopy techniques for characterization of fluorescent nanomaterials

III.4.1. Absorption spectroscopy in the visible and ultra-violet part of the EM spectrum

The UV-vis absorption measurements of the aqueous dispersions were carried out on a Thermo Evolution 600 spectrophotometer. The change in optical properties of silver nanoparticles before and after functionalization with tryptophan was investigated by using UV-vis. Also, UV-vis was employed in monitoring the influence of the reduction time on optical properties of graphene oxide and changes in optical bands.

III.4.2. Emission spectroscopy in the visible and ultra-violet part of the EM spectrum

The photoluminescence spectra of aqueous tryptophan solution and AgTrp colloids were recorded using a PerkinElmer LS45 fluorescence spectrophotometer. Fluorolog-3 Model FL3-221 spectrofluorometer system (Horiba Jobin Yvon) was employed for measuring quantities of fluorescence excitation emission matrices. Xenon lamp (450 W) was used as an excitation source and TBX-04 as a detector. Both excitation and emission monochromators were double grating, with dispersion of 2.1 nm/mm (1200 grooves/nm). All measurements were performed in the front face geometry at the room temperature. EEM fluorescence landscapes were obtained by recording the emission spectra from 330 to 650 nm at 2 nm intervals, for excitations ranging between 270 and 430 nm changed in 2.5 nm steps. For these measurements excitation slit was set at 6 nm, emission slit was at 2 nm and integration time was fixed to 0.4 ms. Changes in excitation power were corrected using reference photodetector.

III.4.3. Fourier transform infrared spectroscopy (FTIR)

FTIR spectroscopy was carried out at room temperature using a Nicolet 380 spectrophotometer in the spectral range of 4000–400 cm^{-1} , with a resolution of 4 cm^{-1} . The datasets were averaged over 200 scans. In these analyses, the samples were 150 mg KBr pellets that contained 2 mg of the sample.

III.4.4. X-ray photoelectron spectroscopy (XPS)

XPS experiments were performed on a Physical Electronics Quantum 2000 instrument using Al $K\alpha$ radiation (1486.6 eV). The spectra of C 1s, O 1s, Ag 3d, and N 1s core levels were recorded at 29.35 eV pass energy and at 55° take-off angle. The peak shift due to charge accumulation was corrected using the C 1s level at 284.4 eV as an internal standard. The XPS peaks are assumed to be linear combinations of Lorentzian and Gaussian line shapes and were resolved into individual components after proper subtraction of the baseline using the Shirley background subtraction method.

III.5. Deep-UV fluorescence microscopy

III.5.1. Experimental conditions for DUV imaging

DUV fluorescence imaging of microorganisms incubated with AgTrp colloids (*E. coli* and *C. albicans*) and graphene's functionalities (Huh7.5.1) was performed at DISCO beamline of SOLEIL synchrotron facility (France). The fluorescence images were collected on the TELEMOS endstation of DISCO.

Bioimaging of live *E. coli* cells and live *E. coli* cells incubated with AgTrp colloids was performed by acquiring the luminescence signals in the [327–353 nm], [370–410 nm], and [452–486 nm] wavelength ranges for 6 minutes upon illumination of the samples with $\lambda_{\text{exc}} = 280$ nm synchrotron radiation. Each sample was prepared three times and at least 6 different locations ($150 \times 75 \mu\text{m}$) were investigated for each sample to ensure the consistency of the observations. To avoid the effects of photobleaching on the intensity of the fluorescence signal, the images on each of the locations were acquired for only two sets of conditions.

As for the fluorescence images of *C. albicans* cells and *C. albicans* cells incubated with tryptophan, Ag NPs, and AgTrp NPs, synchrotron UV radiation with wavelength of 290 nm was used as an excitation source and the luminescence signal was collected in the [327–353 nm] and [370–410 nm] wavelength ranges for 30 s. To ensure consistency of the observations at least 10 different locations ($155 \times 60 \mu\text{m}$) were investigated by means of DUV imaging.

The fluorescence images of Huh7.5.1 cells and Huh7.5.1 cells incubated with GO, prGO and rGO were collected in the [327 - 353 nm], [370 - 410 nm] and [420 - 480 nm] wavelength ranges for 30 seconds, for excitation wavelength of 270 nm. At least 20 different locations ($79.96 \times 79.96 \mu\text{m}$ 1024x1024) per coverslip were investigated for deep UV bioimaging.

Ultrafluar glycerin immersion objective (Zeiss, Germany) with 100x magnification was used for collecting all the images. Under these conditions, the pixel size on the fluorescence images projected on the camera chip of a PIXIS 1024 BUV camera (Princeton, USA) corresponds to 154 nm. The whole setup was controlled by μ Manager and the images were analyzed by using FIJI software.

III.5.1. Processing of the fluorescence images

The processing of the fluorescence images obtained by the DUV fluorescence imaging was minimal in order to preserve original information from the images and focused on improvement of the presentation of the results. In addition, since the fluorescence intensity at a given pixel presents realistic intensity of the light of specific energy emitted from that location, it is possible to get additional information from this spatially resolved fluorescence by using appropriate mathematical transformations.

The first step is pseudo coloring a fluorescence image with LUT (Look Up Table) of interest. This was carried out to emphasize differences in intensity of fluorescence signal coming from cells. Calibration bar represents the minimum and maximum values of the fluorescence intensity. For a LUT colored fluorescence image, the minimum of the intensity is assigned to the black color and the maximum is assigned to the white color. Intermediate colors are dependent upon choosing LUT of interest (Figure III.5.1., Magenta and Fire LUT).

The second step is an option “Find maxima” which determines local maxima in an image. This is done in order to localize and compare decay kinetics of intensities of maxima on the fluorescence image. A threshold is set at the maximum value minus noise tolerance and the contiguous area around the maximum above the threshold is analyzed.

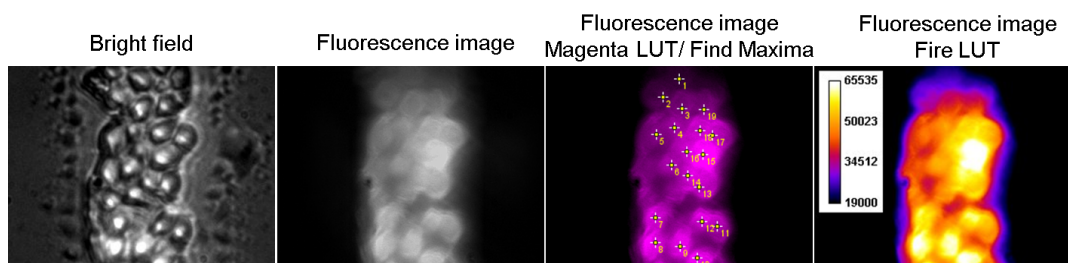


Figure III.5.1. Step by step procedure of processing images of *C. albicans* obtained with DUV fluorescence imaging.

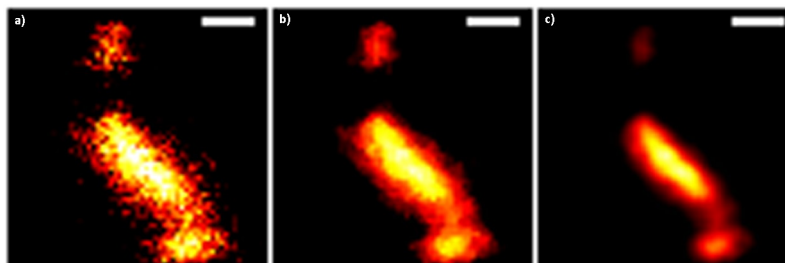


Figure III.5.2. Steps in fluorescence image processing of *E. coli*: a) raw image, b) noise reduced and background subtracted image, and c) contrast enhanced and mean filtered image. Pixel size in the images is equal to 154 nm. Scale bars in the images correspond to 2 μm .

Bleaching kinetics of the cells was analyzed by using a plugin PixBleach, developed in Fiji software. The intensities from the bleach stacks are fitted to Kohlrausch function, a generalized exponential function with an additional stretching parameter,

$$I(t)=A\times\exp(-t/\tau)^{1/h}+B, \quad \text{Eq.III.2}$$

where A is the decay amplitude, B is a measure of the background autofluorescence, τ is the bleach time constant and h is the heterogeneity factor. Eq.III.2 was used to fit the fluorescence intensities of at least 10 images in a stack. The amplitude corresponded to initial fluorescence intensity (prior to bleaching). Bleach time constant is the parameter that characterizes the lifetime of the fluorophore in the structure, while heterogeneity factor is related to the width of the τ -distribution values. Time integrated emission (TIE) was estimated as the total signal intensity emitted by the fluorophores before their complete photodestruction. The stack images and calculated parameters are presented in detail in the results section.

IV Physical properties of fluorescent nanostructures and their interaction with biological systems

In the previous section we presented procedures for the fabrication of tryptophan functionalized silver nanoparticles (AgTrp) and graphene-based nanomaterials: graphene oxide (GO), partially reduced graphene oxide (prGO) and reduced graphene oxide (rGO). We described the incubation conditions and the methods for preparation of biological samples for the experimental investigations. The interaction of fabricated nanostructures with biological systems is highly depended on surface properties of the nanomaterials. Therefore, we have used spectroscopy and microscopy experimental techniques in order to study the physical properties altered by the functionalization process of nanostructures.

Tryptophan is the largest essential amino acid that exhibits fluorescence excitation and emission maxima in the ultraviolet (UV) region [1]. Silver nanoparticles efficiently interact with visible light because of the collective resonance of the conduction electrons in the metal (surface plasmon resonance). Surface modification of silver nanoparticles with tryptophan results in nanostructures that both resonantly absorb electromagnetic radiation and exhibit intense fluorescence [2]. Because of this added property, a new functionality of the silver nanoparticles can arise, or more specifically, they can be used as fluorescent probes in the investigations of the antimicrobial activity of silver in live biological systems. To test this assumption, we have performed a challenging study of DUV fluorescence imaging of bacterial cells of *Escherichia coli* and fungus *Candida albicans* incubated with AgTrp fluorescent nanostructures using UV synchrotron radiation as an excitation source, and the results of these investigations will be given in the section IV.1 of this chapter.

Graphene oxide (GO) is the second type of fluorescent nanostructure that is presented in this dissertation. Optical properties of GO significantly depend on the relative ratios of different oxygen functional groups of GO and are strongly influenced by the continuous interactions of functional groups of GO with the dispersed aqueous environment. GO is an electronically hybrid material that has both conducting π -states from sp^2 carbon sites and a large energy gap between the σ -states of its sp^3 -bonded carbons. The control of the ratio of the sp^2 and sp^3 fractions by the reduction process is a powerful way to tune its bandgap and therefore controllably transform GO from an insulator to a graphene-like semi-metal [3]. The fluorescence emission (in the range of 350–600 nm) exhibited by monolayer GO sheets

dispersed in aqueous medium has larger contributions from disorder induced localized states formed due to the presence of oxygen functional groups rather than sp^2 carbon domains of GO. With the partial reduction of GO, the scavenging of oxygen functional groups is occurring and it influences the size of sp^2 clusters [4]. This reflects in larger contribution of sp^2 sites to the fluorescence emission and the enhancement of the quantum yield. Newly created fluorescence properties of GO, by careful reduction process, can be used in bioimaging. The toxicology effects of GO and reduced GOs are explored in bioimaging of cancer liver cells Huh7.5.1.

Results and discussion chapter of this dissertation is organized in two sections: In section IV.1 we will present structural and optical properties of tryptophan functionalized silver nanoparticles (AgTrp), and bioimaging of AgTrp fluorescent structures in interaction with pathogen cells of bacteria (*E. coli*) and fungus (*C. albicans*). In section IV.2, we characterize the physical properties of fluorescent nanostructures of graphene oxide (GO), partially reduced graphene oxide (prGO) and reduced graphene oxide (rGO). We investigate the interaction of GO, prGO and rGO with cancer liver cells (Huh7.5.1) by means of fluorescent bioimaging.

IV.1. DUV fluorescence imaging of microbial cells incubated with tryptophan functionalized silver nanoparticles

Silver nanoparticles are efficient antimicrobial agents with low toxicity and their antimicrobial activity was tested against different pathogen strains, including bacteria representative *Escherichia coli* and the most common pathogen fungus *Candida Albicans* [5, 6]. The details of the mechanisms of antimicrobial action of silver nanoparticles on *E. coli* still remain to be recognized; however, several studies have demonstrated that silver ions released from the nanoparticles interact with the sulfhydryl and phosphate groups of outer membrane proteins leading to dysfunction in their permeability, enzymatic signaling activity and respiratory processes [7-9]. Concerning *C. albicans* cells, Vazquez-Munoz et al. [10] reported that the nanoparticles tend to accumulate in the cell walls and induce cell death by releasing silver ions. In addition, it was shown that silver nanoparticles induce intracellular accumulation of reactive oxygen species (ROS) and alter mitochondrial membrane potential of [11]. The resistance of *C. albicans* to the action of silver nanoparticles gradually increases as their growth proceeded from adhered cells to pre-formed biofilm and, finally, to mature biofilm [12, 13].

Silver ions Ag^+ poses more pronounced antimicrobial properties in comparison to the silver nanoparticles [14]. The diffusion of Ag^+ ions in microbial cells is limited due to the high reactivity of the ions with intracellular species. Consequently, silver nanoparticles can be regarded as carriers of Ag^+ ions that, by using appropriate surface modification, can be transported to the specific cell sites and inflict more efficient damage with Ag^+ release. Therefore, in order to improve the antimicrobial treatments with nanoparticles, the investigations of the nanoparticle spatial distribution within the microbial cells are of particular importance for understanding their antimicrobial activity.

Antimicrobial nanostructures that can absorb and emit light in the UV region were prepared by functionalization of silver nanoparticles with tryptophan amino acid. The UV fluorescence emission property of AgTrp conjugates provided the detection of the nanostructures within microbial cells by the DUV fluorescence imaging technique with high spatial resolution (one pixel ~ 150 nm). Since the fluorescence of tryptophan depends on the polarity of the environment [1] the luminescence of in this way prepared tryptophan capped silver nanoparticles is environmentally sensitive. This feature enabled us to distinguish whether functionalized antimicrobial nanostructures were localized in hydrophobic (e.g. cell wall) or hydrophilic (cell interior and/or exterior) regions of the cells.

The results presented in section IV.1 of this dissertation are focused on the interaction of tryptophan functionalized silver nanoparticles with *Escherichia coli* and *Candida albicans* cells, and on the intracellular accumulation of the particles within the microorganism. The internalization of the AgTrp nanostructures by microbial cells was studied in the [327–353 nm], [370–410 nm], and [452–486 nm] wavelength ranges at DISCO beamline of synchrotron SOLEIL. Using a monochromatic synchrotron beam as an excitation source allowed detection of low concentrations of molecules emitting in the UV domain with high signal-to-noise ratio [15, 16].

IV.1.1. Structure and optical properties of tryptophan functionalized silver nanoparticles

Silver hydrocolloids (Ag NP) and hydrocolloids of tryptophan-functionalized silver nanoparticles (AgTrp) were synthesized by chemical reduction of silver salt (AgNO_3) by using NaBH_4 (details are given in section III.1.1). Functionalization was carried out by adding appropriate amount of tryptophan to silver hydrocolloid, and two concentrations of AgTrp sample was obtained, noted as AgTrp1.0 and AgTrp2.0.

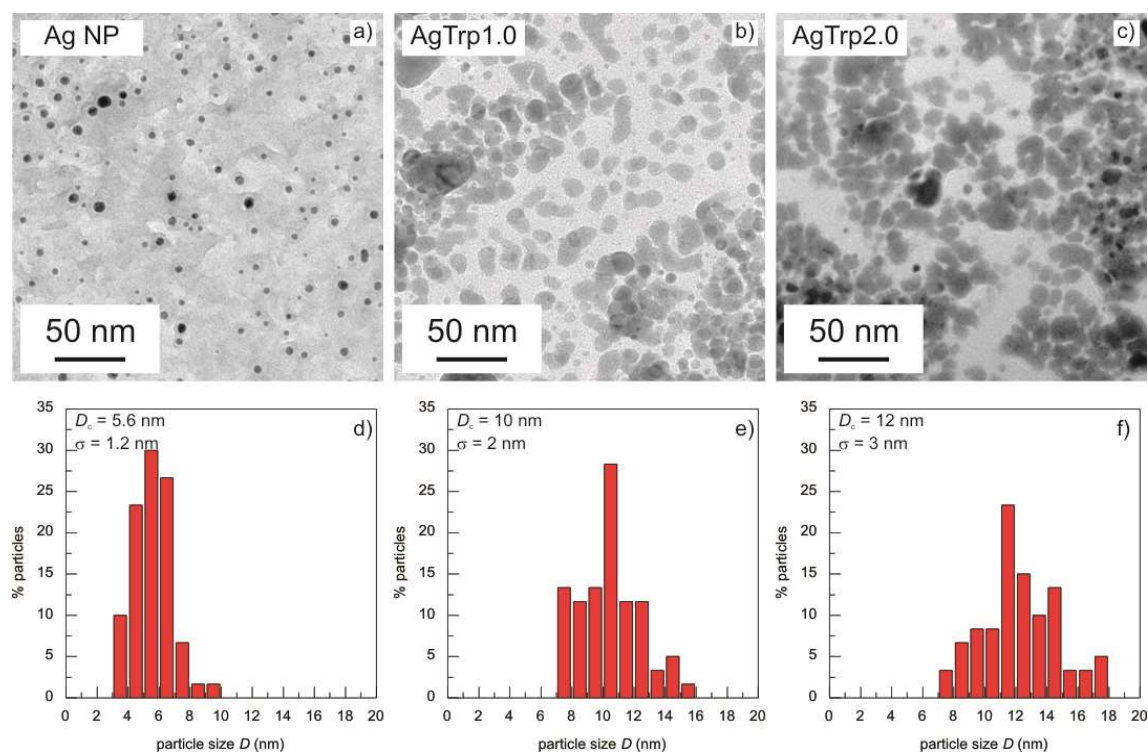


Figure IV.1.1. TEM images (a, b, c) and the corresponding particle size distribution (d, e, f) of AgNP, AgTrp1.0 and AgTrp2.0 samples.

The morphology and the size of tryptophan functionalized silver nanoparticles were investigated by transmission electron microscopy. The typical TEM images of the prepared samples are presented in Figure IV.1.1. The micrograph and the corresponding particle size distribution histogram of the initial silver colloid (Figure IV.1.1a and d) showed spherical particles approximately 6 nm in size with narrow size distribution. The addition of tryptophan led to the formation of hybrid nanostructures of larger sizes and more pronounced eccentricity (Figure IV.1.1b and c). As a consequence, there was also a broadening of the size distribution of the particles with respect to the size distribution for the initial Ag colloid. The average

values of the diameter of the equivalent circular area of the particles in AgTrp1.0 and AgTrp2.0 colloids were 10 nm and 12 nm, respectively. Observed changes in the size and morphology are a consequence of the tryptophan-mediated aggregation of noble metal nanoparticles, which was already reported for a silver nanoparticle–tryptophan system [17].

The absorption spectra of the silver colloids are presented in Figure IV.1.2a, along with the spectrum of 0.1 mM aqueous solution of the amino acid. The band at approximately 280 nm belongs to π - π^* transition of L-tryptophan, which are localized around the indole group. The UV-vis absorption spectrum of the initial AgNP colloid shows the absorption band at 382 nm that corresponds to the dipolar component of the surface plasmon resonance (SPR). The addition of tryptophan to the silver colloid leads to a redshift of the SPR band and to a decrease in its intensity. In addition, the surface modification induces asymmetric broadening of the band toward higher wavelengths that, for higher concentrations of the amino acid, results in the appearance of a new absorption band at approximately 580 nm. A red-shifted band is associated with aggregated AgNPs. The changes in the absorption spectra with the addition of tryptophan can be attributed to the changes in the morphology of Ag NPs in the presence of the amino acid depicted in Figure IV.1.1.

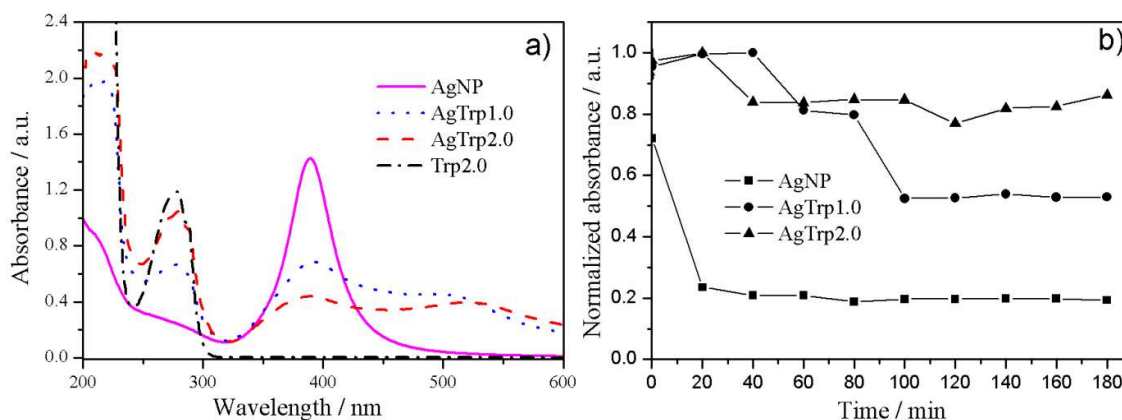


Figure IV.1.2. a) Absorption spectra of the tryptophan water solution (Trp2.0), hydrocolloids of silver nanoparticles (Ag NPs) and hydrocolloids of tryptophan-functionalized silver nanoparticles (AgTrp1.0 and AgTrp2.0). b) The stability of Ag NPs and AgTrp1.0 and AgTrp2.0 colloids in saline solution. The stability was estimated by following the changes in the intensity of absorption at $\lambda_{\max} = 398$ nm with time.

Since the saline solution was used as a dispersion medium for microbial cells it was important to test the chemical stability of tryptophan functionalized Ag NPs in this environment. Silver tends to form non-biocompatible complexes with chlorine and a decrease in the intensity of the SPR absorption band can be used as a measure of the stability of the nanoparticles [18].

Ag NPs, AgTrp1.0 and AgTrp2.0 hydrocolloids were mixed with saline at 37°C and the intensity of the absorbance at ~398 nm was monitored for 3 h. The relative changes in the optical absorption of Ag NPs, AgTrp1.0 and AgTrp2.0 samples in saline with time were shown in Figure IV.1.2b. It can be seen that the bare silver nanoparticles (Ag NPs) are highly unstable in the presence of saline. The intensity of the absorption band at prolonged times dropped by almost 80%. Concerning the functionalized nanoparticles (AgTrp1.0 and AgTrp2.0), the complexation of silver is present but less pronounced. In the case of the AgTrp2.0 sample the intensity of the SPR band was reduced by 10% only, meaning that the tryptophan prevents the complexation of silver with chlorine to a certain extent and, consequently, improves the stability of the nanoparticles in the saline solution.

The interaction between tryptophan and silver nanostructures was investigated with FTIR and XPS. Reported FTIR spectra of pure tryptophan and AgTrp powders dispersed in KBr in the 2000–500 cm^{-1} range are shown in Figure IV.1.3 [44]. The spectrum of the pure amino acid shows the bands that originate from the vibrations of carboxyl (1666 cm^{-1} and 1415 cm^{-1}) and α -amine (1590 cm^{-1} , 1457 cm^{-1} , and 1006 cm^{-1}) groups from the peptide group of tryptophan, as well as the bands assigned to pyrrole (3405 cm^{-1} , 1357 cm^{-1} , 1099 cm^{-1} , 1006 cm^{-1} , and 848 cm^{-1}) and benzene (3039 cm^{-1} , 1357 cm^{-1} , 1230 cm^{-1} , 987 cm^{-1} , 848 cm^{-1} , and 744 cm^{-1}) rings from the indole side group (Table IV.1.1). It can be seen that the presence of the nanoparticles significantly affects the vibration spectrum of the amino acid.

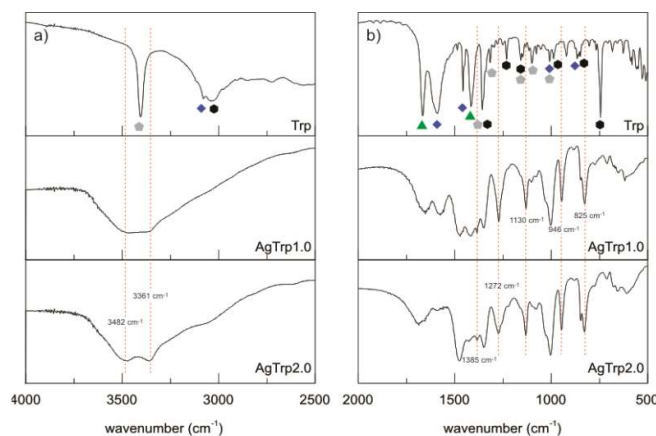


Figure IV.1.3. FTIR spectra of tryptophan and tryptophan functionalized silver nanoparticles. The symbols designate vibration modes pertaining to carboxyl (triangle), α -amine (diamond), pyrrole (pentagon) and benzene (hexagon). Adapted from [44]

Table IV.1.1. Characteristic vibration modes in the FTIR spectra of KBr dispersed Trp and AgTrp powders.

Tryptophan [cm ⁻¹]	AgTrp1.0 [cm ⁻¹]	AgTrp2.0 [cm ⁻¹]	Mode ^a
*	*	3482	$\nu_{as}NH_3^+$, νOH
3405	*	*	$\nu NH(r)$
*	3361	3361	$\nu_s NH_3^+$
3077	*	*	$\nu_{as} NH_3^+$
3039	*	*	$\nu CH(R)$
1666	1647	1687	$\nu_{as} COO^-$
1590	1575	1590	$\beta_{as} NH_3^+$
1457	1471	1475	$\beta_s NH_3^+$
1415	1417	1427	$\nu_s COO^-$
*	1384	1384	$\nu_s COO^-$
1357	1349	1347	βCH
*	1272	1272	νR
1230	*	*	βCH_2 , νR
*	1130	1130	$\nu H(R)$
1099	1099	1099	$\beta H(r)$
1006	1002	1002	$\nu CN(r)$, βNH_3^+
987	998	998	def. R
*	946	946	$\beta H(R)$
919	*	*	βCH_2
865	*	*	$\beta H(r)$
848	*	*	def R, def r
*	825	825	βCOO^-
744	*	*	$\beta H(R)$

v – stretching; β – bending; def. – deformational mode; s – symmetric deformation; as – asymmetric deformation; R – benzene ring; r – pyrrole ring; * – mode not observed. ^aBand assignments were taken from X.Cao and G. Fischer, J. Phys. Chem. A **103**, 9995 (1999)

The most indicative changes are in the 1500–1300 cm⁻¹ regions that depend also on the Ag:Trp molar ratio. With an increase in the amount of Trp, the relative intensity of the 1415 cm⁻¹ line, that corresponds to a symmetric stretching of the carboxyl ion, decreases with respect to the bands at 1457 cm⁻¹ ($\beta_s NH_3^+$) and 1357 cm⁻¹ (βCH of indole). This result can be correlated to the observed aggregation of the nanoparticles upon addition of tryptophan. The FTIR bands pertaining to α -amine and indole groups also differ in the spectra of the amino acid and the AgTrp samples. The lines at 3405 cm⁻¹ ($\nu NH(r)$, indole) and 744 cm⁻¹ ($\beta H(R)$, benzene ring) almost disappear upon the functionalization, indicating that silver–tryptophan interaction takes place via secondary amines of pyrrole and delocalized π -orbitals of benzene. In the case of the vibrations attributed to the deformations of α -amine, the bands shift toward lower wavenumbers and decrease in the intensity with an increase in the Ag:Trp molar ratio. The vibration spectra of AgTrp show additional lines that were not observed in the spectrum of the pure amino acid (dotted lines in Figure IV.1.3). New bands at 3482 cm⁻¹ and 3361 cm⁻¹ can be attributed to the stretching vibrations of protonated α -amine, while the lines at 1385 cm⁻¹ and 825 cm⁻¹ correspond to stretching and deformation vibrations of the carboxyl group.

The bands positioned at 1272 cm^{-1} , 1130 cm^{-1} , and 946 cm^{-1} represent new modes originating from the indole group. The presented analysis of the FTIR spectra shows that tryptophan molecules interact with silver nanoparticles via all available functional groups.

The X-ray photoelectron spectroscopy scan of the Ag 3d core level of AgTrp nanostructures (sample AgTrp1.0) is presented in Figure IV.1.5. Generally, the 3d level of silver is characterized by two spectral lines separated by 6 eV that correspond to $3d_{3/2}$ and $3d_{5/2}$ levels. It can be seen that in the case of functionalized nanostructures, each of these lines is a result of the superposition of two additional peaks. In the Ag $3d_{5/2}$ profile, the positions of these peaks are 368.8 eV and 367.6 eV. The first maximum is shifted by approximately 0.5 eV towards higher energies with respect to the reference value of bulk metallic silver of 368.3 eV [19] (Ag0, vertical dotted line in Figure IV.1.4). Shin et al. [20] showed that the shift of this type is a consequence of cumulative effects of the increase in the number of surface atoms in the particles due to their small size and the adsorption of a thin organic layer on the silver surface. The result indicates that functionalization results in the formation of amino acid layers on the nanoparticle surface with a thickness sufficient to induce a shift in the Ag $3d_{5/2}$ level. On the other hand, the peak at lower energy corresponds to silver in the oxidized state Ag^+ [20].

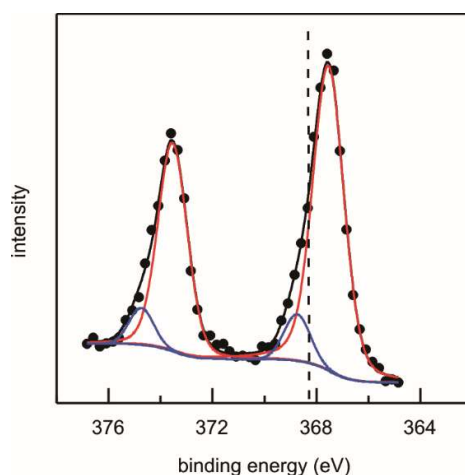


Figure IV.1.4. High resolution X-ray photoelectron spectra of Ag 3d levels of the AgTrp1.0 sample. The vertical dashed line corresponds to the reference value of bulk silver [19].

Photoluminescence emission spectra of tryptophan aqueous solutions (0.1 mM, pH \sim 10) and AgTrp colloids are presented in Figure IV.1.5a and Figure IV.1.6a. The spectra show an asymmetric emission band at 368 nm that originates from the environment sensitive $^1\text{L}_a$ transitions of the amino acid. The intensity of the emission band of the AgTrp1.0 sample

is lower than that of the pure 0.1 mM tryptophan solution, although the concentrations of the amino acid in the both samples are the same (Figure IV.1.5a). This can be attributed to the absorption of the emitted radiation by silver nanoparticles (Figure IV.1.2a) and/or to the increase in the non-radiative decay rate of the surface-bound tryptophan [21].

Hydrophobic indole side group of tryptophan allows a transfer of hybrid nanostructures from the hydrocolloid into an organic solvent, such as toluene. In general, fluorophores in polar solvent, such as water, display large Stokes' shifts due to interactions of the excited state dipole moment of the fluorophore with the surrounding polar solvent molecules [1]. In the non-polar solvent, on the other hand, these interactions are less pronounced and result in PL bands at higher energies. The photoluminescence spectra of the initial and the phase transferred AgTrp2.0 colloids are presented in Figure IV.1.5b ($\lambda_{\text{exc}} = 280$ nm) and Figure IV.1.6b ($\lambda_{\text{exc}} = 290$ nm). It can be seen that the nanostructures dispersed in toluene exhibit an emission band at lower wavelengths, which is typical of tryptophan luminescence in nonpolar media. This suggests that the functionalization of silver nanoparticles with tryptophan results in fabrication of polarity-sensitive fluorophore that, as it will be seen in the following section, enabled us to gain additional information on the accumulation of the AgTrp nanostructures with respect to *E. coli* and *C. albicans* cells. The same excitation of $\lambda_{\text{exc}} = 280$ nm (as noted in the Figure IV.1.5) was used in fluorescence imaging of *E. coli* cells. Fluorescence emission was collected in two emission ranges: F1 = (327 – 353) nm and F2 = (452 – 486) nm.

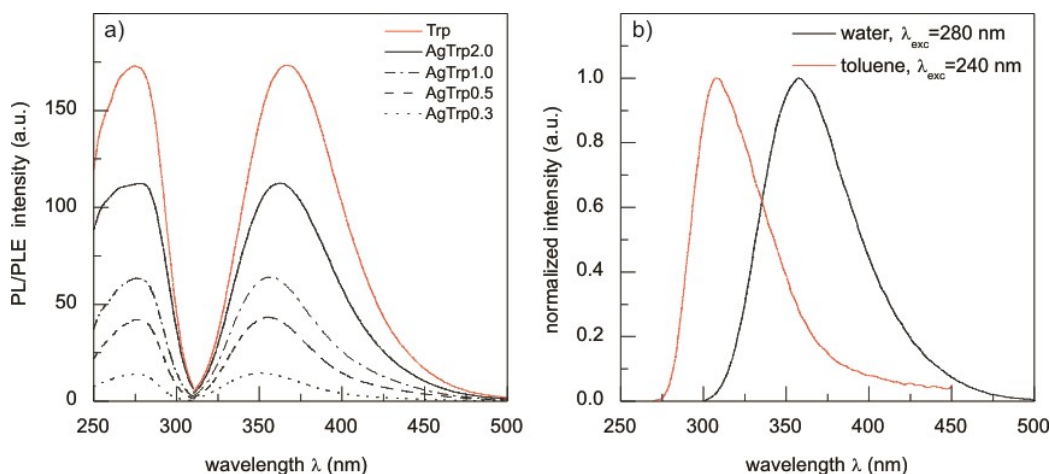


Figure IV.1.5. a) Photoluminescence emission ($\lambda_{\text{exc}} = 280$ nm) and excitation ($\lambda_{\text{em}} = 360$ nm) spectra of 0.1 mM Trp aqueous solution (red line) and AgTrp colloids. b) Normalized photoluminescence spectra of AgTrp2.0 colloids in water (black line) and toluene (red line).

For the fluorescence imaging experiments on *C. albicans*, the excitation wavelength of 290 nm was used, according to the photoluminescence spectra in Figure IV.1.6a. The fluorescence signal was collected in F1 = (327 – 353) nm and F2 = (370 - 410) nm emission ranges to detect AgTrp nanostructures in hydrophilic and hydrophobic environment of the cells.

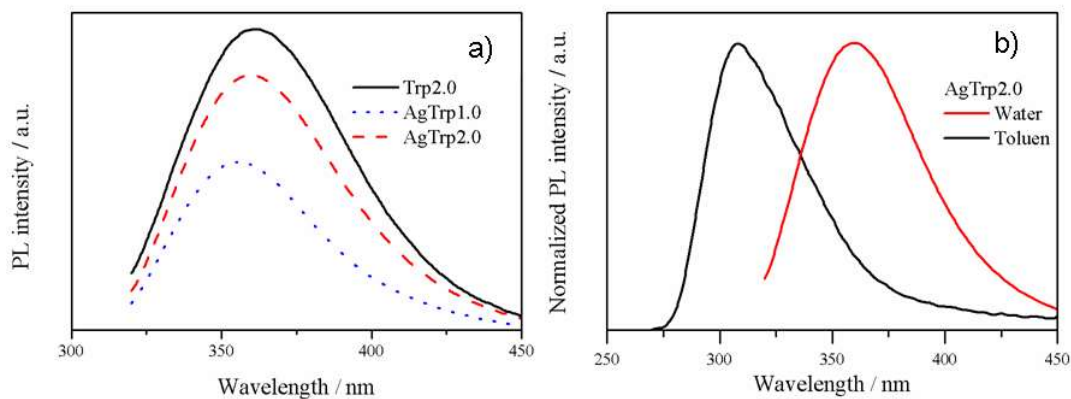


Figure IV.1.6. a) Photoluminescence emission ($\lambda_{\text{exc}} = 290$ nm) spectra of tryptophan aqueous solution and AgTrp hydrocolloids. b) Normalized photoluminescence spectra of AgTrp2.0 colloids in toluene ($\lambda_{\text{exc}} = 240$ nm) and water ($\lambda_{\text{exc}} = 290$ nm).

IV.1.2. DUV fluorescence imaging of *Escherichia coli* incubated with tryptophan functionalized silver nanoparticles

E. coli is a rod-shaped (approximately 0.5 μm by 2 μm) Gram-negative bacterium which possesses a complex cell envelope consisting of an outer membrane – a lipid bilayer composed of lipopolysaccharides and phospholipids, an aqueous and protein rich periplasm, a peptidoglycan cell wall, and an inner cytoplasmic membrane, which is a phospholipid bilayer [22]. The interactions between the silver nanoparticles and Gram-negative bacteria were extensively studied by electron microscopy techniques [5, 8, 23–25]. The investigations of this type state that the nanoparticles attach to the cell surface. In addition, the observations of thin cross-sections of *E. coli* cells incubated with silver nanoparticles [5, 8] showed that the particles can penetrate the microorganism. The conjugation of AgNPs with tryptophan can offer other advantages in addition to providing specific optical properties. For example, *E. coli* produces membrane transport proteins that transport tryptophan into cells [26, 27] and therefore the functionalization of the nanoparticles with the amino acid can facilitate the diffusion of the nanoparticles into the cells. Also, a recent study [28] showed that tryptophan residues in designed antimicrobial peptides penetrate cell membranes and improve their antimicrobial activity.

To find the optimal concentration for the bioimaging experiments, the antimicrobial activity of AgTrp nanostructures versus *E. coli* was tested using the procedure described in section III.2.2. It is important to note that according to the procedure, the incubation of the cells with the nanoparticulate agents takes place for 24 h at 37 °C so that the cells can achieve stationary phase of growth. The results are presented in Table IV.1.2. The data indicate progressive decrease in the cell count with an increase in the silver concentration. The results, also, show that the presence of tryptophan reduces antimicrobial efficacy of silver, since with an increase in the molar content of the amino acid the percent of inhibition relative to the control decreases. The total inhibition of the microbial growth occurs when the concentration of silver exceeds 2.16 $\mu\text{g ml}^{-1}$, both for pristine and tryptophan conjugated nanoparticles. Bearing in mind that we wanted to image *E. coli* in the growth phase that is after incubation of the cells with the nanoparticles for just 2h, for the preparation of the samples we used higher concentration of 8.64 $\mu\text{g ml}^{-1}$, so that a probability of interaction of AgTrp with cells would be higher. Although this high concentration would have eventually induced complete inhibition of bacterial growth, the experiments were performed immediately after 2h of incubation while a significant number of the bacteria were still alive (Figure III.2.1).

Table IV.1.2. Results of antimicrobial activity of functionalized silver nanoparticles vs. *E. coli*

	Concentration of silver							
	0.54 $\mu\text{g/ml}$		1.08 $\mu\text{g/ml}$		1.62 $\mu\text{g/ml}$		2.16 $\mu\text{g/ml}$	
	CFU/ml	R[%]	CFU/ml	R[%]	CFU/ml	R[%]	CFU/ml	R[%]
Ag NP	$30 \times 10^4 \pm 3 \times 10^4$	50.81 ^a	$14 \times 10^4 \pm 5 \times 10^4$	77.00 ^a	136.00 \pm 25	99.99 ^a	0	100.00
AgTrp1.0	$44 \times 10^4 \pm 6 \times 10^4$	27.86 ^b	$23 \times 10^4 \pm 4 \times 10^4$	62.29 ^b	1016.00 \pm 98	98.85 ^b	0	100.00
AgTrp2.0	$60 \times 10^4 \pm 2 \times 10^4$	0.20 ^c	$52 \times 10^4 \pm 3 \times 10^4$	14.75 ^c	2900.00 \pm 112	96.82 ^c	0	100.00

$61 \times 10^4 \pm 5 \times 10^4$ CFU/ml of control *E. coli* sample;
 Values marked by a different letter (a, b, and c) within a particular column are significantly different (P = 0.1)

The DUV fluorescence imaging of live *E. coli* and *E. coli* cells incubated with different concentrations of AgTrp colloids was performed using a 280 nm synchrotron beam as an excitation source. The results of the DUV fluorescent imaging of live *E. coli* cells for two different emission detection ranges (Filter I: [327 - 353 nm] (red) and Filter II: [452 - 486 nm] (green)) are presented in Figure IV.1.6a, together with the bright-field images of the samples. The intensities of the fluorescent signals, averaged over different locations in the sample, are shown in Figure IV.1.7b. In the [327-353 nm] emission range, the autofluorescence of the cells is of lower intensity than the UV fluorescence of *E. coli* incubated with AgTrp nanostructures. This effect is particularly visible in the case of the microorganisms treated with AgTrp2.0 colloid, where the intensity of the signal was approximately four times higher than the signal of the control.

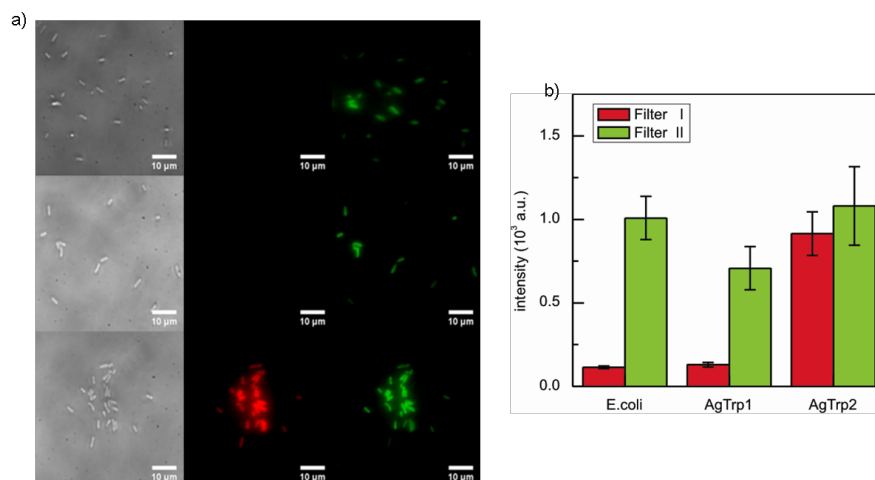


Figure IV.1.7. a) Bright field and fluorescence images of *E. coli* cells (top) and *E. coli* cells incubated with AgTrp1.0 (middle) and AgTrp2.0 (bottom) nanoparticles. b) The intensities of fluorescence signals averaged over different locations in the samples. Conditions $\lambda_{\text{exc}}=280$ nm, $t=6$ min, Filter I: 327 – 353 nm (red), Filter II: 452 – 486 nm (green).

The average intensities of the fluorescent signals for *E. coli* cells incubated with AgTrp1.0 and AgTrp2.0 functionalized nanoparticles obtained in [452–486 nm] range showed a negligible difference in comparison to the control sample, indicating that they originate from the autofluorescence of the cells (Figure IV.1.6b). The difference between fluorescent images obtained using described conditions provides that the UV luminescence pertaining to AgTrp nanostructures can be easily distinguished from that of *E. coli* autofluorescence.

The mentioned effect is demonstrated in FigureV.1.8 that shows the overlays of the fluorescence images acquired within [327–353 nm] and [452–486 nm] (FigureV.1.8a and b), as well as [327–353 nm] and [370–410 nm] (FigureV.1.8c and d), detection ranges. It can be seen that the strong signal in the [327–353 nm] domain can be detected only in the *E. coli* cells incubated with AgTrp2.0 colloid (Figure IV.1.8b and d).

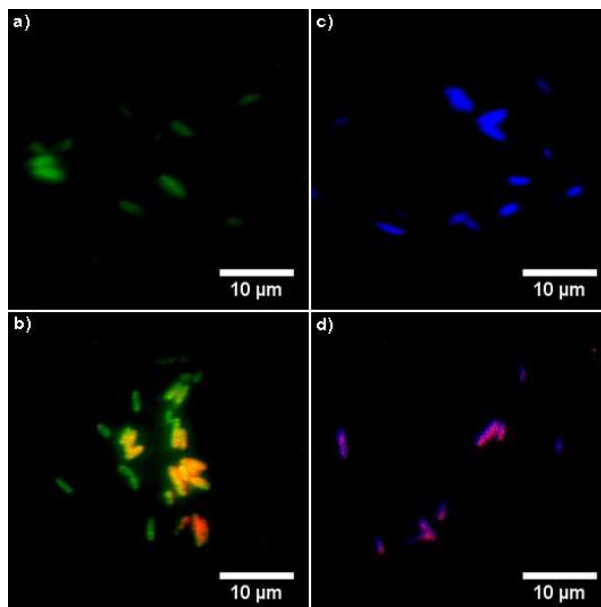


Figure IV.1.8 Overlaid fluorescence images of (a, c) *E. coli* cells and (b, d) *E. coli* cells incubated with AgTrp2.0. The images were obtained by overlaying the data acquired within [327–353 nm] and [452–486 nm] (a, b), as well as [327–353 nm] and [370–410 nm] (c, d) ranges. Excitation wavelength $\lambda_{\text{exc}} = 280$ nm.

The tryptophan fluorescence, as well as that of phenylalanine and tyrosine, is responsible for the characteristic optical properties of many proteins [1] including those of *E. coli*. However, the complexity of the biomolecule results in limited number of tryptophan residues per protein. For example, the most abundant outer membrane protein in *E. coli*, OmpA, with approximately 105 copies per *E. coli* cell [29], has five tryptophan residues, out of which four are located in the lipid bilayer [30] resulting in the overall fluorescence of the

protein peaking at about 330 nm [31]. In our case, an intense signal from the functionalized nanostructures is a consequence of the accumulation of the amino acid on the silver surface, as was concluded from the analyses of the XPS data (Figure IV.1.5). The fact that the fluorescence from AgTrp nanostructures in the cells occurs at lower wavelengths than the emission of the hydrocolloids (368 nm) indicates that the functionalized nanostructures were localized in a hydrophobic environment (i.e. cell membrane). This conclusion is in agreement with the results presented in Figure IV.1.6b and with the recent results on the interaction of tryptophan-substituted antimicrobial peptides with liposomes that mimic *E. coli* cell membranes [27]. In the mentioned study the observed blue-shift in the tryptophan emission was attributed to the insertion of tryptophan residues into the lipid bilayers. The change in the morphology of the bilayer structure after the interaction between silver nanoparticles and vesicles prepared from extracted *E. coli* membranes was also confirmed by TEM analysis [24].

For the imaging conditions used in the present study, the spatial resolution of the fluorescence images is defined by the projected pixel size of 154 nm. The estimated lateral resolution for the [327–353 nm] emission range is around 140 nm, which is lower than the pixel size of the images. Under the assumption that there is a correlation between the intensity of the signal at a given pixel and the concentration of AgTrp nanostructures in the corresponding surface area, this spatial resolution is sufficient to determine the preferable locations for the accumulation of AgTrp nanostructures in the bacteria. Bright-field and the corresponding fluorescence images of *E. coli* cells incubated with AgTrp2.0 colloid acquired in the [327–353 nm] emission range are presented in Figure IV.1.9. The intensity of the luminescence signal localized on the cell positions varies along the cell surface area (Figure IV.1.9b) suggesting inhomogeneous distribution of AgTrp nanostructures. The white dots in Figure IV.1.9c represent positions of local fluorescence maxima detected using Fiji. For clarity of the presentation, labels were augmented to 9×9 pixels. The individual maximum can be attributed to the preferential location within the cell in which accumulation of AgTrp nanostructures takes place.

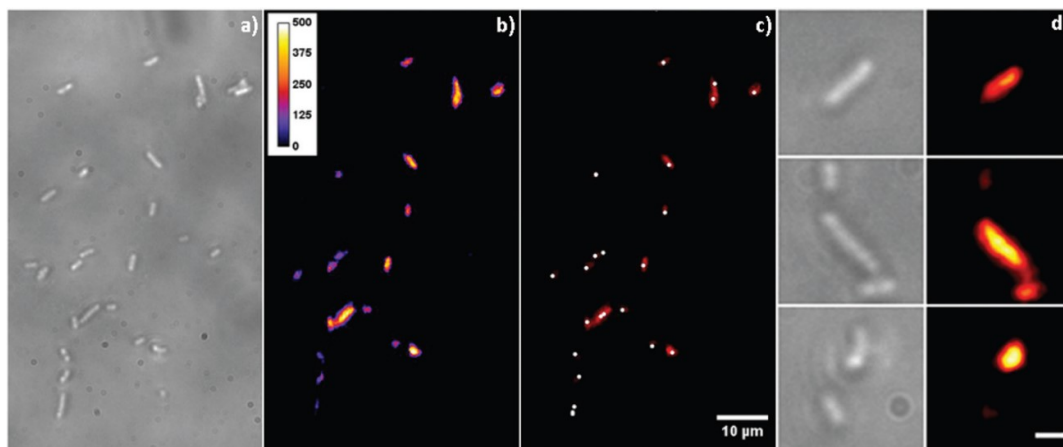


Figure IV.1.9. (a) Bright-field and (b) fluorescence images of *E. coli* cells incubated with AgTrp2.0 colloid (concentration $8.64 \mu\text{g ml}^{-1}$) obtained in the [327–353 nm] range. (c) The same image with local fluorescence maxima labeled by 9×9 pixel white dots. (d) Bright-field and fluorescence images of selected cells (scale bars in the images correspond to $2 \mu\text{m}$). Conditions: $\lambda_{\text{exc}} = 280 \text{ nm}$, acquisition time 6 min, incubation time 2 h. Pixel size in the images is equal to 154 nm

Therefore, our DUV experiments show that functionalization with tryptophan enables study of the accumulation of nanoparticles with a single cell resolution (Figure IV.1.10). The results of the fluorescence imaging suggest that *E. coli* cells internalize AgTrp nanostructures. This can be seen more clearly in Figure IV.1.10d in which bright field and spatially averaged fluorescence images (mean filter in Fiji) of selected *E. coli* cells incubated with AgTrp2.0 are presented. The spatial distribution of the nanostructures within the cells observed agrees with transmission electron microscopy observations of the cross-sections of *E. coli* incubated with silver nanoparticles [5, 8]. The DUV results in Figure IV.1.9 and 10 suggest that tryptophan-functionalized silver nanoparticles interact with the sections of cell membranes leading to encapsulation of the nanostructures by the phospholipids and subsequent transport to the cytoplasm.

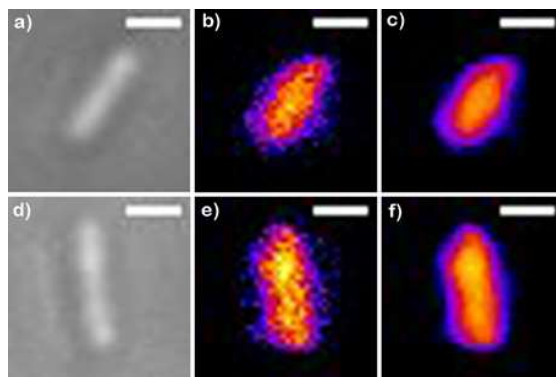


Figure IV.1.10. Bright-field and fluorescence images of individual *E. coli* cell incubated with AgTrp1.0 (a,b,c) and AgTrp2.0 (d,e,f) colloids obtained in the [327 nm, 353 nm] range.

IV.1.3. DUV fluorescence imaging of *Candida albicans* incubated with tryptophan functionalized silver nanoparticles

The DUV fluorescence imaging studies of the pure *C. albicans* cells and *C. albicans* cells mixed with pure tryptophan solution (Trp2.0), Ag NPs colloid and AgTrp2.0 colloid were performed by using 290 nm synchrotron beam as an excitation source. Due to limited beamtime at SOLEIL facility, the studies were narrowed to a single *C. albicans* strain (ATCC 10259). The discussion of the results will be focused on the fluorescent signals obtained in [327–353 nm] (filter F1) and [370–410 nm] (filter F2) ranges. The signal collected in F1 range originates predominantly from the fluorescence of functionalized nanoparticles situated in non-polar environment, but a smaller part of the collected signal may also come from the fluorescence of the nanoparticles in water (low-wavelength tail in Figure IV.1.6). The signal collected in F2 range belongs to the fluorescence of the functionalized nanoparticles situated in polar environment (water).

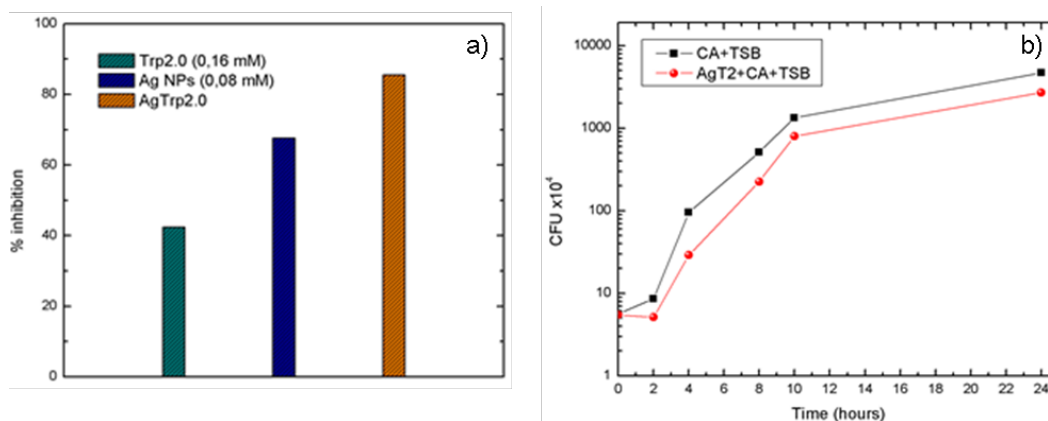


Figure IV.1.11. a) Antimicrobial activity of pure tryptophan (Trp2.0), bear silver nanoparticles (Ag NPs) and tryptophan functionalized silver nanoparticles (AgTrp2.0). b) Survival of *C. albicans* incubated with AgTrp2.0 nanostructures in TSB medium for 24 hours.

Prior to the discussion on the fluorescence imaging results, we will refer to the observations regarding the morphology of the untreated *C. albicans* and *C. albicans* after the incubation. The bright-field imaging of the untreated *C. albicans* sample showed the presence of diverse morphogenetic states of the fungus: single cells, small clusters of yeast cells, budding yeast forms and larger clusters of agglomerated yeast as well as pseudohyphae and hyphae, whereas the later forms were not found in the *C. albicans* samples incubated either with pure tryptophan or Ag NPs. We have correlated this observation with the antimicrobial activity

tests, which showed that the number of *C. albicans* colonies in the samples with tryptophan and Ag NPs were significantly reduced (Figure IV.1.11a). It is worth to notice that the antifungal activity of AgTrp was more pronounced than that of Ag NP, which is the opposite to the case of *E. coli*. Since no mature morphogenetic forms were found in the above-mentioned control samples, we compared the fluorescence signals arising from single yeast cells and small clusters of single cells. Figure IV.1.12 shows the bright-field and the fluorescence images of the pure *C. albicans* cells and the cells incubated with tryptophan and bare Ag NPs. In order to enable visual comparison of the fluorescence intensities from different images, the fluorescence signals in the corresponding channels were scaled to the same range of values using Fiji image analysis software. The untreated cells (Figure IV.1.12a) exhibit autofluorescence in both spectral ranges, [327–353 nm] (filter F1) and [370–410 nm] (filter F2). The autofluorescence originates from the presence of the fluorophores in the cells such as phenylalanine, tryptophan and dityrosine [32, 33]. Figure IV.1.12b and c show the fluorescence images of the cells after the incubation with tryptophan and Ag NPs. With respect to the intensity of the autofluorescence of the control sample, no significant changes in fluorescence were observed after the incubation. Statistical analysis was performed on the results obtained from at least 10 different locations along the sample and it confirmed that the variations in the intensity of the fluorescent signal were within the experimental error. Tryptophan and Ag NPs obviously affect the filamentation and growth [34, 35], but do not affect the fluorescence properties of the cells.

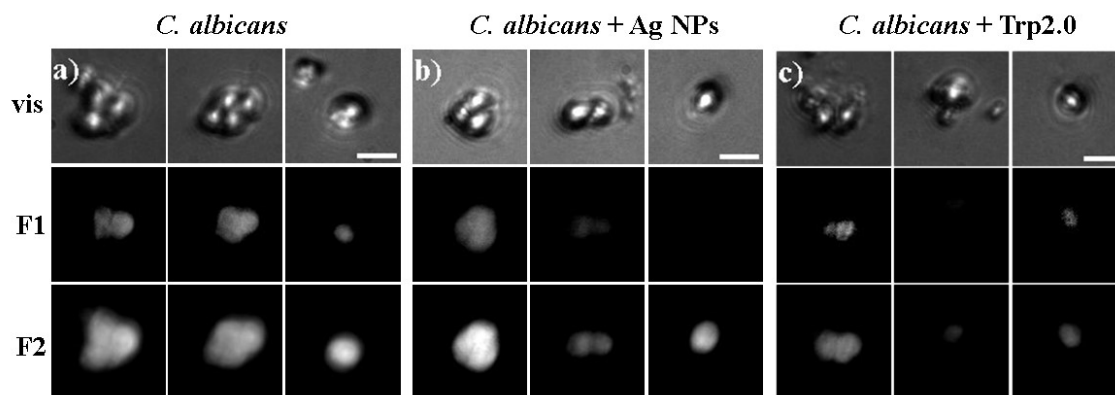


Figure IV.1.12. Bright-field (vis) and fluorescence images of *C. albicans* single cells and small clusters of cells recorded in two emission ranges F1 [327–353 nm] and F2 [370–410 nm]: a) *C. albicans*, b) *C. albicans* incubated with bare Ag NPs and c) *C. albicans* incubated with Trp2.0. Scale bar is 5 μm . For comparison, the fluorescence signals in corresponding F1 and F2 channels were scaled to the same range of values using Fiji image analysis software.

In contrast to these observations, the pseudohyphae and large clusters of agglomerated yeast were observed in the case of *C. albicans* cells treated with the tryptophan functionalized silver nanoparticles. Although the antifungal activity of the AgTrp2.0 colloid was more pronounced than that of the pure tryptophan and bare silver nanoparticles (Figure IV.1.11a), the similarity between the growth curves of the sample and control (Figure IV.1.11b) indicated that the treated cells reach the phase of stationary growth. This is probably the consequence of a lower diffusivity of functionalized nanoparticles, since they are larger in size than the starting Ag NP.

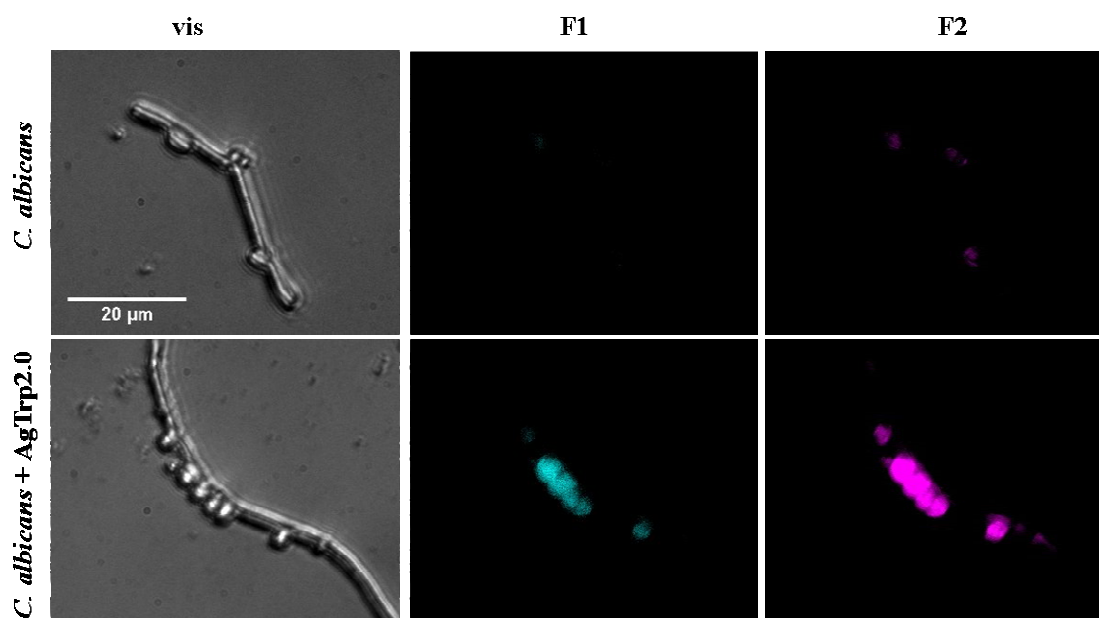


Figure IV.1.13. Bright-field (vis) and fluorescence images of pseudohyphae with budding spores in early stage of growth of the control *C. albicans* and *C. albicans* + AgTrp2.0 samples. The fluorescence images were obtained upon 290 nm synchrotron beam excitation, while the fluorescent signal was collected for 30 s in the [327–353 nm] (F1) and [370–410 nm](F2) wavelength range. The fluorescence signals in corresponding F1 and F2 channels were scaled to the same range of values using Fiji image analysis software.

In Figure IV.1.13, we show the fluorescent images of the pseudohyphae with budding spores in early stage of growth for the control *C. albicans* sample and the sample obtained after incubation of *C. albicans* with AgTrp2.0 nanoparticles (*C. albicans* + AgTrp2.0). It can be seen that the sample incubated with AgTrp2.0 nanostructures exhibits much stronger fluorescence than the control sample in both spectral ranges (F1 and F2). The intensity of the fluorescence signal increased almost three times proving that the tryptophan functionalized silver nanoparticles interacted with the cells. Specifically, there is a preferential interaction of

AgTrp2.0 nanoparticles with the spores, rather than with the elongated parts of pseudohyphae. This effect was observed at various locations along the sample and the additional fluorescent images are presented in Figure IV.1.14.

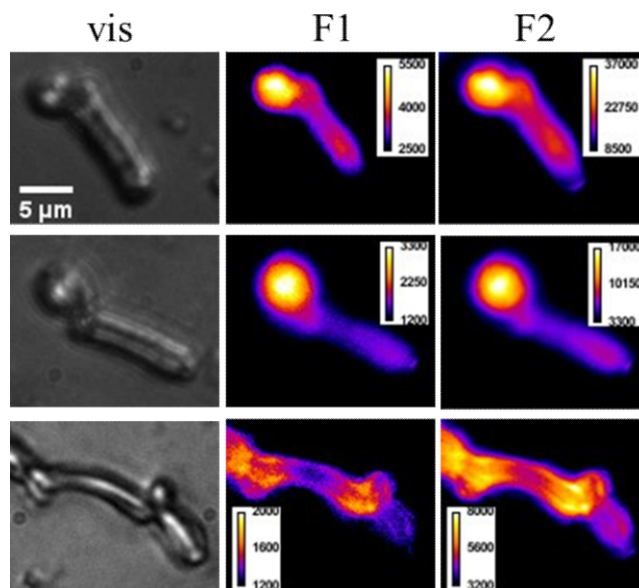


Figure IV.1.14. Bright-field (vis) and fluorescence images of pseudohyphae with budding spores in early stage of growth of the *C. albicans*+AgTrp2.0 sample. The fluorescence images were obtained upon 290 nm synchrotron beam excitation, while the fluorescent signal was collected for 30 s in the [327 - 353 nm] (F1) and [370 - 410 nm] (F2) wavelength range. The minimum of the intensity is assigned to the black color and the maximum is assigned to the white color.

This result agrees with previous studies that showed that the morphogenetic forms in early stages of growth are less resistant to antifungal agents [36, 37]. The fluorescence images in Figure IV.1.13 suggest that the incubation with AgTrp2.0 nanoparticles results in significant increase in fluorescence intensity in both spectral ranges (F1 and F2). In Figure V.1.15, we show that this is also the case with the other morphogenetic forms of *C. albicans* such as the yeast and early biofilm phases. It can be seen in Figure IV.1.15a-c that the yeast and early biofilm forms incubated with AgTrp2.0 nanoparticles exhibit more pronounced fluorescence than that of the control sample. The fluorescence signals in corresponding F1 and F2 channels were scaled to the same range of values using Fiji image analysis software. In Figure IV.1.15d, we compare the mean fluorescence intensities per single cell calculated from at least ten different locations along the samples. It can be noticed that the mean fluorescence intensity in both spectral ranges increased by almost two times after the incubation. The obtained results clearly show that AgTrp2.0 nanoparticles affect the fluorescent properties of

the *C. albicans* after the incubation. However, the fact that the fluorescence intensity increases in each of the investigated spectral ranges suggests that the functionalized silver nanoparticles may reside in both hydrophilic (cell interior and/or exterior) and hydrophobic (cell wall) regions of the cells. The observed increase in the fluorescence signal intensity in both F1 and F2 spectral ranges in the *C. albicans* cells incubated with AgTrp2.0 nanoparticles (in comparison to the control sample) enabled us to draw the additional conclusions on the accumulation of the nanoparticles in the cells.

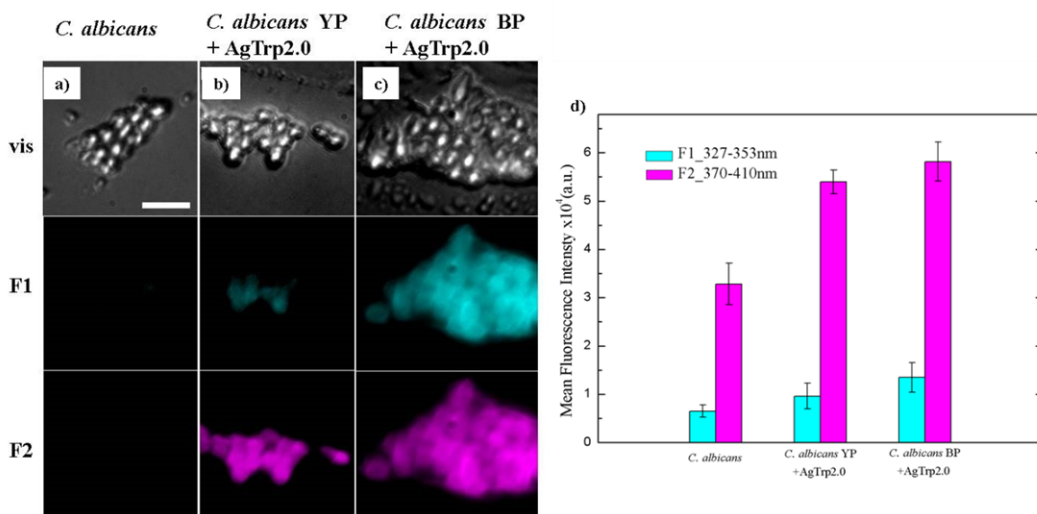


Figure IV.1.15. a) Bright-field and fluorescence images of a) control *C. albicans* cells b) AgTrp2.0 incubated *C. albicans* agglomerated yeast phase (YP) cells and c) AgTrp2.0 incubated *C. albicans* early biofilm phase (BP) cells. Scale bar is 10 μ m. The fluorescence images were obtained upon 290 nm synchrotron beam excitation, while the fluorescent signal was collected for 30 s in the [327–353 nm] (F1) and [370–410 nm] (F2) wavelength ranges. d) Statistics on mean fluorescent intensity per single cell for untreated (control) and incubated (yeast phase and biofilm phase) *C. albicans* samples (number of cells counted $n > 100$). The error bars represent standard deviations of the fluorescence intensity.

For this reason, we have performed time-lapse experiments and bleach kinetics analysis of the results. In the image sequences obtained in the time lapse experiment, we selected 50 local maxima of fluorescence in the ranges to represent the specific sites at which accumulation of the nanoparticles takes place. To determine the fluorescence maxima, a threshold is set at the maximum value minus noise signal and the analyses were carried out over the contiguous area around the maximum, which is above the threshold (the details of the procedure can be found in Experimental). It was observed that the fluorescence intensity values of the local maxima were significantly higher than the autofluorescence of the control sample. This approach was used instead of co-localization analysis due to heterogenic nature of *C. albicans*

autofluorescence as well as due to the problems in establishing well-defined crosstalk parameters. Figure IV.1.16 shows the dependence of the local fluorescence maxima values on time (the box plot diagrams) for the untreated and treated cells that constitute early biofilm phase. In the case of the control sample, the autofluorescence is decreasing with time in both spectral ranges (Figure IV.1.16a). The same is observed for the incubated cells (Figure IV.1.16b) but with more pronounced decay of the intensity of fluorescence signal over the same period.

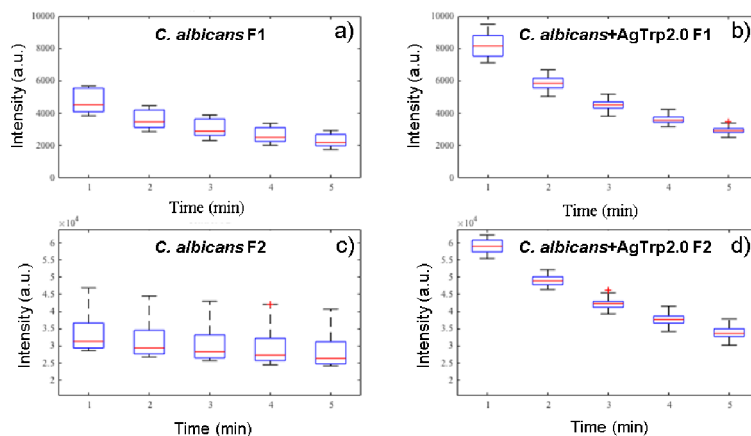


Figure IV.1.16. The box plot diagrams of the local fluorescence maxima values versus time for untreated (a, c) and incubated (b, d) cells in [327–353 nm] (F1) and [370–410 nm] (F2) spectral ranges. Red horizontal line represents the median intensity of the corresponding maxima.

Taking also into account that incubated cells show overall higher intensity of fluorescence signals, the results in Figure IV.1.16 suggests that they contain the fluorophores that exhibit different bleaching kinetics. The fluorescence intensity may exhibit time-dependent decrease due to photobleaching and it is reliant on the molecular structure and the local environment [1]. The presence of AgTrp nanostructures at cell sites could induce perturbation in bleaching dynamics of the fluorescent signal. To elucidate this effect further, we decided to study in detail the changes in the fluorescence intensity in both emission channels during the bleaching by analyzing the consecutive fluorescence images of the cells. Bleaching kinetics was analyzed by using a plugin PixBleach [38], developed for Fiji software. The intensities from the bleach stacks are fitted to Kohlrausch function $I(t) = A \times \exp(-t/\tau)^{1/h} + B$, a generalized exponential function with an additional stretching parameter [39–41]. A is the decay amplitude, B is a measure of the background autofluorescence, τ is the bleach time constant and h is the heterogeneity factor. The amplitude corresponded to initial fluorescence intensity (prior to bleaching). Bleach time constant is the parameter that characterizes the lifetime of

the fluorophore in the structure, while heterogeneity factor is related to the width of the τ - distribution values. The calculations are based on pixel by pixel analysis of the randomly distributed bleach rate constants, which is appropriate for heterogeneous fluorescence coming from structure such as early biofilm [40, 41]. Five selected images from the time lapse stack are presented in Figure IV.1.17a. To localize fast bleaching sites, we subtracted the last image in the stack from the first one, while assuming that the rapid bleaching was finished by the time the last image was acquired [38]. The images obtained by subtraction ($\Delta F1$ and $\Delta F2$) in Figure IV.1.17b depict different fast bleaching regions, especially in the highlighted sites (green outline) for which photobleaching analysis was applied. The amplitude maps calculated for the fluorescence signals obtained in F1 and F2 emission ranges are shown in Figure IV.1.16c. In the case of the first filter (F1), the most pronounced fluorescence bleaching is observed in the regions close to the cell interior. In contrast, the pronounced fluorescence bleaching in the second emission range (F2) was observed in the regions around the cells. Also, the time constant (τ) maps for F1 and F2 spectral ranges differ significantly (Figure IV.1.17c).

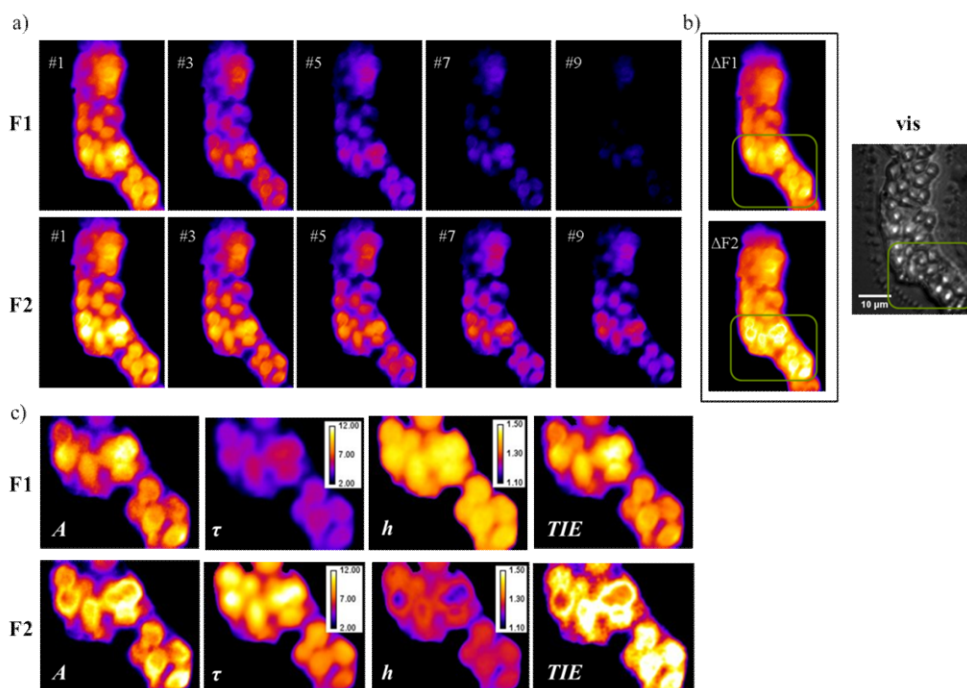


Figure IV.1.17. a) Five selected images of the AgTrp2.0 nanoparticles incubated cells obtained by time lapse imaging in [327–353 nm] (F1) and [370–410 nm] (F2) emission spectral ranges. b) The images ($\Delta F1$ and $\Delta F2$) obtained by subtraction of the last image in the stack from the first one in the specific spectral range and the VIS image of the cells. The analysis was carried out on the part of the image that depicted the most pronounced changes (green outline). c) Parameters from the stretch exponential fitting of the fluorescence intensity decay: A -amplitude map, τ -time constant map, h -heterogeneity map and TIE – Time integrated emission.

The τ -values in the F1 range are two times lower in average than that in F2 range, which indicates faster bleaching in the former spectral range. Heterogeneity maps in Figure IV.1.17c suggest that the τ -distribution is much broader in the F1 range, while the widths of distributions in both ranges are higher at the cell sites. Time-integrated emission maps (TIE) in Figure IV.1.17c depict corrected intensities for various factors such as illumination shading and autofluorescence. TIE removes spatial variations in probe emission due to fluorescence saturation or local collisional fluorophore quenching in living cells [38]. The resulted TIE map of pixels represents the total intensity emitted by the fluorophores. These results differ from the bleach time constant and heterogeneity maps calculated for the autofluorescence of the control sample (Figure IV.1.18). The presented maps show homogenous distribution of τ - and h -values with slight variations due to complex morphology of the early biofilm phase. Time constant values of the untreated cells in both spectral ranges are uniformly distributed, with higher mean τ values of 50% in comparison to the treated cells. The autofluorescence is less affected by the bleaching.

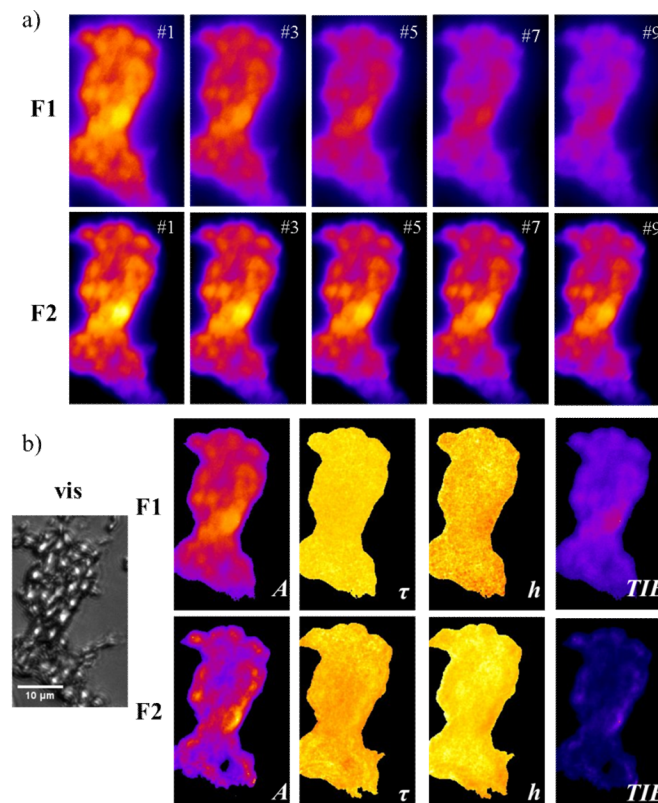


Figure IV.1.18. a) Five selected images of the untreated *C. albicans* cells obtained by time lapse imaging in [327 - 353 nm] (F1) and [370 – 410 nm] (F2) emission spectral ranges. b) VIS image of the cells and parameters from the stretch exponential fitting of the fluorescence intensity decay: A-amplitude map, τ -time constant map, h -heterogeneity map and TIE – Time integrated emission.

Considering that the fluorescent signals acquired in the F1 and F2 ranges correspond to the tryptophan fluorescence in non-polar and polar environments, respectively (Figure IV.1.6), the results obtained by the bleaching kinetics analysis clarifies further the sites of the nanoparticle accumulation. The fluorescence signal in the F1 range comes mostly from the nanoparticles that are situated in the cell membrane. The collected signal in the F2 range comes from the functionalized nanoparticles in polar environment and indicates the accumulation of the nanoparticles on the cells surfaces as well as water channels between cells [42, 43]. The results obtained by ultrastructural analyses of *C. albicans* exposed to silver nanoparticles [10, 36] are in agreement with our observations, and support assignment of the F1 and F2 spectral ranges to cell interior and exterior, respectively. For example, Vazquez-Munoz et al. [10] reported that the Ag NPs aggregate outside the examined *C. albicans* cells, while also confirming their presence in the interior of the cells.

References

- [1] J. R. Lakowicz, *Principles of Fluorescence Spectroscopy*, Springer, Berlin, 3rd edn, 2006.
- [2] R. Dojčilović, J. D. Pajović, D. K. Božanić, V. V. Vodnik, S. Dimitrijević-Branković, A. R. Milosavljević, S. Kaščaková, M. Réfrégiers, V. Djoković, *Analyst* 141 (2016) 1988.
- [3] N. Morimoto, T. Kubo and Y. Nishina, *Scientific Reports* 6 (2016) 21715.
- [4] K. Erickson et al., *Advanced Materials* 22 (2010) 4467.
- [5] Sondi and B. Salopek-Sondi, *Journal of Colloid and Interface Science* 275(1) (2004) 177.
- [6] Aleš Panáček et al., *Biomaterials* 30(31) (2009) 6333.
- [7] G. McDonnell and A. D. Russell, *Clinical Microbiology Reviews* 12 (1999) 147.
- [8] J. R. Morones, J. L. Elechiguerra, A. Camacho, K. Holt, J. Kouri, J. T. Ramirez and M. J. Yacaman, *Nanotechnology* 16 (2005) 2346.
- [9] Dror-Ehre, H. Mamane, T. Belenkova, G. Markovich and A. Adin, *Journal of Colloid Interface Sciences* 339 (2009) 521.
- [10] R. Vazquez-Munoz, M. Avalos-Borja and E. Castro-Longoria, *PLoS One* 9 (2014) e108876.
- [11] S. Hwang, J. Lee, J. H. Hwang, K. J. Kim and D. G. Lee, *FEBS Journal* 279 (2012) 1327.
- [12] D. R. Monteiro et al., *Mycoses* 56 (2013) 672.
- [13] D. R. Monteiro et al., *Journal of Prosthodontic Research* 59 (2015) 42.
- [14] C. N. Lok et al., *Journal of Biological Inorganic Chemistry* 12 (2007) 527.
- [15] F. Jamme, S. Kaščaková, S. Villette, F. Allouche, S. Pallu, V. Rouam and M. Réfrégiers, *Biology of the Cell* 105 (2013) 1.
- [16] F. Jamme, S. Villette, A. Giuliani, V. Rouam, F. Wien, B. Lagarde and M. Réfrégiers, *Microscopy and Microanalysis* 16 (2010) 507.
- [17] C. H. Chuang and Y. T. Chen, *Journal of Raman Spectroscopy* 40 (2009) 150.
- [18] R. I. MacCuspie, *Journal of Nanoparticle Research* 13 (2011) 2893.
- [19] M. P. Seah, *Surface and Interface Analysis* 14 (1989) 488.
- [20] H. S. Shin, S. C. Choi, Y. Jung, S. B. Kim, H. J. Song and H. J. Shin, *Chemical Physics Letters* 383 (2004) 418.
- [21] E. Dulkeith et al., *Physical Review Letters* 89 (2002) 203002.
- [22] N. Ruiz, D. Kahne and T. J. Silhavy, *Nature Reviews Microbiology* 4 (2006) 57.
- [23] Y. Zhou, Y. Kong, S. Kundu, J. D. Cirillo and H. Liang, *Journal of Nanobiotechnology* 10 (2012) 19.
- [24] W. R. Li, X. B. Xie, Q. S. Shi, H. Y. Zeng, Y. S. Ou-Yang and Y. B. Chen, *Applied Microbiology and Biotechnology* 85 (2010) 1115.
- [25] S. Pal, Y. K. Tak and J. M. Song, *Applied Environmental Microbiology* 73 (2007) 1712.
- [26] C. Yanofsky, V. Horn and P. Gollnick, *Journal of Bacteriology* 173 (1991) 6009.
- [27] V. M. Heatwole and R. L. Somerville, *Journal of Bacteriology* 173 (1991) 3601.
- [28] X. Bi, C. Wang, W. Dong, W. Zhu and D. Shang, *the Journal of Antibiotics* 67 (2014) 361.
- [29] R. Koebnik, K. P. Locher and P. Van Gelder, *Molecular Microbiology* 37 (2000) 239.
- [30] P. J. Bond and M. S. Sansom, *Journal of Molecular Biology* 329 (2003) 1035.
- [31] T. Surrey and F. Jähnig, *Proceedings of the National Academy of Sciences of the United States of America* 89 (1992) 7457.
- [32] E. H. Smail, P. Briza, A. Panagos, and L. Berenfeld, *Infection and Immunity* 63 (1995) 4078.
- [33] P. M. Molyneux, S. Kilvington, M. J. Wakefield, J. I. Prydal, N. P. Bannister, *Cornea* 34 (2015) 1588.
- [34] K. Kim, W. Sung, B. Suh, S. Moon, J. Choi, J. Kim, D. Lee, *Biometals* 22 (2009) 235.
- [35] K. Y. Lum, S.T. Tay, C. F. Le, V. S. Lee, N. H. Sabri, R. D. Velayuthan, H. Hassan, and S. D. Sekaran, *Scientific Reports* 5 (2015) 9657.
- [36] H. H. Lara, D. G. Romero-Urbina, C. Pierce, J. L. Lopez-Ribot, M. J. Arellano-Jiménez, and M. Jose-Yacaman, *Journal of Nanobiotechnology* 13 (2015) 91.
- [37] J. Chandra, D. M. Kuhn, P. K. Mukherjee, L. L. Hoyer, T. McCormick, and M. A. Ghannoum, *Journal of Bacteriology* 183 (2001) 5385.
- [38] D. Wüstner, A. L. Larsen, N. J. Faergeman, J. R. Brewer, and D. Sage, *Traffic* 11 (2010) 440.
- [39] M. N. Berberan-Santos, E. N. Bodunov, and B. Valeur, *Chemical Physics* 315 (2005) 171.
- [40] K.C. Lee et al., *Biophysical Journal* 81 (2001) 1265.
- [41] D. Wüstner, T. Christensen, L.M. Solanko, and D. Sage, *Molecules* 19 (2014).
- [42] D.R. Monteiro et al., *Biofouling* 7 (2011) 711.
- [43] D.R. Monteiro et al., *Journal of Applied Microbiology* 114 (2013) 1175.
- [44] D. K. Božanić, Ispitivanje fizičkih osobina nanočestica plementih metala dispergovanih u sintetičkim polimerima i biopolimerima, Doktorska teza, Univerzitet u Beogradu, Beograd, Jul 2011.

IV.2. DUV fluorescence imaging of cancer liver cells incubated with graphene-based nanostructures

Recently, a combination of graphene-based nanomaterials and imaging science approaches has led to the development of novel bioimaging systems [1, 2]. Graphene oxide (GO) and reduced GO (rGO), display advantageous characteristics as biosensing platforms due to the high surface area, good biocompatibility and ability to interact with proteins and polysaccharides [3, 4]. The interaction at biointerfaces is governed by amphiphilic property of GO and rGO. Preparation of hydrophilic and well-defined graphene-based nanostructures in terms of size, number of layers, and controlled surface chemistry with enhanced optical properties is essential for bioimaging purposes. The distinct toxicity mechanism of graphene-based materials particularly on cancer cells is highly dependent on the differential surface oxidation status of the nanomaterial [5, 6]. Electron microscopy revealed variant internalization behaviors for GO and rGO, where some of the water-soluble sulfonated nanographene sheets became folded and compartmentalized into tight bundles within cellular organelles [7]. Developing versatile approaches for efficient transport of the graphene-based nanoprobe to cancer sites is significant for subcellular imaging studies, especially for the fluorescence imaging which is proved to be an important tool in probing the drug delivery process.

Deep UV fluorescence imaging is a non-invasive microscopy technique that provides the possibility to detect fluorophores that exhibit excitation and emission maxima in the UV region. Because DUV imaging technique has high detection sensitivity and provides high spatial resolution, there is no need for conventional enhancing conjugates like dyes or fluorescent molecules. GO exhibits wide fluorescence emission (350-500 nm) that can be excited with DUV excitation. Therefore, we used GO as a fluorescent probe in DUV imaging study of cancer liver cells. The influence of GO on intrinsic fluorescence properties of cancer cells reveals its modes of toxicity that are imposed after the incubation. To further elucidate the effect of the reduction process of graphene oxide in interaction with cancer cells, we fabricated an intermediate product in form of partially reduced graphene oxide (prGO). We used pronounced fluorescent properties of prGO for the detection in the specific cell compartments of cancer liver cells. UV autofluorescent species, particularly aromatic amino acids and NAD(P)H are involved in mitochondrial function, energy metabolism, calcium homeostasis, gene expression, oxidative stress, aging and apoptosis [8]. Alterations in cell state that are occurring as a consequence of pathological conditions modify the amount and

distribution of the fluorophores, and the properties of their environment. Therefore, the autofluorescence analysis will give the information about morphological and physiological state of cells [9]. To explore damage induced changes in cancer cell's autofluorescent properties and to make a correlation with perturbed cell processes, we investigated the intrinsic fluorescence property of cancer liver cells incubated with fabricated graphene's functionalities.

In the first part of this section we will report on changes in structural and optical properties of graphene oxide affected by the reduction process. In second part of the section we will present results of the bioimaging study of cancer liver cells (Huh7.5.1 cell line) incubated with graphene oxide, partially reduced graphene oxide and reduced graphene oxide.

IV.2.1. Structure and optical properties of graphene oxide, partially reduced graphene oxide and reduced graphene oxide

Modified Hummers method was used for the fabrication of graphene oxide and the reduction was done in the presence of hydrazine hydrate (details of the procedure are in Experimental section III.1). Partial reduction of graphene oxide can be achieved by carefully controlling the reduction process. The studies on characterization of graphene oxide reduced with hydrazine reported that the reduction process is very sensitive to the amount of reducing agent used [10, 11]. By carefully tuning the concentration of hydrazine and the reduction conditions, it is possible to control and maintain fabrication of the intermediates. Figure IV.2.1 shows high resolution TEM micrographs with representative elemental mapping of the highlighted surface area of graphene oxide (GO), partially reduced graphene oxide (prGO) and reduced graphene oxide (rGO) layers. Oxygen content is decreasing with the time of reduction as it can be seen from the (red) oxygen maps (Figure IV.2.1b,c) and thus the C/O ratio is increasing, which is confirmed by EDS results (Figure IV.2.2). Fabrication of graphene oxide produced stable 2d nanostructures with $C/O \sim 4$. For prGO and rGO, different C/O content is obtained with the hydrazine reduction and consistent surface morphology of the layers is preserved ($C/O \sim 7$ and $C/O \sim 10$, respectively). Also, it can be seen that the partial reduction with hydrazine did not cause visible damage of the layered structures.

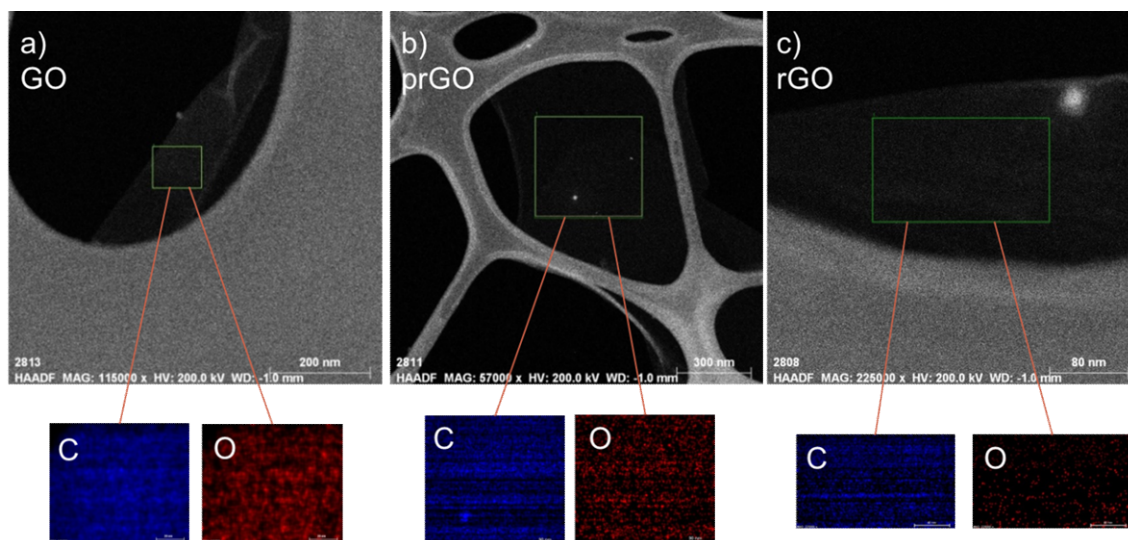


Figure IV.2.1. HRTEM micrographs and elemental maps of carbon and oxygen for a) graphene oxide (GO), b) partially reduced graphene oxide (prGO) and c) reduced graphene oxide (rGO). The green outline is highlighting the examined surface for elemental composition.

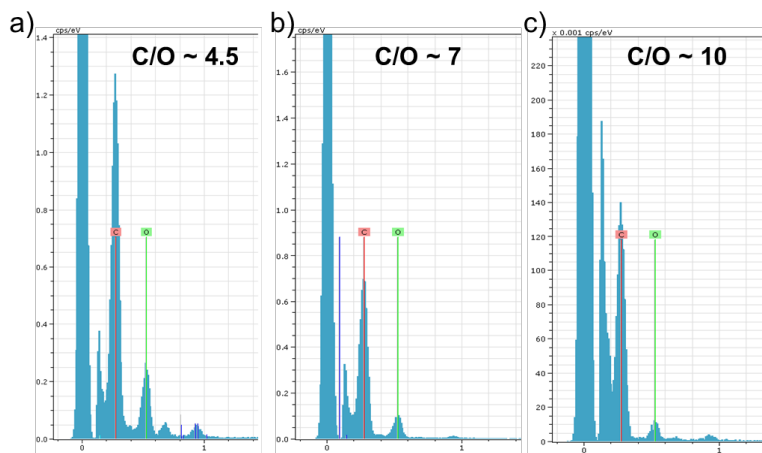


Figure IV.2.2. Energy Dispersive Spectroscopy (EDS) results on elemental analysis of a) graphene oxide b) partially reduced graphene oxide and c) reduced graphene oxide. Highlighted ratios of carbon and oxygen show decreased values with the degree of reduction.

Additional micrographs of GO made by using SEM are presented in Figure IV.2.3. Sheet structures of graphene with high oxygen content are piled up in layers. The single sheet of GO with large surface area is obtained with modified Hummers method (Figure IV.2.3b).

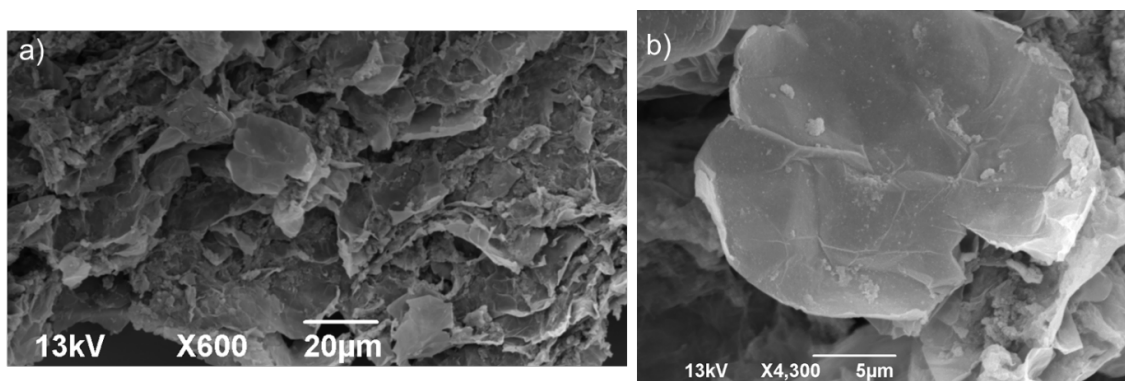


Figure IV.2.3. Scanning electron microscopy (SEM) micrographs of graphene oxide fabricated with modified Hummers method.

Figure IV.2.4 shows results of the Raman-AFM analysis of reduced GO flake (rGO). The 3D AFM topography image (Figure IV.2.4 b) is showing two small white regions on the surface that represent defects. The corresponding Raman image shows ratio of peak intensity from the D peak (ca. 1345 cm^{-1} shift) to the G peak (ca. 1588 cm^{-1} shift). Increased D/G ratio after the reduction suggests a decrease in the average size of the sp^2 clusters. It can be seen that highest value for the D peak is in the defective regions of the surface.

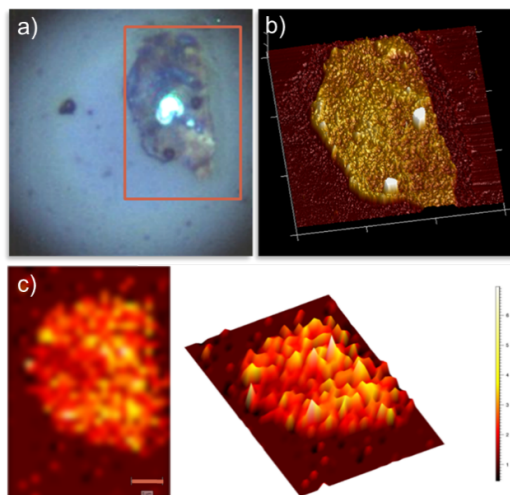


Figure IV.2.4. Results of the combined AFM/Raman analyses of rGO flakes: a) bright light image of the selected area, b) 3D AFM topography image and c) Raman microspectroscopy image representing D/G peak intensity ration with 5 micrometer scale.

The results of the Raman spectroscopy of the prepared samples are shown in in Figure IV.2.5. The spectrum of graphene oxide displays characteristic behavior with the pronounced D band at 1340 cm^{-1} and the G peak at 1586 cm^{-1} . The G band comes from the in-plane vibrations of sp^2 carbon atoms and represents doubly degenerate phonon mode (E_{2g} symmetry) at the center of the Brillouin zone. On the other hand, the D peak (symmetry A_{1g} mode) rises due to the presence of the sp^3 carbons, as well as the defects on graphene sheet [12] and renewal of sp^2 carbon in graphene oxide [13]. Consequently, since the oxygen-carbon bonds are formed in the sp^3 hybridization, the reduction process can be followed by a change in the relative intensity of these two bands (I_D/I_G). The I_D/I_G ratio value for GO is 0.96 and after the reduction it increases to 1.12 and 1.6 for prGO and rGO, respectively. With longer exposure to hydrazine, the I_D/I_G ratio is increasing indicating formation of a large number of small sized domains of sp^2 carbon atoms [14, 15]. This affects the in plane vibrations of sp^2 carbon atoms and, therefore, reflects on G mode which is manifested as a decrease in the peak intensity. Oxygen bonding produces change in the electronic structure of the π and π^* bands which influences in-plane vibrations in sp^2 and reflects in altered intensity of the observed D mode frequency [16].

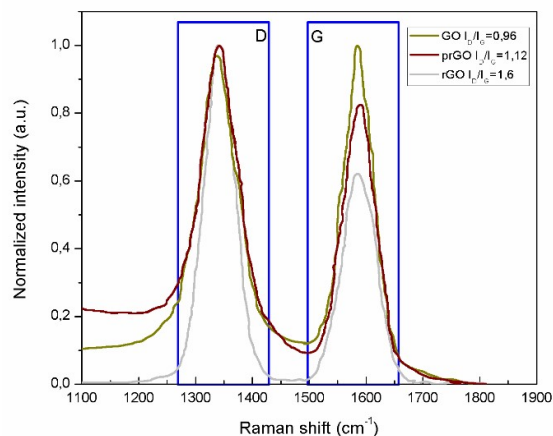


Figure IV.2.5. Normalized Raman spectra of GO, prGO and rGO. Blue rectangles are highlighting D and G band, and the ratio of the original intensities of the D and G peaks is given in the inset.

Because the energy gap between the π and π^* states depends on the size of sp^2 clusters, the reduction affects the absorption spectra of graphene oxide. The attenuation of light by GO aqueous dispersions during the reduction process was monitored by UV visible spectroscopy (Figure IV.2.6). For the GO dispersion, the absorption spectra consists of two distinct peaks at 220 nm and 310 nm which belong to specified transitions of π - π^* (C=C) and n - π^* (C=O), respectively. There is a red shift of the absorbance peak at 220 nm when the reduction occurs. The vanishing of shoulder observed at 310 nm after the reduction is attributed to the decrease in concentration of carboxyl groups.

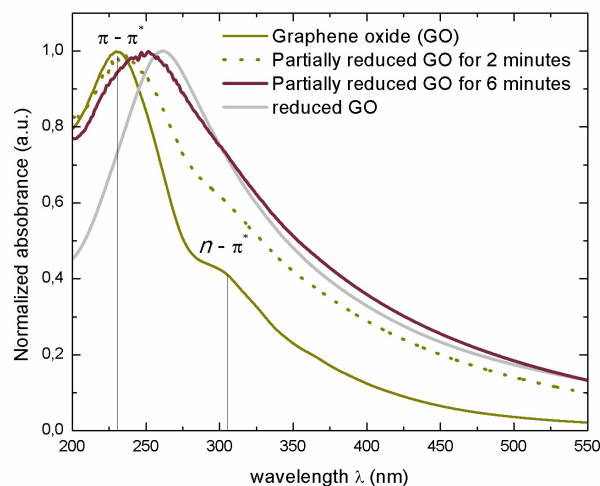


Figure IV.2.6. Normalized UV-vis spectra of GO, partially reduced GO for different times of reduction, and reduced GO.

Due to functionalization-induced opening of the energy gap, GO is expected to emit photoluminescence across its optical bandgap. For the excitation in the UV part of the EM spectrum, GO possess fluorescence originated from radiative recombination of electron-hole pairs which are located in small sp^2 domains [15] with pronounced emission between 400 and 500 nm. In Figure IV.2.7 are presented emission excitation matrices of the GO, prGO and rGO. As it can be seen, there are two distinct regions with pronounced photoluminescence intensity noted as region I ($\lambda_{exc}=270$ nm, $\Delta\lambda_{em}=380-550$ nm) and region II ($\lambda_{exc}=300$ nm, $\Delta\lambda_{em}=350-450$ nm). Because we wanted to investigate intrinsic fluorescence from the incubated cancer liver cells, we are interested in the first region with excitation in deep UV part of EM spectrum ($\lambda_{exc}=270$ nm).

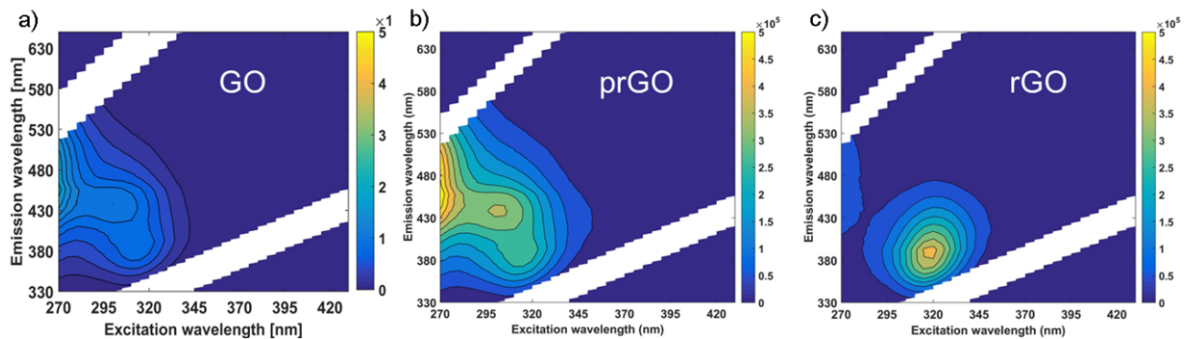


Figure IV.2.7. Emission excitation matrices for a) GO, b) prGO and c) rGO. We used excitation wavelength range (270 – 430) nm and emission range (330-650) nm.

Extracted single spectra from emission excitation matrices are given in Figure IV.2.8a and c, where it can be seen that the partially reduced graphene oxide yields the highest fluorescence. Apparently, the partial reduction caused specific rearrangement of the honeycomb network which resulted in more effective recombination of excited electrons that further led to the increase in fluorescence intensity. The change in optical properties after partial reduction of graphene oxide was mainly influenced by the size effect of different arrangements of sp^2 localized sites. In Figure IV.2.8b and d are shown corresponding normalized photoluminescence spectra. Grey rectangles are emphasizing emission ranges that are used for the collection of the fluorescence signal in DUV imaging [F1 (327 - 353 nm), F2 (370 - 410 nm) and F3 (420 - 480 nm)]. The autofluorescence signal is detected in all three spectral ranges and the contribution of the fluorescence coming from graphene's functionalities was monitored in F2 and F3 emission ranges.

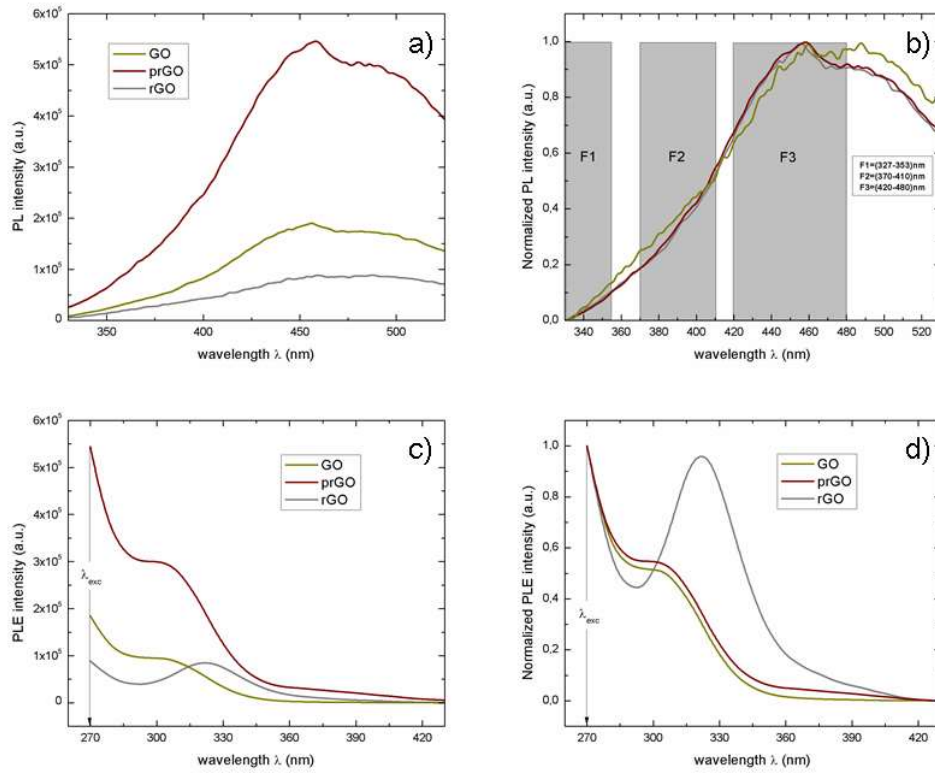


Figure IV.2.8. a, b) Photoluminescence (PL) and normalized PL emission spectra of graphene oxide (GO), partially reduced graphene oxide (prGO) and reduced graphene oxide (rGO) with highlighted emission ranges (grey rectangles) used in deep UV fluorescence imaging. The emission ranges: F1 = (327-353) nm, F2 = (370-410) nm and F3 = (420-480) nm for $\lambda_{exc} = 270$ nm. c, d) PL excitation (PLE) and normalized PLE spectra of GO, prGO and rGO for the emission wavelength of 460 nm. Long arrow is indicating the excitation wavelength used in DUV fluorescence imaging.

IV.2.2. DUV Fluorescence imaging of Huh7.5.1 cancer liver cells with graphene oxide, partially reduced graphene oxide and reduced graphene oxide

Cancer liver cells (Huh7.5.1 cell line) are incubated with GO, prGO and rGO. The selected visible microscopy images are presented in Figure IV.2.9. It can be seen that the morphology of the cells was not affected significantly by the presence of GO. Cancer cells kept their form and the occurrence as isolated cells and, also, cell pairs was consistently observed. However, folded GO aggregates were observed in the vicinity of the cells as it can be seen in the bright-field images. As for the cells incubated with prGO and rGO, the impact of the material on the cells was higher, since we noticed the cell sites with inflicted damage. Also, the black agglomerates of reduced graphene oxides (red arrows), that can be seen in all the micrographs, revealed the sites of introducing impairment (Figure IV.2.9). Cells have ability to internalize, actively fold and compartmentalize relatively large pieces of graphite and yet still remain healthy [6, 7, 17]. As it will be shown below, we have observed that the internalized prGO and rGO sheets are exhibiting pronounced fluorescence in comparison to the non-internalized aggregated sheets.

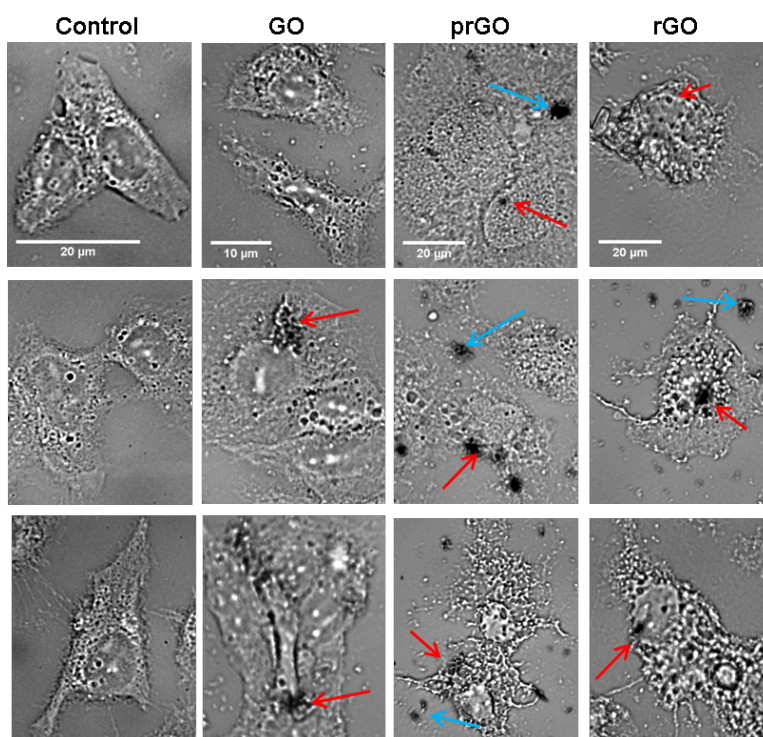


Figure IV.2.9. Bright field micrographs of Huh 7.1.5 cells incubated with or without GO, prGO and rGO. Red arrows are indicating localization of graphene functionalities at damaged cell sites. Blue arrows are showing non-internalized graphene entities.

Deep UV imaging of treated and untreated cancer liver cells Huh7.5.1 was performed for the excitation wavelength of 270 nm and the fluorescence emission was monitored in three spectral ranges F1 (327 - 353 nm), F2 (370 - 410 nm) and F3 (420 - 480 nm). Graphene's fluorescence centers have wide blue emission that primarily belongs to the F3 filter (Figure IV.2.8b), and partially to the F2 filter. Huh cells have intrinsic fluorescence that has been detected in all three spectral emission ranges, with comparable fluorescence intensities (Figure IV.2.10). The most dominant autofluorescent specie in F3 filter is NADH, which can be a good indicator for various kinds of processes that are occurring in mitochondria [8, 18]. We observed that the fluorescence emission coming from the cells when they are excited with deep UV light is mainly homogeneously distributed in the cytoplasmic region such as mitochondria. Also, the nucleoli become the brightest intercellular fluorescent sites which is also observed in reported studies [19, 20]. Therefore, the autofluorescence intensity is dependent on the degree of damage to the cells.

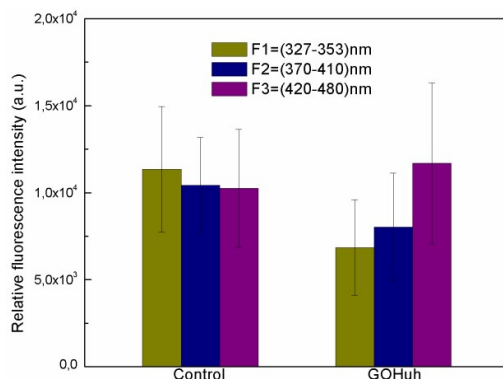


Figure IV.2.10. Statistics on mean fluorescent intensity per single cell for untreated Huh7.5.1 cells (control) and GO incubated Huh7.5.1 cells (number of cells counted $n > 30$). The error bars represent standard deviations of the fluorescence intensity.

Fluorescent images obtained in F3 emission range and corresponding bright-field micrographs are presented in Figure IV.2.11. The intensity of the fluorescence in the F3 filter for the graphene oxides (Figure IV.2.10) is showing similar fluorescence intensity in comparison to the control sample. The mild quenching of the autofluorescence by graphene oxide was observed for the F1 and F2 filter. This can be explained by the fact that GO is prone to quench tryptophan, tyrosine and phenylalanine [21], via non-radiative recombination of the molecule's excited electrons into the energy bands of GO. These amino acids are the main cell fluorophores with excitation and emission maxima in the 200-400 nm wavelength range [22]. As for the cells incubated with prGO, we observed pronounced intensity of the

fluorescence, which was localized in the cell (Figure IV.2.11b). The signal intensities on the fluorescence image (gem LUT) were, for clarity, scaled to the top 85%. It can be seen that such high intensities are coming from opaque entities that belong to prGO internalized by the cell. This is also the case for the cells incubated with rGO (Figure IV.2.11c). On other hand, the images show that the prGO and rGO aggregates localized outside the cells do not fluoresce (see blue arrows in the Figure IV.2.9). Consequently, the cell compartments in which the reduced graphene oxides are present show higher fluorescence intensity, than the rGO aggregates themselves allocated in the vicinity of the cells. The reason behind the lower fluorescence intensity of the rGO aggregates located outside the cell is in the formation of the π -stacked complexes in the aggregates that induces static quenching. On the other hand, in the internalized rGO, apparently, the cellular material separates the rGO sheets, thus preventing the π -stacking. Additionally, we propose that specified localization of reduced graphene oxides induced changes in mitochondrial function and therefore affected NADH which is the main fluorophore detected in F3 filter. For the cells in which the localization of the graphene's functionalities was detected, we observe three times higher fluorescence intensity than that of the control samples (Figure IV.2.11b,c). The presence of the graphene's functionalities in combination with the inserted damage that they cause had overall influence on the fluorescence properties of Huh cells. Further we investigate the fluorescence dynamics with consecutive imaging of the treated and untreated cells.

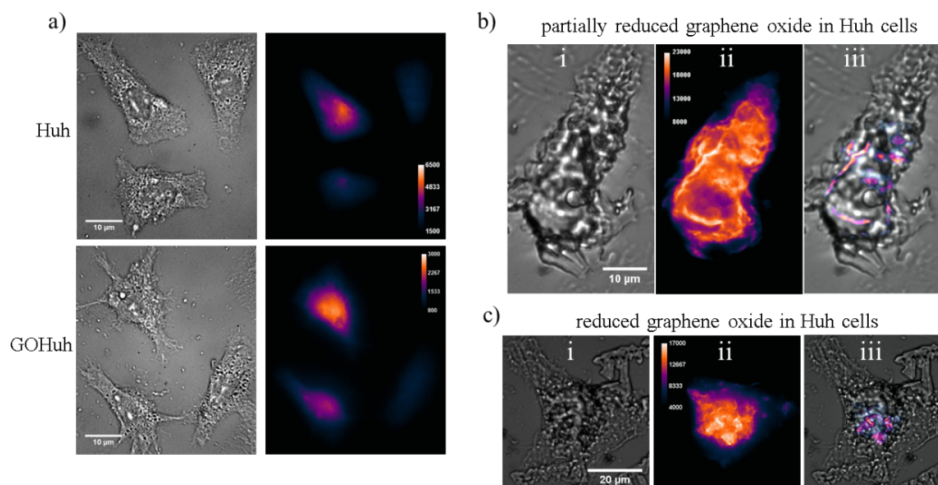


Figure IV.2.11. Localization of graphene's functionalities in cancer liver cells. Huh cells incubated with b) partially reduced graphene oxide and c) reduced graphene oxide. i – bright field images, ii – images with fluorescence emission in F3 (420-480nm) spectral range and iii – composite images made with merging bright field images and fluorescence images from the F3 spectral range with profound maxima highlighted that belongs >85% of the total fluorescence intensity.

In the case of agglomerated cells (Huh cells incubated with GO), we have observed that GO is localized in cracks and channels between aggregated Huh cells (Figure IV.2.12.). Lammel et al [17] reported on formation of thick filament bundles by the cancer liver cells as a respond to the inflicted damage of graphene oxide. We propose that the cracks and elongated channels between and throughout surface of the cells resemble sites of injury inflicted by sharp edges of GO.

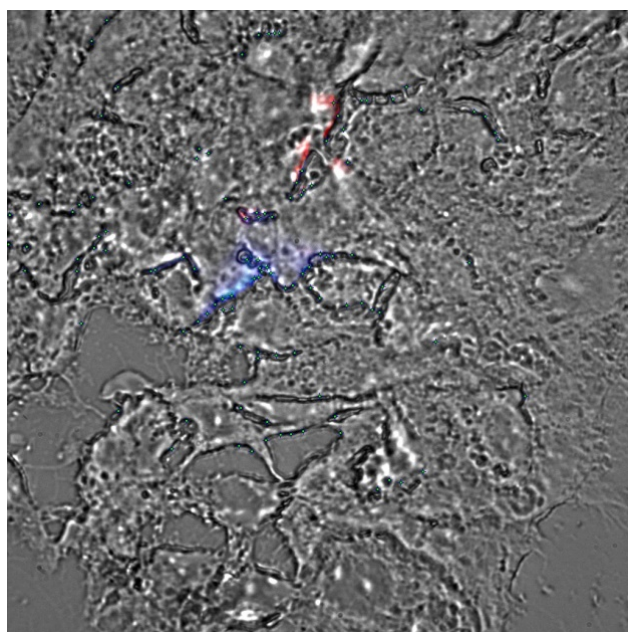


Figure IV.2.12. Huh cells incubated with GO are presented in composite micrograph of bright-field image and fluorescence images obtained in F2=327-410 nm (pseudo-colored in red) and F3=420-480 nm (pseudo-colored in blue) emission ranges. Green dots are representing local fluorescence maxima.

In Figure IV.2.13 we can see the behavior of local maxima with time for all the samples in F2 and F3 emission range. It can be seen that the presence of graphene oxides highly influences the fluorescence kinetics. For the F3 filter (Figure IV.2.13b) the fluorescence of the cells incubated with graphene oxide is rising linearly with time. This can be attributed to the fluorescence transfer from the excited cell emitters to the two major fluorophores present: GO and NADH. The increase of intensity, observed for further UV exposure, could be explained as an induction of membrane damage and consequent mitochondrial damage, with efflux of NAD(P)H in the cytoplasm [19, 23]. The reduced graphene oxides, on the other hand, show different fluorescence dynamics in comparison to the control sample. The bleaching kinetics for the prGO and rGO incubated cells shows

fluorescence maxima after 5 minutes of recording, followed by a fast decay. Fluorescence relocation combined with a decrease in the average fluorescence lifetime suggests the possibility of an increase in the intracellular free NAD(P)H. This idea is supported by the finding of UV induced red shift in the autofluorescence peak [19]. That was observed for the control cells, as the fluorescence intensity detected in F3 filter after prolonged exposure to UV is much higher than the intensity in F2 filter. This is a clear evidence of the obstruction of the intrinsic fluorescence caused by confined graphene functionalities.

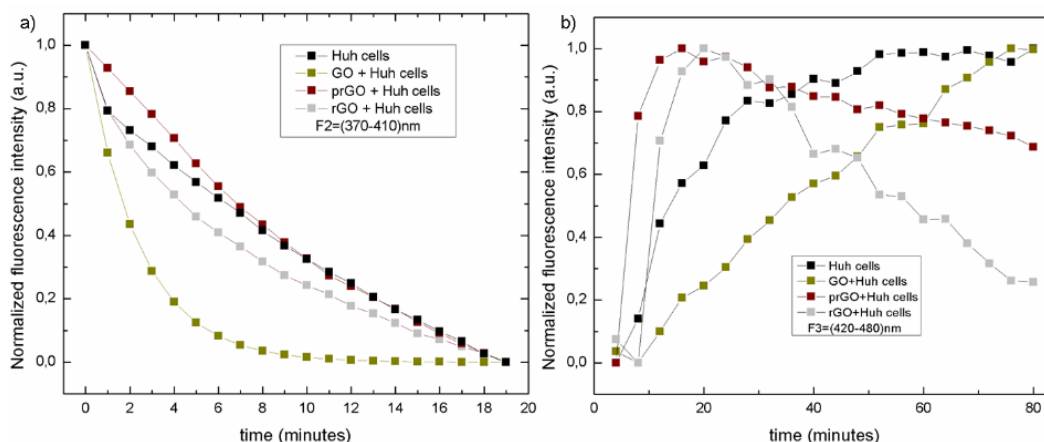


Figure IV.2.13. Timelapse experiments for the fluorescence detected in a) F2 (370-410nm) and b) F3 (420-480nm) emission range. Data are representing mean fluorescence intensities of the local maxima with time.

Because the emission spectra of GO, prGO and rGO partially belongs to the second emission range, we carried out the analysis of bleaching kinetics in F2 spectral emission range (Figure IV.2.13a). In that way we can monitor the influence of graphene's functionalities on other UV autofluorescent species. The presence of GO in incubated cells affected the bleaching dynamics of the dominant fluorophores (e.g. tryptophan) in F2 filter.

We have used bleaching kinetics of the fluorescence in F2 emission range, in order to further evaluate the influence of graphene oxides on fluorescent properties of Huh cells. The bleaching kinetics of the Huh7 cells (Figure IV.2.14) revealed homogenous distribution of τ - values (lifetime of the fluorophores) across the surface of the cell. Time integrated emission (TIE) results confirmed the starting observation that the fluorescence in control cells is coming from nucleus.

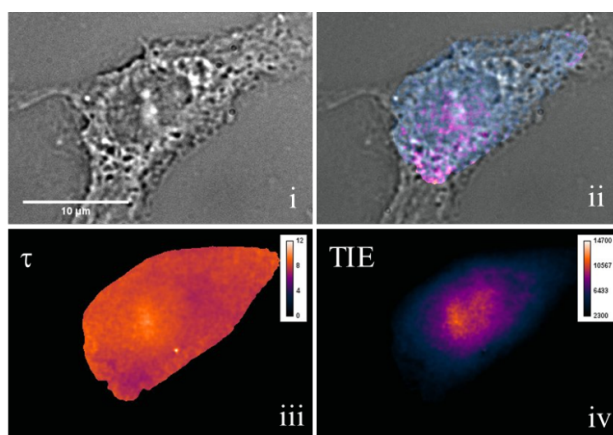


Figure IV.2.14. i) Bright-field image of Huh cell, ii) composite image pseudo-colored with gem LUT, iii) τ -map and iv) time integrated emission map (TIE).

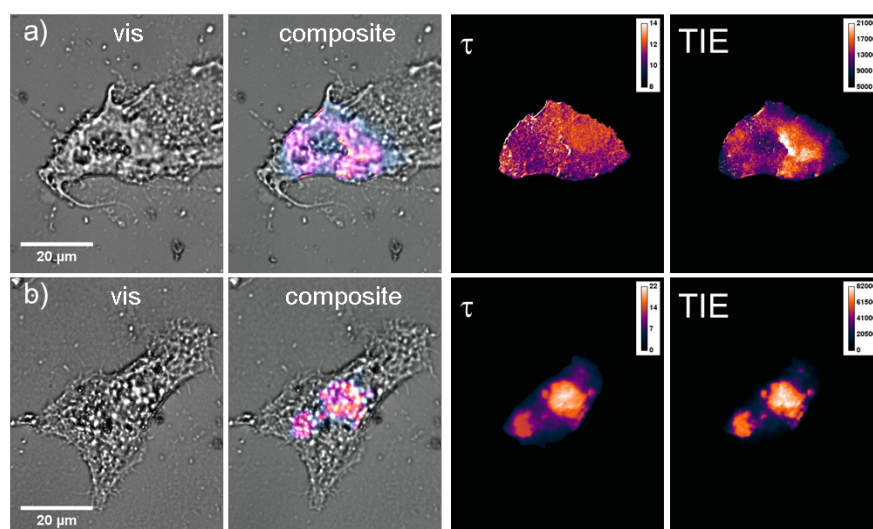


Figure IV.2.15. Bright-field image (vis), composite, τ map and TIE map of Huh cells incubated with a) prGO. b) Huh cells incubated with rGO. Fluorescence images obtained in F2=327-410 nm (pseudo-colored with gem LUT).

In Figure IV.2.15 are presented images for Huh cells incubated with prGO and rGO. Bright-field images reveal black entities of prGO and rGO encapsulated in the cell. Composite images are highlighting the pronounced fluorescence intensities (>85% out of maximal value) assigned to the pseudo-color (gem LUT) predominantly localized in the black areas. The distribution of τ - values is highly inhomogeneous and it is correlated with time integrated emission map. This indicates that the highest fluorescence is coming from the regions of the cells with fluorophores with longer lifetimes. This is in contrast to the results obtained for the control sample. Areas of cell with different bleaching dynamics indicate the presence of reduced graphene oxide and highlight their influence on intrinsic fluorescence properties.

In this study, we successfully fabricated a stable fluorescent nanostructure in form of partially reduced graphene oxide and employed it in deep-UV bioimaging of cancer liver cells. Investigation of the fluorescence of the cells treated with graphene's functionalities (GO, prGO and rGO) revealed pronounced inhibition of cells' viability and damage dependent fluorescence intensity of cells. Bleaching dynamics of cells with visible localization of reduced graphene oxides was used to assess the influence on intrinsic properties of autofluorescent species in the cells. The perturbation in fluorescence dynamics of cancer cells confirmed the toxicity effect of reduced graphene oxides.

References

- [1] C. Cheng, S. Li, A. Thomas, N. A. Kotov and R. Haag, *Chemical Reviews* 117 (2017) 1826.
- [2] D. Du, Y. Yang and Y. Lin, *MRS Bulletin* 37(12) (2012) 1290.
- [3] S. Mahanta and S. Paul, *Colloids and Surfaces B: Biointerfaces* 134 (2015) 178.
- [4] S. Zhang, K. Yang, L. Feng and Z. Liu, *Carbon* 49 (2011) 4040.
- [5] N. Morimoto, T. Kubo and Y. Nishima, *Scientific Reports* 6 (2016) 21715.
- [6] N. Chatterjee, H. J. Eom and J. Choi, *Biomaterials* 35 (2014) 1109.
- [7] S. J. Corr et al., *Nanoscale Research Letters* 8 (2013) 208.
- [8] M. Monici, *Biotechnology Annual Review* 11 (2005) 227.
- [9] A. A. Heikal, *Biomarkers in Medicine* 4(2) (2010) 241.
- [10] K. Chua and M. Pumera, *Chemical Communications* 52 (2015) 72.
- [11] K. Chua and M. Pumera, *Chemical Society Reviews* 43 (2014) 291.
- [12] A. Yang et al., *Carbon* 47 (2009) 145.
- [13] S. Yin et al., *Journal of Solid State Chemistry* 237 (2016) 57.
- [14] C. Ferrari and J. Robertson, *Physical Review B* 61(20) (2000) 14095.
- [15] G. Eda et al., *Advanced materials* 22 (2010) 505.
- [16] F. Tuinstra and J. L. Koenig, *the Journal of Chemical Physics* 53 (1970) 1126
- [17] T. Lammel, P. Boisseaux, M. L. Fernandez-Cruz and J. M. Navas, *Particle and Fiber toxicology* 10 (2013) 27.
- [18] D. Chorvat Jr and A. Chorvatova, *Laser Physics Letters* 6(3) (2009) 175.
- [19] K. K. Konig, P. T. C. So, W. W. Matulin, B. J. Tromberg and E. Gratton, *Journal of Microscopy* 183 (1996) 197.
- [20] M. Monici et al., *Diagnostic applications in haematology* 2928 (1996) 180.
- [21] S. Li et al., *ACS Symposium series* Chapter 3 (2015) 43.
- [22] F. Jamme, S. Kaščáková, S. Villette, F. Allouche, S. Pallu, V. Rouam and M. Réfrégiers, *Biology of the Cell* 105 (2013) 1.
- [23] K. Blinova et al., *Biochemistry* 44 (2004) 2585.

V Conclusion

In this dissertation, we investigated two types of fluorescent nanostructures: tryptophan functionalized silver nanoparticles and partially reduced graphene oxide. These nanostructures were studied with various microscopy and spectroscopic methods in order to establish their structure and physical properties. After that, the fabricated nanostructures were used in deep UV bioimaging study of bacteria *Escherichia coli*, fungus *Candida albicans* and cancer liver cell line Huh7.5.1.

Antimicrobial nanostructures that can absorb and emit light in the UV region were prepared by functionalization of silver nanoparticles with tryptophan amino acid and used as environmentally sensitive fluorescent probes. The nanostructures were characterized by transmission electron microscopy and different spectroscopic methods (UV-vis, FTIR, XPS, and photoluminescence). The TEM images and the analyses of the UV-vis spectra suggested that the addition of tryptophan led to the formation of hybrid nanostructures with pronounced eccentricity and larger sizes with respect to that of the initial silver nanoparticles. XPS results indicate that functionalization results in the formation of amino acid layers on the nanoparticle surface. FTIR spectra showed that tryptophan molecules interact with silver nanoparticles via all available functional groups. The process of internalization of silver nanoparticles in *Escherichia coli* cells was followed by means of DUV fluorescence imaging. The DUV fluorescence imaging of live *E. coli* cells and *E. coli* cells incubated with different AgTrp colloids was performed using a 280 nm monochromatised synchrotron beam as an excitation source. The analyses of the fluorescence images showed that a signal detected in the [327–353 nm] emission range can be attributed to the fluorescence of AgTrp nanostructures within *E. coli* cells. The fluorescence of the amino acid in this domain suggested that the tryptophan molecules were localized in the hydrophobic environment. Furthermore, for the imaging conditions employed, the spatial resolution of the fluorescence images was 154 nm, which was sufficient to perform analyses of the accumulation of AgTrp nanostructures in the bacteria. The DUV images showed an increase in the intensity of fluorescence towards the interior of the cells indicating that *E. coli* internalized the tryptophan functionalized nanoparticles. The results imply that the tryptophan-functionalized silver nanoparticles interact with cell membranes *via* insertion of the amino acid into the phospholipid bilayer and enter the cells.

DUV imaging of *C. albicans* incubated with AgTrp showed that incubation of the fungus with functionalized nanoparticles results in significant increase in the fluorescence signal. Due to the environmentally sensitive fluorescence of the tryptophan on the surface of the nanoparticles, it was possible to investigate the origin of the fluorescence and search for the sites where the accumulation of the nanoparticles takes place. Two pseudohyphae with budding spores in early stage of growth were used to show that the interaction may depend on the polymorphic stage of the fungus. It was observed that the nanoparticles interacted with budding spores rather than with pseudohyphae filaments. The analyses of the fluorescence signals from the *C. albicans* cell showed that incubation results in an increase of the fluorescence intensity in both investigated spectral ranges ([327–353 nm] and [370–410 nm]). By performing photobleaching tests, we were in position to identify the regions with the specific bleaching dynamics and associate them with the polarity of the environment in which the nanoparticles are situated. This analysis suggested that the functionalized silver nanoparticles were predominantly situated at the surface of the *C. albicans* cells, but that they also penetrate the cell walls.

Modified Hummers method was used for the fabrication of graphene oxide and the reduction was performed in the presence of hydrazine hydrate. Partial reduction of graphene oxide was achieved by controlling the duration of the reduction process. HRTEM micrographs of GO, prGO and rGO showed isolated monolayers with preserved structure. Elemental analysis revealed that the C/O ratio values were dependent on the time of reduction, which is also confirmed by Raman spectroscopy. The change in optical properties was monitored by photoluminescence and UV-vis spectroscopies. The partially reduced graphene oxide showed the highest intensity of photoluminescence emission for the excitation that belongs to DUV part of the EM spectrum. The fluorescent GO, prGO and rGO nanostructures were used in DUV fluorescence imaging study of cancer liver cell line Huh7.5.1. The interaction of the nanostructures with the cells resulted in strong increase in the fluorescence intensity with respect to the autofluorescence of the control sample. Bleaching kinetics studies showed that the time dependence of the fluorescence emission from graphene oxide internalized cells is different from that of the intrinsic fluorescence of the untreated cells.

List of author's publications

1. R. Dojčilović, J. D. Pajović, D. K. Božanić, V. V. Vodnik, S. Dimitrijević-Branković, A. R. Milosavljević, S. Kaščaková, M. Réfrégiers, V. Djoković: Fluorescence nanoprobe for single bacterium tracking: Functionalization of silver nanoparticles with tryptophan to probe the nanoparticle accumulation with single cell resolution. *Analyst* (2016) 141, 1988 – 1996, IF = 4.033
2. R. Dojčilović, J. D. Pajović, D. K. Božanić, U. Bogdanović, V. V. Vodnik, S. Dimitrijević-Branković, M. G. Miljković, S. Kaščaková, M. Réfrégiers and V. Djoković Interaction of amino-acid functionalized silver nanoparticles and *Candida albicans* polymorphs: A deep-UV fluorescence imaging study. *Colloids and Surfaces B: Biointerfaces* (2017) 155, 341-348, IF=3.902
3. J. D. Pajović, R. Dojčilović, D. K. Božanić, V. V. Vodnik, S. Dimitrijević-Branković, S. Kaščaková, M. Réfrégiers, M. Markelić, V. Djoković: Deep UV fluorescence imaging study of *Candida albicans* cells treated with gold-riboflavin hydrocolloids. *Optical and Quantum Electronics* (2016) 48:311, IF = 1.29
4. J. D. Pajović, R. Dojčilović, D. K. Božanić, S. Kaščaková, M. Réfrégiers, S. Dimitrijević-Branković, V. V. Vodnik, A. R. Milosavljević, E. Piscopiello, A. S. Luyt, V. Djoković: Tryptophan-functionalized gold nanoparticles for deep UV imaging of microbial cells. *Colloids and Surfaces B: Biointerfaces* (2015) 742, IF = 3.902
5. N. N. Nedeljković, M. D. Majkić, D. K. Božanić and R. J. Dojčilović: Dynamics of the Rydberg state population of slow highly charged ions impinging a solid surface at arbitrary collision geometry. *Journal of Physics B: Atomic, Molecular and Optical Physics* (2016) 49, 125201, IF = 1.833
6. V. P. Pavlović, V. B. Pavlović, B. Vlahović, D. K. Božanić, J. D. Pajović, R. Dojčilović, V. Djoković: Structural properties of composite of polyvinylidene fluoride and mechanically activated BaTiO₃ particles. *Physica Scripta T157* (2013) 014006, IF = 1.194

Изјава о ауторству

Потписани-а Радован Дојчиловић
број индекса 8012/2012

Изјављујем,

да је докторска дисертација / докторски уметнички пројекат под насловом
“Fabrication of silver-tryptophan and graphene oxide fluorescent nanostructures and
investigation of their interaction with biological systems”
“Фабрикација сребро-триптофан и графен оксид флуоресцентних наноструктура и
испитивање њихове интеракције са биолошким системима”

- резултат сопственог истраживачког / уметничког истраживачког рада,
- да предложена докторска теза / докторски уметнички пројекат у целини ни у деловима није била / био предложена / предложен за добијање било које дипломе према студијским програмима других факултета,
- да су резултати коректно наведени и
- да нисам кршио/ла ауторска права и користио интелектуалну својину других лица.

Потпис докторанда

У Београду, 29.05.2017.



Изјава о коришћењу

Овлашћујем Универзитетску библиотеку „Светозар Марковић“ да у Дигитални репозиторијум Универзитета у Београду унесе моју докторску дисертацију под насловом:

“Fabrication of silver-tryptophan and graphene oxide fluorescent nanostructures and investigation of their interaction with biological systems”

“Фабрикација сребро-триптофан и графен оксид флуоресцентних наноструктура и испитивање њихове интеракције са биолошким системима”

која је моје ауторско дело.

Дисертацију са свим прилозима предао/ла сам у електронском формату погодном за трајно архивирање.

Моју докторску дисертацију похрањену у Дигиталном репозиторијуму Универзитета у Београду и доступну у отвореном приступу могу да користе сви који поштују одредбе садржане у одабраном типу лиценце Креативне заједнице (Creative Commons) за коју сам се одлучио/ла.

1. Ауторство (CC BY)

2. Ауторство – некомерцијално (CC BY-NC)

3. Ауторство – некомерцијално – без прерада (CC BY-NC-ND)

4. Ауторство – некомерцијално – делити под истим условима (CC BY-NC-SA)

5. Ауторство – без прерада (CC BY-ND)

6. Ауторство – делити под истим условима (CC BY-SA)

(Молимо да заокружите само једну од шест понуђених лиценци.

Кратак опис лиценци је саставни део ове изјаве).

Потпис аутора

У Београду, 29.05.2017.



1. **Ауторство.** Дозвољавате умножавање, дистрибуцију и јавно саопштавање дела, и прераде, ако се наведе име аутора на начин одређен од стране аутора или даваоца лиценце, чак и у комерцијалне сврхе. Ово је најслободнија од свих лиценци.

2. **Ауторство – некомерцијално.** Дозвољавате умножавање, дистрибуцију и јавно саопштавање дела, и прераде, ако се наведе име аутора на начин одређен од стране аутора или даваоца лиценце. Ова лиценца не дозвољава комерцијалну употребу дела.

3. **Ауторство – некомерцијално – без прерада.** Дозвољавате умножавање, дистрибуцију и јавно саопштавање дела, без промена, преобликовања или употребе дела у свом делу, ако се наведе име аутора на начин одређен од стране аутора или даваоца лиценце. Ова лиценца не дозвољава комерцијалну употребу дела. У односу на све остале лиценце, овом лиценцом се ограничава највећи обим права коришћења дела.

4. **Ауторство – некомерцијално – делити под истим условима.** Дозвољавате умножавање, дистрибуцију и јавно саопштавање дела, и прераде, ако се наведе име

аутора на начин одређен од стране аутора или даваоца лиценце и ако се прерада дистрибуира под истом или сличном лиценцом. Ова лиценца не дозвољава комерцијалну употребу дела и прерада.

5. **Ауторство – без прерада.** Дозвољавате умножавање, дистрибуцију и јавно саопштавање дела, без промена, преобликовања или употребе дела у свом делу, ако се наведе име аутора на начин одређен од стране аутора или даваоца лиценце. Ова лиценца дозвољава комерцијалну употребу дела.

6. **Ауторство – делити под истим условима.** Дозвољавате умножавање, дистрибуцију и јавно саопштавање дела, и прераде, ако се наведе име аутора на начин одређен од стране аутора или даваоца лиценце и ако се прерада дистрибуира под истом или сличном лиценцом. Ова лиценца дозвољава комерцијалну употребу дела и прерада. Слична је софтверским лиценцама, односно лиценцама отвореног кода.

Изјава о истоветности штампане и електронске верзије докторског рада

Име и презиме аутора Радован Дојчиловић

Број индекса 8012/2012

Студијски програм Физика кондензоване материје и статистичка физика

Наслов рада

“Fabrication of silver-tryptophan and graphene oxide fluorescent nanostructures and investigation of their interaction with biological systems”

“Фабрикација сребро-триптофан и графен оксид флуоресцентних наноструктура и испитивање њихове интеракције са биолошким системима”

Ментор др Владимир Ђоковић

Изјављујем да је штампана верзија мог докторског рада истоветна електронској верзији коју сам предао/ла ради похрањена у **Дигиталном репозиторијуму Универзитета у Београду**.

Дозвољавам да се објаве моји лични подаци везани за добијање академског назива доктора наука, као што су име и презиме, година и место рођења и датум одбране рада. Ови лични подаци могу се објавити на мрежним страницама дигиталне библиотеке, у електронском каталогу и у публикацијама Универзитета у Београду.

Потпис аутора

У Београду, 29.05.2017.

